Theses and Dissertations   Student Graduate Works

12-1999

Application of the Interaction Picture to Reactive Scattering in One Dimension

Michael J. MacLachlan

Follow this and additional works at: https://scholar.afit.edu/etd

Part of the Engineering Physics Commons

Recommended Citation

www.manaraa.com

APPLICATION OF THE INTERACTION PICTURE
TO REACTIVE SCATTERING
IN ONE DIMENSION

DISSERTATION

Michael J. MacLachlan, Major, USAF

AFIT/DS/ENP/99-02

DEPARTMENT OF THE AIR FORCE
AIR UNIVERSITY
AIR FORCE INSTITUTE OF TECHNOLOGY

Wright-Patterson Air Force Base, Ohio

The views expressed in this dissertation are those of the author and do not reflect the official policy or position of the Department of Defense or the United States Government.

AFIT/DSP/ENP/99-02

Application of the Interaction Picture to Reactive Scattering in One Dimension

DISSERTATION

Presented to the Faculty of the School of Engineering

of the Air Force Institute of Technology

Air University

In Partial Fulfillment of the

Requirements for the Degree of

Doctor of Philosophy

Michael J. MacLachlan, B.M., B.S.E.E., M.S.N.E
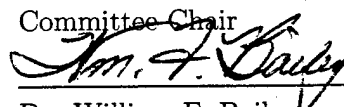
Major, USAF

September 1999
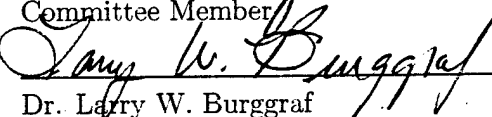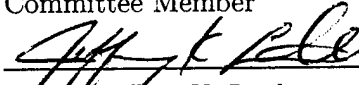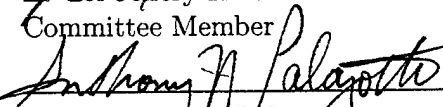
Application of the Interaction Picture to Reactive Scattering in One Dimension

Michael J. MacLachlan, B.M., B.S.E.E., M.S.N.E

Major, USAF

Approved:

_____   _13 Sept 99_
Dr. David E. Weeks   Date
Committee Chair

_____   _13 Sept 99_
Dr. William F. Bailey   Date
Committee Member

_____   _13 Sept 1999_
Dr. Larry W. Burggraf   Date
Committee Member

_____   _13 Sept 1999_
Lt Col Jeffery K. Little   Date
Committee Member

_____   _13 Sept 99_
Dr. Anthony N. Palazotto   Date
Dean's Representative

_____
Robert A. Calico, Jr
Dean

Preface

In the Air Force Research Laboratory's Propulsion Sciences and Advanced Concepts Division, teams of scientists and engineers are engaged in research aimed at making rockets and aircraft more capable and more efficient. They design new high-energy molecules to improve performance of propellants. They develop and investigate new materials, searching for ways to make lighter-weight components that function at higher temperatures. They attempt to make vehicles and weapons more survivable by manipulating their exhaust chemistry and probing that of adversaries' vehicles and weapons.

Some of this research is done analytically; most experimentally. In many cases, the substances involved in the experimental investigations are extremely flammable, explosive or toxic. To work with such substances safely is a difficult and expensive, but necessary proposition. If it were possible analytically to predict the outcomes of reactions and the configurations of molecules, the need for such laborious experiments could be reduced to simple one-time verifications of the computational predictions. For now and for the foreseeable future, however, analytical approaches are vastly slower, more difficult, and more expensive than experimentation. Great strides are needed in both numerical algorithms and computer hardware before computer calculations can feasibly replace even relatively simple chemical experiments on the types of molecules most valuable in aerospace propulsion applications. This project originated in this need, which is only one example among many beneficial potential applications of quantum modeling of chemical systems.

No great strides have resulted, but perhaps a step was taken in the right direction, thanks to the generous support of numerous people and organizations. This project was sponsored by the High Energy Density Matter Star Team at the Air Force Research Laboratory Propulsion Directorate. My thanks to the team's leaders, Dr. Jeff Sheehy and Dr. Mario Fajardo, as well as their redoubtable branch chief, Dr. Pat Carrick, for the opportunity. Our mutual leaders, Dr. Steve Rodgers and Dr. Phil Kessel, and recently Mr. Mike Huggins, have also been indispensably supportive. I was also honored to receive encouragement and counsel regarding the mechanics of completing a doctorate from three of the most senior leaders of the Propulsion Directorate: Col John Rogacki, Col Wesley

Table of Contents

x

AFIT/DSP/ENP/99-02

Abstract

The interaction picture is used together with the channel-packet method in a new time-dependent approach to compute reactive scattering matrix elements. The channel-packet method enables the use of the interaction picture for computing reactive S-matrix elements by splitting the computational effort into two parts. First, asymptotic reactant and product wavepackets are individually propagated into the interaction region of the potential to form Møller states. The interaction picture, in contrast to the usual Schrödinger picture of quantum mechanics, is so constructed that a wavefunction that experiences no change in potential (that is, a free-particle wavefunction) remains always fixed, with no translation or distortion. In the Schrödinger picture, free-particle wavefunctions translate and spread with time. By removing free-particle spreading, the use of the interaction picture reduces the size of the region of space that must be modeled when computing the Møller states. Since the asymptotic wavepackets are propagated in time independently of each other, it is possible to choose an asymptotic Hamiltonian and corresponding interaction picture that is well suited for each arrangement channel. By using two different interaction pictures, one for the reactant arrangement channel and one for the product arrangement channel, it is possible to realize savings in the required grid size. During the second part of the channel-packet computation, the reactant and product wavepackets obtained from the first part of the calculation are further propagated using the Schrödinger picture. The time-dependent correlation between the evolving wavepackets is calculated as they split into energetically accessible arrangement channels and are absorbed using absorbing boundary conditions.

The use of the interaction picture for computing S-matrix elements is developed, validated, and illustrated using a simple one-dimensional reactive example where the size of the grid required for computing the Møller state in the interaction picture is reduced by a factor of two when compared with required grid size in the Schrödinger picture. Larger reductions in grid requirements are realized when the wavepackets remain compact while evolving into Møller states, especially when reactant or product momenta are high.

Application of the Interaction Picture to Reactive Scattering in One Dimension

I. Introduction

1.1 Context of the Research

The purpose of this project is to advance certain computational approaches to molecular scattering theory, part of the physics that underlies chemical kinetics. Chemical reactions are macroscopic manifestations of numerous individual collisions among molecules of various species, carrying some thermal distribution of translational, rotational, vibrational, and electronic energies. Each pair of colliding molecules experiences a spatially dependent mutual force, which is appreciable over some "interaction region" of relatively small intermolecular separation distances and falls to zero in the asymptotic limit of large separations. The interaction force is the observable manifestation of an interaction potential-energy function whose effect is significant in the interaction region, and which approaches a constant value in the asymptotic limit. A classical view of a molecular collision event is illustrated in Figure 1.1. The figure shows an elastic collision in a coordinate system in which one of the particles is fixed. In a center-of-mass coordinate system, comparable dynamics could occur if one of the particles were of much larger mass than the other. The light particle travels in a straight line through the region of space where the intermolecular potential is negligible, along the asymptotic paths noted in the figure. The interaction region is small compared to the asymptotic regions of the interaction.

The example in Figure 1.1 is an elastic collision, wherein the colliding particles are changed in momentum only; not in internal configuration. Over the course of more complex "reactive" collisions, numerous types of changes may occur in the colliding reactant molecules, including the rearrangement of atoms within or between molecules, interconversion of kinetic and potential energy, and the exchange of kinetic energy among its translational, rotational, vibrational, and electronic manifestations. However, the event may always be seen as consisting of a brief period of strong interaction, preceded and followed by long periods of negligible interaction.

1-1
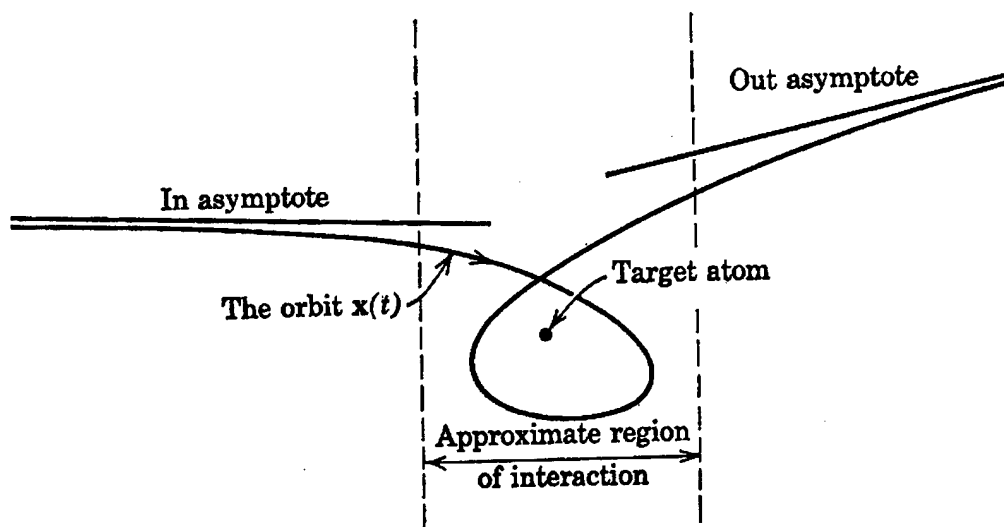
Figure 1.1   Schematic of a classical elastic collision event, as it might occur between a free and a fixed particle in a laboratory reference frame, or between a very light and a very heavy particle in a center-of-mass frame(1).

In order to predict the outcome of a reaction, or to understand a known reaction from first principles, one would like to know the probabilities that various asymptotic post-collision states will result from the asymptotic pre-collision states. The information needed to derive the probability that reactants in each possible energetic state and physical configuration will give rise to each possible state and configuration of products is contained in the scattering operator **S**. The state-to-state reaction probability can be averaged, weighted by the statistical momentum distribution of the reactants, to obtain scattering cross sections, which can be used in turn to calculate reaction rates and predict macroscopic reaction outcomes. The scattering operator is derived numerically in an energy representation of finite order, known as the S matrix. The square of the absolute value of the S matrix gives, for each pair of reactant and product energies, the probability that a reaction yielding the particular set of products at the selected product energy and configuration will result from the collision of the reactants at the selected reactant energy and configuration.

Both time-dependent or time-independent techniques have been developed to compute the S matrix (or portions of it) numerically. Time-independent methods(2–6) are

limited in speed and scope of application by their dependence on the diagonalization of large matrices. Time-dependent methods(7–14) have been hampered by their requirement to follow the motion of quantum or semiclassical particles over large changes in position and momentum during the course of the collision, over the full time from before the reactants begin to interact, through the collision, to the time when the products no longer interact with each other. Both the time-independent and the time-dependent methods therefore present large computational problems, which can only be solved with reasonable speed and accuracy for collisions involving very few atoms. Based on the numerical techniques available in 1988, Kosloff estimated that fast minicomputers could reasonably be used for problems with three coordinate degrees of freedom, and that, based on expected improvements in computational hardware alone, this capability would increase by one degree of freedom every seven to eight years(7). The analytical techniques Kosloff envisioned, like the ones treated in this project, all invoke the Born-Oppenheimer approximation. This is the assumption that electrons adapt instantaneously to the motion of their nuclei, allowing the treatment of atoms without dealing with electrons as separate objects(15). Within this approximation, the neglect of overall system rotations enables three degrees of freedom to suffice for examining two-atom collisions, as will be seen in Section 1.3. Each additional atom adds three more degrees of freedom to the problem, and the computational time required to compute the S matrix increases rapidly with the number of degrees of freedom. The scaling of computational effort with degrees of freedom is estimated in Appendix A. Despite this, recent algorithmic developments such as absorbing boundary conditions have already yielded some six-dimensional calculations within the eight-year period following Kosloff's estimate(16–19). This is a good illustration of the extra leverage algorithmic advances offer to complement progress in computer hardware. However, computational improvements notwithstanding, existing computational capabilities are still far from sufficient for full quantum-mechanical treatment of the majority of reactive scattering problems.

Typically, quantum computations are performed using a view or "picture" of the mechanics of quantum wavefunctions known as the Schrödinger picture. Complex wavefunctions containing both the positional and momentum-space distributions of a quantum

system's probability density, are common to all quantum "pictures." The absolute value squared, $\langle \Psi | \Psi \rangle$, of a wavefunction Ψ gives the distribution of the probability of the system being found in a particular configuration. The Schrödinger picture is characterized by wavefunctions obeying the Schrödinger equation of motion in the form

$$i\hbar \frac{d}{dt} |\psi\rangle_S = \mathbf{H}_S |\psi\rangle_S \,, \tag{1.1}$$

where $\mathbf{H}_s$ is the full system Hamiltonian as discussed in Section 1.3. Scattering calculations can be performed fruitfully in the Schrödinger picture, but this project demonstrates that another framework, the interaction picture, offers computational advantages at least in some scattering problems. In the interaction picture, described in detail in Section 3.5, wavefunctions obey the Schrödinger equation in the same form,

$$i\hbar \frac{d}{dt} |\psi\rangle_I = \mathbf{H}_I |\psi\rangle_I \,, \tag{1.2}$$

as in the Schrödinger picture, but the Hamiltonian operator $\mathbf{H}_I$ and the wavefunction ψ_I are both defined in such a way as to cancel out all "free" motion in the system—such as the motion experienced in the scattering system in its asymptotic region.

In this project, the interaction picture is part of a collection of techniques assembled to increase the efficiency with which S-matrix elements can be computed. Three new time-dependent computational approaches—the channel-packet method, absorbing boundary conditions, and the interaction picture—are used together in a single model for the first time. The channel-packet method allows the calculation of relevant sets of reactive S-matrix elements without the expense of approximating the entire matrix, and is the key to surmounting long-standing difficulties with the application of the interaction picture to reactive scattering calculations (1). The other two techniques complement the channel-packet method by decreasing its computational effort. The assembly of techniques is developed theoretically in two dimensions in Section 1.3, and analyzed computationally in one dimension elsewhere in this document. It is extensible in a straightforward way to systems with higher degrees of freedom, and should improve further in speed if transported to parallel-architecture computers.

1.2 Research Approach and Scope

The tools developed for this project are based on simulated time evolution of wave-functions as they interact with one-dimensional potentials. Both the interaction picture (Section 3.5) and the Schrödinger picture are used. The channel-packet method, described in Chapter II, requires two separate time evolutions, one of which (to calculate Møller states) benefits from the use of the interaction picture, and one of which (the calculation of correlation functions) is done in the Schrödinger picture with the aid of absorbing boundary conditions (Section 3.4). The split-operator technique of Section 3.1 is the algorithm of choice for propagation in the Schrödinger picture, which is used as a reference for comparison with the interaction-picture results. Two potentially valuable approaches to wavepacket propagation in the interaction picture were set aside when they failed to produce accurate results reliably. These methods, the finite-basis approach and Tannor's "Heisenberg" approach, are described in Chapter IV, along with a third approach that is accurate and straightforward to implement, but cannot provide a means of reducing computational grid sizes. The only interaction-picture technique that consistently gave accurate results on a variety of potentials is the sequential nested interaction picture, described in Section 3.5.4. Results based on the application of the sequential nested interaction picture appear in Chapters V and VI.

1.3 Quantum Reactive Scattering in One and Two Dimensions

The research reported here deals primarily with one-dimensional quantum-mechanical models of reactive scattering. To illustrate how the techniques can be applied to problems of higher order, the two-dimensional theory is also developed. Both theories are developed in the familiar Schrödinger picture of quantum mechanics.

In time-dependent calculations, scattering events are modeled using complex wave-functions that evolve in a vector space that is viewed in two equivalent representations. In the position or "coordinate" representation, the amplitude of the wavefunction gives the distribution of its probability amplitude across the position coordinate $\overline{x}$. In the momentum representation, obtained by Fourier transform from the position representation, the amplitude of the wavefunction represents its momentum, $\overline{p} = \hbar\overline{k}$. It is often conve-

nient to express momentum in terms of $\overline{\mathbf{k}}$ rather than $\overline{\mathbf{p}}$. This is done freely henceforth in this document, particularly since the system of atomic units is always used, in which Planck's constant $\hbar = 1$. A system involving n particles of mass m_i, then, is described by a single wavefunction $|\psi\rangle$ of reduced mass μ, position $\langle\overline{\mathbf{x}}\rangle = \langle\psi|\,\mathbf{x}\,|\psi\rangle$, and momentum $\langle\overline{\mathbf{p}}\rangle = \langle\psi|\,\mathbf{p}\,|\psi\rangle$ in a position and a momentum space of dimension $3(n-2)$. The reduction in dimension from $3n$ to $3(n-2)$ is accomplished by fixing the center of mass and neglecting any overall rotation(20).

Time-dependent methods are based on numerical solutions of the time-dependent Schrödinger equation,

$$i\hbar\frac{d}{dt}\,|\psi(t)\rangle = \mathbf{H}\,|\psi(t)\rangle,\qquad(1.3)$$

which, for time-independent Hamiltonian operators $\mathbf{H}$, has the formal solution,

$$|\psi(t)\rangle = e^{-i\mathbf{H}(t-t_0)/\hbar}\,|\psi(t_0)\rangle,\qquad(1.4)$$

where $|\psi(t_0)\rangle$ is the state vector at time $t = t_0$. Therefore, the Hamiltonian conveniently expressed as

$$\mathbf{H} = \mathbf{H}_a + \mathbf{V}(\bar{x}),\qquad(1.5)$$

must be derived. Given a numerical approximation for the interaction potential $\mathbf{V}(\bar{x})$ between the reactants, all that remains is to add the asymptotic potential $\mathbf{H}_a$, containing the kinetic energy of the reactants' translation toward each other, plus any internal vibrational or rotational energy the reactants carry. The asymptotic potential, $\mathbf{H}_a$, plays an important role in the construction of Møller operators (Section 2.2) and the interaction picture (Section 3.5). The numerical approximation of the full Hamiltonian is used to derive the time-evolution operator $\mathbf{U}(t,t_0) = e^{-i\mathbf{H}(t-t_0)/\hbar}$, which governs the behavior of the system throughout the collision process. Time-dependent numerical methods use approximations of $\mathbf{U}(t',t)$ over successive short time intervals $\Delta t = t' - t$ to evolve the system wavefunction over the required time period.

1.3.1 The One-Dimensional Interaction Hamiltonian.   For purposes of illustration, the simplest collision to describe is that of two structureless particles with no angular momentum. In this case, the motion of the wavefunction relative to center-of-mass coordinates is one-dimensional. Using bold type for operator variables, the Hamiltonian for this one-dimensional system can be written

$$\mathbf{H} = \mathbf{H}_a + \mathbf{V}(x), \tag{1.6}$$

where the potential operator $\mathbf{V}(x) = V(\mathbf{x})$ describes the interaction of the two particles, and the asymptotic Hamiltonian,

$$\begin{aligned}\mathbf{H}_a &= \lim_{x \to \pm\infty} \mathbf{H} \\ &= \frac{\hbar^2 \mathbf{k}^2}{2\mu}, \end{aligned} \tag{1.7}$$

is obtained in the asymptotic limit where $\lim_{x \to \pm\infty} \mathbf{V}(x) = 0$. Here $\mathbf{k}$ represents the one-dimensional momentum operator conjugate to $\mathbf{x}$. Equation (1.6) is not only a convenient way of accounting for the kinetic- and potential-energy contributions to the full Hamiltonian; it will also serve as a motivator and guide to the construction of the interaction picture in Section 3.5.

1.3.2 Two-Dimensional Interaction Hamiltonians.   If one of two colliding particles is a diatomic molecule consisting of atoms labeled A and B, and the other particle is an atom labeled C, the resulting three-body system requires $3(3-2) = 3$ coordinates to locate each atom in the rotationless center-of-mass reference frame. If the angle given by the vertices A, B, and C is fixed—for example, if the atoms are constrained to move along a single line—then the resulting collinear system requires only two coordinates to locate the atomic positions. One possible choice of coordinates, called bond coordinates, is illustrated in Figure 1.2, where the coordinate x is the distance between atoms A and B, and y is the distance between atoms B and C. Bond coordinates have the advantage of generality, describing all possible arrangements equally well. The Hamiltonian in bond
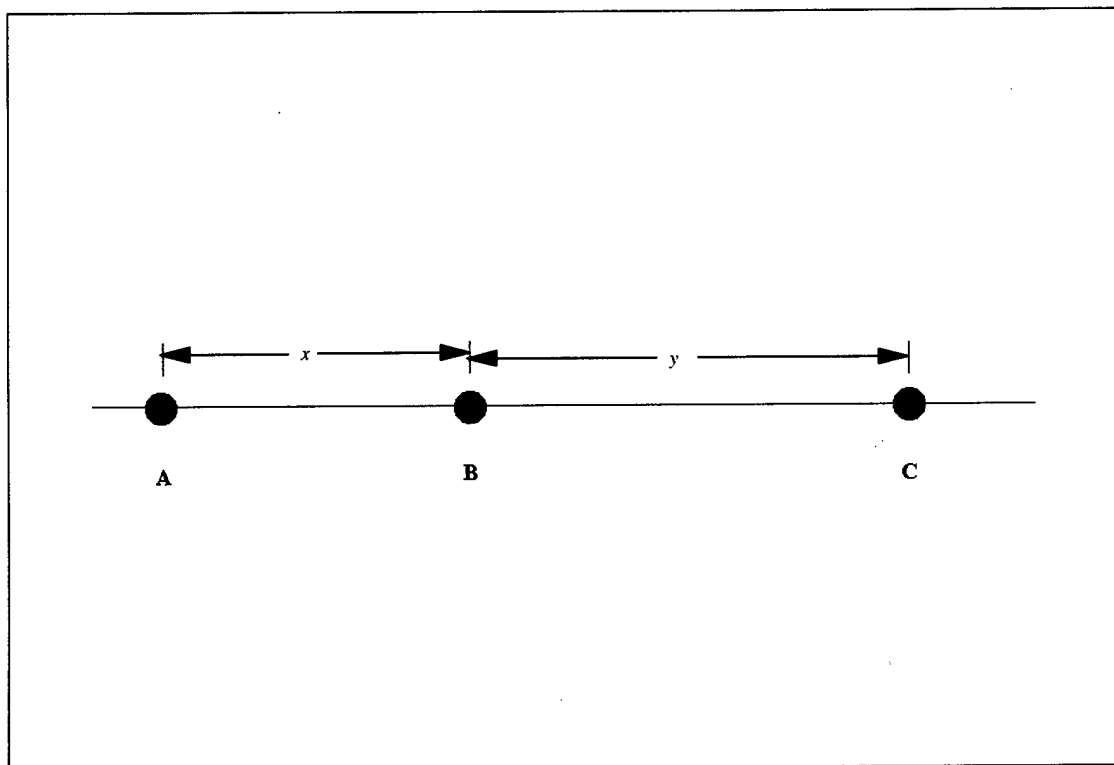
Figure 1.2   Bond coordinates for three collinear bodies.

coordinates is

$$\mathbf{H}_b = \frac{\hbar^2 \mathbf{k}_x^2}{2\mu_{AB}} + \frac{\hbar^2 \mathbf{k}_y^2}{2\mu_{BC}} - \frac{\hbar^2 \mathbf{k}_x \mathbf{k}_y}{m_B} + \mathbf{V}(x,y), \tag{1.8}$$

where $\mathbf{k}_x$ and $\mathbf{k}_y$ are the momentum operators conjugate to x and y,

$$\mu_{AB} = \frac{m_A m_B}{m_A + m_B} \tag{1.9}$$

and

$$\mu_{BC} = \frac{m_B m_C}{m_B + m_C} \tag{1.10}$$

are the reduced masses of the two pairs of adjacent atoms, and m_A, m_B, and m_C are the masses of the respective atoms(21). In the asymptotic limit of large x (or y), the atom A (C) no longer interacts with the diatom BC (AB) and $V(x,y) \to V(y)$ (or $V(x)$). The
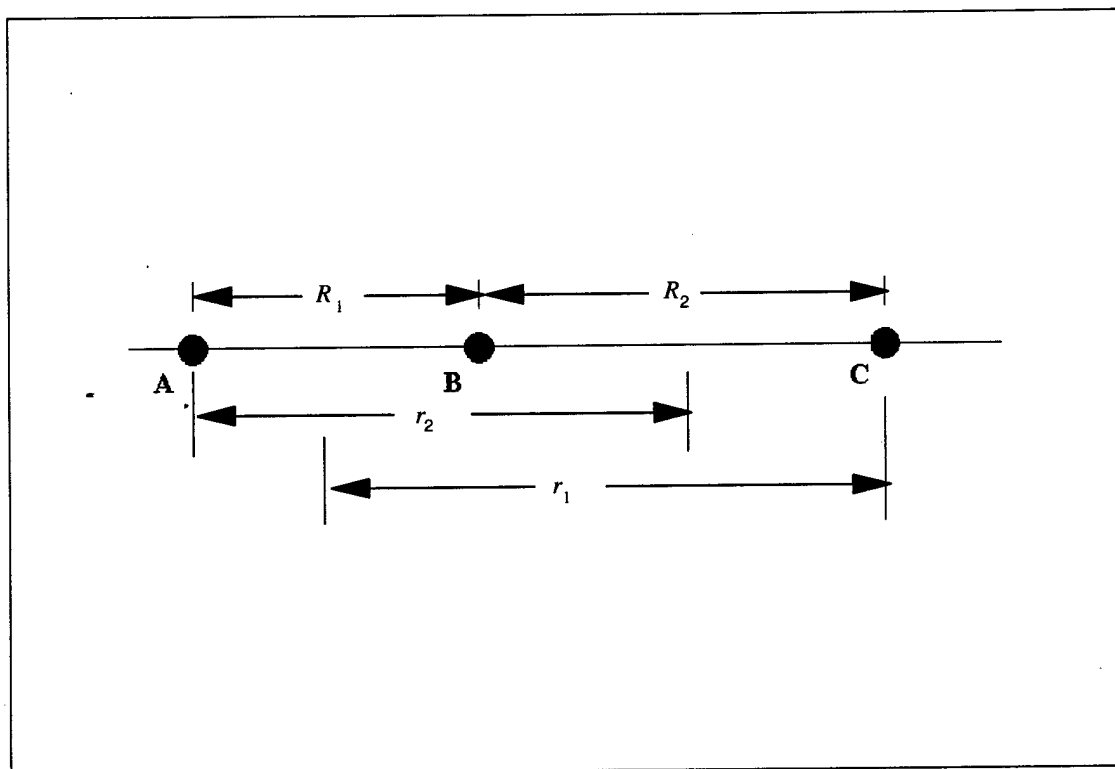
Figure 1.3   Jacobi coordinates for three collinear bodies.

disadvantage of bond coordinates is manifest in these limits, where the Hamiltonian in equation (1.8) is not separable like equation (1.6) because of the kinetic coupling term $\hbar^2 k_x k_y / m_B$.

Using an alternative choice of coordinates, called Jacobi coordinates (Figure 1.3), the asymptotic Hamiltonian becomes separable, at the cost of using different Jacobi coordinates for different arrangements of particles in the asymptotic regions before and after the collision. In general, the three atoms A, B, and C may be arranged in any of four ways:

- all three atoms may be relatively close together and bound or strongly interacting (ABC),

- all three may be relatively far apart and not interacting (A + B + C),

- A and B may form a diatom while C is relatively distant (AB + C), or

- B and C may form a diatom while A is relatively distant (A + BC).

These four cases are termed "arrangement channels" in the context of molecular collision theory. However, as far as a collision event is concerned, the first case cannot be an asymptotic state of the reactants or products. It must be either a temporary transition state in the midst of the collision, or a bound state. A bound state cannot be the state prior to collision, since there are no free particles to collide with one another. Neither can it be the state following the collision in a conservative system which began in an unbound state. For computational simplicity, it is also possible to exclude the three-body case A + B + C by assuming that the system begins in one of the two remaining arrangement channels and restricting the energy of the collision so as to make complete dissociation energetically inaccessible. The interaction then becomes a one with only two possible outcomes, the arrangements AB + C and A + BC.

Each of the two arrangements has a corresponding set of Jacobi coordinates. In Figure 1.3, the two arrangements are labeled with the subscripts $\gamma = 1$ and $\gamma = 2$. In each arrangement, the coordinate R_γ represents the distance separating the two members of the diatom, and r_γ is the distance between the free atom and the center of mass of the diatom. The Hamiltonian in Jacobi coordinates is given by

$$\mathbf{H}_\gamma = \frac{\hbar^2 \mathbf{k}_{r_\gamma}^2}{2m_\gamma} + \frac{\hbar^2 \mathbf{k}_{R_\gamma}^2}{2\mu_\gamma} + \mathbf{V}_\gamma(r_\gamma, R_\gamma), \tag{1.11}$$

where m_γ is the mass of the lone atom, and μ_γ is the reduced mass of the atom-diatom system in the arrangement channel labeled by γ. Thus, for one labeling of the two arrangements,

$$\mu_1 = \frac{(m_A + m_B)\, m_C}{m_A m_B m_C}, \tag{1.12}$$

and

$$\mu_2 = \frac{m_A\, (m_B + m_C)}{m_A m_B m_C}. \tag{1.13}$$

In the asymptotic limit of large r_γ the Hamiltonian reduces to the sum of a free-particle Hamiltonian and an internal Hamiltonian,

$$
\begin{aligned}
\mathbf{H}_a^\gamma &= \lim_{r_\gamma \to \pm\infty} \mathbf{H}_\gamma \\
&= \frac{\hbar^2 \mathbf{k}_{r_\gamma}^2}{2m_\gamma} + \frac{\hbar^2 \mathbf{k}_{R_\gamma}^2}{2\mu_\gamma} + \lim_{r_\gamma \to \pm\infty} \mathbf{V}_\gamma(r_\gamma, R_\gamma) \\
&= \frac{\hbar^2 \mathbf{k}_{r_\gamma}^2}{2m_\gamma} + \frac{\hbar^2 \mathbf{k}_{R_\gamma}^2}{2\mu_\gamma} + \mathbf{V}_{int}^\gamma(R_\gamma) \\
&= \mathbf{H}_{rel}^\gamma + \mathbf{H}_{int}^\gamma.
\end{aligned}
\tag{1.14}
$$

In equation (1.14), $\mathbf{V}_{int}^\gamma(R_\gamma) = \lim_{r \to \pm\infty} \mathbf{V}_\gamma(r_\gamma, R_\gamma)$ is the internal potential of the diatom, and $\mathbf{k}_{r_\gamma}$ and $\mathbf{k}_{R_\gamma}$ are the momentum operators conjugate to $\mathbf{r}_\gamma$ and $\mathbf{R}_\gamma$ respectively. The last term in equation (1.14),

$$
\mathbf{H}_{int}^\gamma = \frac{\hbar^2 \mathbf{k}_{R_\gamma}^2}{2\mu_\gamma} + \mathbf{V}_{int}^\gamma(R_\gamma),
\tag{1.15}
$$

is the Hamiltonian of an isolated diatom, and

$$
\mathbf{H}_{rel}^\gamma = \frac{\hbar^2 \mathbf{k}_{r_\gamma}^2}{2m_\gamma}
\tag{1.16}
$$

describes the behavior of a free particle of mass m_γ with an energy equal to the relative kinetic energy between the atom and diatom. In general, $m_\gamma \neq m_{\gamma'}$, $\mu_\gamma \neq \mu_{\gamma'}$, and $\mathbf{V}^\gamma(r_\gamma, R_\gamma) \neq \mathbf{V}^{\gamma'}(r_{\gamma'}, R_{\gamma'})$; the two Hamiltonians are as distinct as the arrangements themselves. Thus, in an exchange reaction, such as AB + C $\to$ A + BC, one must use both coordinate systems in order to take advantage of the simplified form (1.14) for both the reactant and product asymptotic Hamiltonians. The requirement for multiple coordinate systems and Hamiltonians, and the need to change coordinate systems in mid-collision, present the principal difficulties with the use of Jacobi coordinates in scattering calculations.

II. Time-Dependent Molecular Scattering Theory

The channel-packet method is a technique for obtaining selected elements of the S matrix by means of time-dependent quantum propagation techniques. Such techniques are based on the numerical solution of the time-dependent Schrödinger equation,

$$i\hbar \frac{d}{dt} |\psi(t)\rangle = \mathbf{H} |\psi(t)\rangle. \tag{2.1}$$

The formal solution to the time-dependent Schrödinger equation for a time-independent Hamiltonian operator $\mathbf{H}$ is

$$
\begin{aligned}
|\psi(t)\rangle &= \mathbf{U}(t, t_0) |\psi(t_0)\rangle \\
&= e^{-i\mathbf{H}(t-t_0)/\hbar} |\psi(t_0)\rangle,
\end{aligned}
\tag{2.2}
$$

where $|\psi(t_0)\rangle$ is the state vector at time $t = t_0$, and $\mathbf{U}(t, t_0) = e^{-i\mathbf{H}(t-t_0)/\hbar}$ is the time-evolution operator. Commonly, it is convenient to set $t_0 = 0$, and use the shorthand notation $\mathbf{U}(t) = \mathbf{U}(t, 0)$.

There have been several applications of the channel-packet method to a variety of scattering problems. In particular, the method has been used to compute state to state S-matrix elements for the collinear $H + H_2(n) \rightleftharpoons H_2(n') + H$ reaction(22,23) and more recently for a two dimensional model $OC + OH(n = 0) \rightleftharpoons OCO(n = 0) + H$ reaction(24). In a larger three-dimensional calculation, Dai and Zhang have used the channel-packet method to compute exact state-to-state S-matrix elements for the $H + O_2$ reaction(12). One common advantage shared by all of these calculations is the facility with which the channel-packet method provides S-matrix elements over a wide range of energies. In addition to exact quantum calculations, the channel-packet method has also been useful in formulating several approximate strategies for computing S-matrix elements. These include a new semiclassical method for computing S-matrix elements developed by Garashchuk and Tannor(25), and the application of the multiconfiguration time-dependent Hartree approach to computing S-matrix elements by Jäckle and Meyer(26).

2.1 Channel Packets

The two-dimensional asymptotic Hamiltonian of equation (1.14), $\mathbf{H}_a^\gamma$, has two components, $\mathbf{H}_{rel}^\gamma$ and $\mathbf{H}_{int}^\gamma$. Since both $\mathbf{H}_{rel}^\gamma$ and $\mathbf{H}_{int}^\gamma$ have known eigenvalues and eigenstates, eigenstates of the asymptotic Hamiltonian can be constructed in Jacobi coordinates as direct products of free-particle eigenstates, $\left|k_{r_\gamma}\right\rangle = \left|k_\gamma\right\rangle$, and diatomic eigenstates, $\left|\gamma\right\rangle$:

$$
\begin{aligned}
\mathbf{H}_a^\gamma \left|k_\gamma, \gamma\right\rangle &= \left(\mathbf{H}_{rel}^\gamma + \mathbf{H}_{int}^\gamma\right) \left|k_\gamma\right\rangle \left|\gamma\right\rangle \\
&= \mathbf{H}_{rel}^\gamma \left|k_\gamma\right\rangle \left|\gamma\right\rangle + \left|k_\gamma\right\rangle \mathbf{H}_{int}^\gamma \left|\gamma\right\rangle \\
&= \frac{\hbar^2 k_\gamma^2}{2m_\gamma} \left|k_\gamma\right\rangle \left|\gamma\right\rangle + E_\gamma \left|k_\gamma\right\rangle \left|\gamma\right\rangle \\
&= \left(\frac{\hbar^2 k_\gamma^2}{2m_\gamma} + E_\gamma\right) \left|k_\gamma, \gamma\right\rangle,
\end{aligned}
\tag{2.3}
$$

where the index γ is now used to label the *channel*, a term that includes both the arrangement channel and the internal eigenstate of the diatom. For each arrangement channel, there exists one channel for each eigenstate of the internal Hamiltonian $\mathbf{H}_{int}^\gamma$.

Each channel is associated with a single eigenstate $\left|\gamma\right\rangle$ of the diatom, and infinitely many free-particle eigenstates $\left|k_\gamma\right\rangle$. Rather than attempting to consider the non-square-integrable states $\left|k_\gamma\right\rangle \left|\gamma\right\rangle = \left|k_\gamma, \gamma\right\rangle$ individually, it is useful in collision modeling to construct localized linear combinations of the $\left|k_\gamma, \gamma\right\rangle$,

$$
\left|\psi_{in(out)}^\gamma\right\rangle = \int_{-\infty}^{\infty} dk_\gamma \eta_{\pm}\left(k_\gamma\right) \left|k_\gamma, \gamma\right\rangle.
\tag{2.4}
$$

Equation (2.4) defines two wavepackets, or "channel packets," in the channel labeled γ. The channel packet $\left|\psi_{in}^\gamma\right\rangle$ is expanded in terms of the eigenstates $\left|k_\gamma, \gamma\right\rangle$ of the γ-channel Hamiltonian, where the expansion coefficients $\eta_+\left(k_\gamma\right)$ are chosen to be appreciable over some particular range of momenta k_γ. The packet $\left|\psi_{out}^\gamma\right\rangle$ is also expanded in terms of the eigenstates $\left|k_\gamma, \gamma\right\rangle$, with expansion coefficients $\eta_-\left(k_\gamma\right)$. The channel packets $\left|\psi_{in}^\gamma\right\rangle$ and $\left|\psi_{out}^\gamma\right\rangle$ will later represent reactants and products, respectively, in the channel γ.

It is convenient to choose the expansion coefficients $\eta_\pm \left(k_\gamma \right)$ so that the state $\left| \psi^\gamma_{in(out)} \right\rangle$ is a complex Gaussian in the momentum coordinate k_γ,

$$\eta_\pm \left(k_\gamma \right) = \left[2\pi \left(\Delta k \right)^2_0 \right]^{-\frac{1}{4}} \exp \left[-\frac{\left(k_\gamma - k_{\gamma 0} \right)^2}{4 \left(\Delta k \right)^2_0} + i r_{\gamma 0} \left(k_\gamma - k_{\gamma 0} \right) \right], \qquad (2.5)$$

where $\left(\Delta k \right)_0$ is the uncertainty in the momentum, and the constants $r_{\gamma 0}$ and $k_{\gamma 0}$ fix the center of the Gaussian's representation in coordinate and momentum space, respectively(27). The Gaussian is chosen because it can be manipulated analytically, and can be defined to include whatever particular range of values of momentum k_γ may be of interest. Since the Fourier transform of a Gaussian is also a Gaussian, the coordinate representation of such a channel packet in Jacobi coordinates is the direct product of a Gaussian in the r_γ coordinate and a diatomic eigenfunction in the R_γ coordinate. Such channel packets are the basis for the method described in Section 2.3 for evaluation of matrix elements of the scattering operator.

2.2 The Scattering Operator

The scattering operator $\mathbf{S}$ is the keystone of quantum molecular scattering theory. The scattering operator relates the reactant and product states, $|\psi_{in}\rangle$ and $|\psi_{out}\rangle$, of an interaction as

$$|\psi_{out}\rangle = \mathbf{S} |\psi_{in}\rangle . \qquad (2.6)$$

For the scattering operator to exist, the interaction potential $\mathbf{V}(\overline{x})$ must satisfy the conditions(1)

1. $\mathbf{V}(\overline{x}) = O \left(x^{-3-\epsilon} \right)$ as $x \to \infty$; that is, the potential approaches zero more rapidly than does x^{-3} in the asymptotic limit;

2. $\mathbf{V}(\overline{x}) = O \left(x^{-2+\epsilon} \right)$ as $x \to 0$; that is, the potential becomes unbounded less rapidly than x^{-2} at the origin; and

3. $\mathbf{V}(\overline{x})$ is continuous nearly everywhere for $0 < x < \infty$.

It is important to note that even though the pure internuclear Coulomb potential does not meet conditions 1 and 2 above, the presence of atomic electrons serves to make the **S** operator formalism applicable to atomic and molecular problems. Atomic electrons shield nuclear charges from one another at large separations, and add to the interatomic repulsion at small distances.

It is useful to express the scattering operator as the product

$$\mathbf{S}^{\gamma'\gamma} = \Omega_-^{\gamma'\dagger}\Omega_+^\gamma, \tag{2.7}$$

where the Møller operators are defined as

$$\Omega_\pm^\gamma = \lim_{t\to\mp\infty} e^{i\mathbf{H}t}e^{-i\mathbf{H}_a^\gamma t}. \tag{2.8}$$

The Møller operators are isometric ($\Omega_\pm^\dagger\Omega_\pm = \mathbf{1}$), and are unitary ($\Omega_\pm^\dagger = \Omega_\pm^{-1}$) only if no bound states exist. Møller operators also obey the "intertwining" relation(28)

$$\mathbf{H}\Omega_\pm^\gamma = \Omega_\pm^\gamma\mathbf{H}_a^\gamma, \tag{2.9}$$

where **H** is the full Hamiltonian, and $\mathbf{H}_a^\gamma$ is the asymptotic Hamiltonian in arrangement channel γ. The intertwining relation will be important in Chapter 3. In terms of the Møller operators, the probability of scattering from a given reactant state $|\psi_{in}^\gamma\rangle$ to a given product state $\left|\psi_{out}^{\gamma'}\right\rangle$ is given by

$$
\begin{aligned}
\mathbf{P}^{\gamma'\gamma} &= \left|\left\langle\psi_{out}^{\gamma'}\left|\mathbf{S}^{\gamma'\gamma}\right|\psi_{in}^\gamma\right\rangle\right|^2 \\
&= \left|\left\langle\psi_{out}^{\gamma'}\left|\Omega_-^{\gamma'\dagger}\Omega_+^\gamma\right|\psi_{in}^\gamma\right\rangle\right|^2 \\
&= \left|\left\langle\psi_-^{\gamma'}\left|\psi_+^\gamma\right\rangle\right|^2,
\end{aligned} \tag{2.10}
$$

where γ and γ' indicate the reactant and product channels, respectively. The states $\left|\psi_-^{\gamma'}\right\rangle = \Omega_-^{\gamma'}\left|\psi_{out}^{\gamma'}\right\rangle$ and $|\psi_+^\gamma\rangle = \Omega_+^\gamma|\psi_{in}^\gamma\rangle$ are called Møller states.

The scattering operator is customarily evaluated in its energy or momentum representation, called the S matrix. S-matrix elements are expressed in the momentum repre-

sentation as(31)

$$\sqrt{\kappa'_{\gamma'}\kappa_{\gamma}}\,\delta\left(E_{\gamma'}-E_{\gamma}\right)S^{\gamma',\gamma}_{k'_{\gamma'},k_{\gamma}} = \left\langle k'_{\gamma'},\gamma'\right|\mathbf{S}\left|k_{\gamma},\gamma\right\rangle$$
$$= \left\langle k'_{\gamma'},\gamma'\right|\Omega^{\gamma'\dagger}_{-}\Omega^{\gamma}_{+}\left|k_{\gamma},\gamma\right\rangle$$
$$= \left\langle k'_{\gamma'},\gamma'-\right|k_{\gamma},\gamma+\rangle. \qquad (2.11)$$

The density of states,

$$\kappa_{\gamma} = \frac{\partial E}{\partial|k_{\gamma}|}$$
$$= \frac{\partial}{\partial|k_{\gamma}|}\frac{\hbar^2 k_{\gamma}^2}{2\mu_{\gamma}}$$
$$= \frac{\hbar^2|k_{\gamma}|}{\mu_{\gamma}} \qquad (2.12)$$

is introduced in equation (2.11) to convert the S matrix from energy normalization to momentum normalization. The absolute value squared of the S-matrix element $S^{\gamma',\gamma}_{k'_{\gamma'},k_{\gamma}}$ is the probability that a reaction that starts with reactants in the state $|k_{\gamma},\gamma\rangle$ will yield products in the state $\left|k'_{\gamma'},\gamma'\right\rangle$.

The right-hand side of equation (2.11) is the inner product of the vectors

$$|k_{\gamma},\gamma+\rangle = \Omega^{\gamma}_{+}|k_{\gamma},\gamma\rangle \qquad (2.13)$$

and

$$\left|k_{\gamma'},\gamma'-\right\rangle = \Omega^{\gamma'}_{-}\left|k_{\gamma'},\gamma'\right\rangle, \qquad (2.14)$$

2-5

which are eigenstates of the full Hamiltonian. This can be shown using the intertwining relation (2.9), together with equations (2.13) and (2.3):

$$
\begin{aligned}
\mathbf{H} \left| k_\gamma, \gamma + \right\rangle &= \mathbf{H} \Omega_+^\gamma \left| k_\gamma, \gamma \right\rangle \\
&= \Omega_+^\gamma \mathbf{H}_a^\gamma \left| k_\gamma, \gamma \right\rangle \\
&= \left(\frac{\hbar^2 k_\gamma^2}{2 m_\gamma} + E_\gamma \right) \Omega_+^\gamma \left| k_\gamma, \gamma \right\rangle \\
&= \left(\frac{\hbar^2 k_\gamma^2}{2 m_\gamma} + E_\gamma \right) \left| k_\gamma, \gamma + \right\rangle .
\end{aligned}
\tag{2.15}
$$

A similar argument shows that the states $\left| k_\gamma, \gamma - \right\rangle$, are also eigenstates of the full Hamiltonian.

Two observations regarding the states $\left| k_\gamma, \gamma \pm \right\rangle$ are useful in the development of the channel-packet method in Section 2.3. First, $\left| k_\gamma, \gamma \pm \right\rangle$ satisfy the orthogonality relation

$$
\begin{aligned}
\left\langle k'_{\gamma'}, \gamma' \pm \middle| k_\gamma, \gamma \pm \right\rangle &= \left\langle k'_{\gamma'}, \gamma' \middle| \Omega_\pm^{\gamma' \dagger} \Omega_\pm^\gamma \middle| k_\gamma, \gamma \right\rangle \\
&= \delta_{\gamma' \gamma} \left\langle k'_{\gamma'}, \gamma' \middle| k_\gamma, \gamma \right\rangle \\
&= \delta_{\gamma' \gamma} \delta \left(k'_{\gamma'} - k_\gamma \right) .
\end{aligned}
\tag{2.16}
$$

Second, if the full Hamiltonian $\mathbf{H}$ is time-independent, then solution of the time-dependent Schrödinger equation (2.1) for the time evolution of $\left| k_\gamma, \gamma \pm \right\rangle$ yields,

$$
\begin{aligned}
\left| k_\gamma, \gamma \pm ; t \right\rangle &= \mathbf{U}(t) \left| k_\gamma, \gamma \pm \right\rangle \\
&= e^{-i \mathbf{H} t / \hbar} \left| k_\gamma, \gamma \pm \right\rangle \\
&= \exp \left[-i \left(\frac{\mu_\gamma}{2} k_{\gamma(\gamma')}^2 + E_{\gamma(\gamma')} \right) \frac{t}{\hbar} \right] \left| k_\gamma, \gamma \pm \right\rangle .
\end{aligned}
\tag{2.17}
$$

2.3 Computation of S-Matrix Elements using Channel Packets

Channel packets, introduced in Section 2.1, were developed and used by Weeks and Tannor for computing matrix elements of the scattering operator(29,30). In this time-dependent method, a pair of wavepackets, $\left| \psi_{in}^\gamma \right\rangle$ and $\left| \psi_{out}^{\gamma'} \right\rangle$, defined using equation (2.4),

is used to derive S-matrix elements $S_{k'_{\gamma'},k_\gamma}^{\gamma',\gamma}$ for a broad range of momenta, k_γ and $k'_{\gamma'}$, within a particular pair of reactant and product channels γ and γ'.

The calculation begins by applying a numerical time-evolution scheme like those developed in Sections 3.1 and 3.2 to the channel packets to produce the Møller states

$$
\begin{aligned}
\left|\psi_+^\gamma\right\rangle &= \Omega_+^\gamma \left|\psi_{in}^\gamma\right\rangle \\
&= \lim_{t\to-\infty} e^{i\mathbf{H}t/\hbar} e^{-i\mathbf{H}_a^\gamma t/\hbar} \left|\psi_{in}^\gamma\right\rangle \\
&\approx e^{-i\mathbf{H}\tau/\hbar} e^{i\mathbf{H}_a^\gamma \tau/\hbar} \left|\psi_{in}^\gamma\right\rangle
\end{aligned}
\tag{2.18}
$$

and

$$
\begin{aligned}
\left|\psi_-^{\gamma'}\right\rangle &= \Omega_-^{\gamma'} \left|\psi_{out}^{\gamma'}\right\rangle \\
&\approx e^{i\mathbf{H}\tau/\hbar} e^{-i\mathbf{H}_a^{\gamma'}\tau/\hbar} \left|\psi_{out}^{\gamma'}\right\rangle,
\end{aligned}
\tag{2.19}
$$

where $\pm\tau$ are values of time t, defined such that essentially all of the product and reactant wavepackets experience only the asymptotic potential $\mathbf{H}_a$ for all t greater than $+\tau$ and less than $-\tau$. The coordinate representations of the states $\left|\psi_{in}^\gamma\right\rangle$ and $\left|\psi_{out}^{\gamma'}\right\rangle$ are chosen to be in the interaction region of the potential at time $t = 0$. The effect of the Møller operator Ω_+^γ on the initial state $\left|\psi_{in}^\gamma\right\rangle$ is to propagate it backward from time $t = 0$ to time $t = -\tau$ using the asymptotic Hamiltonian $\mathbf{H}_a^\gamma$ until the resulting intermediate state exits the interaction region, and then to propagate the intermediate state forward to time $t = 0$ again using the full Hamiltonian. Similarly, the product state $\left|\psi_{out}^{\gamma'}\right\rangle$ is propagated forward from time $t = 0$ to time $t = +\tau$ under $\mathbf{H}_a^{\gamma'}$, and back to time $t = 0$ under $\mathbf{H}$. The resulting Møller states can then be propagated under the full Hamiltonian, using the methods described in Chapter III.

The Fourier transform of the time-evolved Møller state $\left|\psi_+^\gamma(t)\right\rangle = \mathbf{U}(t)\Omega_+^\gamma \left|\psi_{in}^\gamma\right\rangle$ is

$$
\begin{aligned}
\left|A_+^\gamma(E)\right\rangle &= \int_{-\infty}^{\infty} dt \exp(iEt)\, \mathbf{U}(t) \left|\psi_+^\gamma\right\rangle \\
&= \int_{-\infty}^{\infty} dt \exp(iEt)\, \mathbf{U}(t)\Omega_+^\gamma \left|\psi_{in}^\gamma\right\rangle.
\end{aligned}
\tag{2.20}
$$

The channel packets $|\psi_{in}^{\gamma}\rangle$ and $\left|\psi_{out}^{\gamma'}\right\rangle$ can be expanded as in equation (2.4), in terms of the eigenvectors $|k_{\gamma}, \gamma\rangle$ and $\left|k_{\gamma'}', \gamma'\right\rangle$ respectively. Substitution of equations (2.18) and (2.4) into (2.20) yields

$$
\begin{aligned}
\left|A_+^{\gamma}(E)\right\rangle &= \int_{-\infty}^{\infty} dt \exp\left(iEt\right) \mathbf{U}(t)\Omega_+^{\gamma} \int_{-\infty}^{\infty} dk_{\gamma}\eta_+\left(k_{\gamma}\right)|k_{\gamma}, \gamma\rangle \\
&= \int_{-\infty}^{\infty} dt \exp\left(iEt\right) \mathbf{U}(t) \int_{-\infty}^{\infty} dk_{\gamma}\eta_+\left(k_{\gamma}\right)|k_{\gamma}, \gamma+\rangle. \quad (2.21)
\end{aligned}
$$

Equation (2.17), substituted in equation (2.21), gives

$$
\begin{aligned}
\left|A_+^{\gamma}(E)\right\rangle &= \int_{-\infty}^{\infty} dt \exp\left(i\frac{E}{\hbar}t\right) e^{-i\mathbf{H}t/\hbar} \int_{-\infty}^{\infty} dk_{\gamma}\eta_+\left(k_{\gamma}\right)|k_{\gamma}, \gamma+\rangle \\
&= \int_{-\infty}^{\infty} dt \exp\left(i\frac{E}{\hbar}t\right) \exp\left[-\frac{it}{\hbar}\left(\frac{\hbar^2 k_{\gamma}^2}{2\mu_{\gamma}} + E^{\gamma}\right)\right] \int_{-\infty}^{\infty} dk_{\gamma}\eta_+\left(k_{\gamma}\right)|k_{\gamma}, \gamma+\rangle \\
&= 2\pi \int_{-\infty}^{\infty} dk_{\gamma}\delta\left(\frac{\hbar}{2\mu_{\gamma}}\left(k_{\gamma}^2 - k_{\gamma}'^2\right)\right)\eta_+\left(k_{\gamma}\right)|k_{\gamma}, \gamma+\rangle \\
&= \frac{2\pi\mu_{\gamma}}{\hbar|k_{\gamma}|} \int_{-\infty}^{\infty} dk_{\gamma}\left[\delta\left(k_{\gamma'}' - k_{\gamma}\right) + \delta\left(k_{\gamma'}' + k_{\gamma}\right)\right]\eta_+\left(k_{\gamma}\right)|k_{\gamma}, \gamma+\rangle \\
&= \frac{2\pi\mu_{\gamma}}{\hbar|k_{\gamma}|} \left\{\eta_+\left(+k_{\gamma}\right)|+k_{\gamma}, \gamma+\rangle + \eta_+\left(-k_{\gamma}\right)|-k_{\gamma}, \gamma+\rangle\right\}, \quad (2.22)
\end{aligned}
$$

where the two degenerate eigenstates corresponding to positive and negative momenta $+k_{\gamma}$ and $-k_{\gamma}$ are the only terms of the integration singled out by the delta functions. The inner product of this expression with the product Møller state is then

$$
\begin{aligned}
\left\langle\psi_-^{\gamma'}\left|A_+^{\gamma}(E)\right\rangle\right. &= \frac{2\pi}{\hbar}\sqrt{\frac{\mu_{\gamma'}\mu_{\gamma}}{|k_{\gamma'}||k_{\gamma}|}}\left\{\eta_-^*\left(k_{\gamma'}'\right)\eta_+\left(+k_{\gamma}\right)\left\langle k_{\gamma'}', \gamma'-|k_{\gamma}, \gamma+\right\rangle\right. \\
&\qquad\left. + \eta_-^*\left(k_{\gamma'}'\right)\eta_+\left(-k_{\gamma}\right)\left\langle k_{\gamma'}', \gamma'-|k_{\gamma}, \gamma+\right\rangle\right\} \\
&= \frac{2\pi}{\hbar}\sqrt{\frac{\mu_{\gamma'}\mu_{\gamma}}{|k_{\gamma'}||k_{\gamma}|}}\left\{\eta_-^*\left(+k_{\gamma'}'\right)\eta_+\left(+k_{\gamma}\right)S_{+k_{\gamma'}', +k_{\gamma}}^{\gamma', \gamma}\right. \\
&\qquad + \eta_-^*\left(-k_{\gamma'}'\right)\eta_+\left(+k_{\gamma}\right)S_{-k_{\gamma'}', +k_{\gamma}}^{\gamma', \gamma} \\
&\qquad + \eta_-^*\left(+k_{\gamma'}'\right)\eta_+\left(-k_{\gamma}\right)S_{+k_{\gamma'}', -k_{\gamma}}^{\gamma', \gamma} \\
&\qquad\left. + \eta_-^*\left(-k_{\gamma'}'\right)\eta_+\left(-k_{\gamma}\right)S_{-k_{\gamma'}', -k_{\gamma}}^{\gamma', \gamma}\right\}. \quad (2.23)
\end{aligned}
$$

The channel-packet method allows a piecemeal evaluation of the S matrix by considering four special cases of equation (2.23), where the expansion coefficients $\eta_\pm$ are chosen so that either

1. $\eta_+ \left(+k_\gamma\right) = \eta_-^* \left(-k_{\gamma'}'\right) = 0$, with $\left\langle r_\gamma \left(-\tau\right)\right\rangle > 0$ and $\left\langle r_{\gamma'}' \left(+\tau\right)\right\rangle > 0$;

2. $\eta_+ \left(+k_\gamma\right) = \eta_-^* \left(+k_{\gamma'}'\right) = 0$, with $\left\langle r_\gamma \left(-\tau\right)\right\rangle > 0$ and $\left\langle r_{\gamma'}' \left(+\tau\right)\right\rangle < 0$;

3. $\eta_\pm \left(-k_\gamma\right) = \eta_-^* \left(-k_{\gamma'}'\right) = 0$, with $\left\langle r_\gamma \left(-\tau\right)\right\rangle < 0$ and $\left\langle r_{\gamma'}' \left(+\tau\right)\right\rangle > 0$; or

4. $\eta_+ \left(-k_\gamma\right) = \eta_-^* \left(+k_{\gamma'}'\right) = 0$, with $\left\langle r_\gamma \left(-\tau\right)\right\rangle < 0$ and $\left\langle r_{\gamma'}' \left(+\tau\right)\right\rangle < 0$.

In case 1, for example, the reactant wavepacket starts to the right of the origin, with all free-particle momentum directed to the left. The product wavepacket finishes up to the right of the origin, traveling to the right. Equation (2.23) reduces to

$$\left\langle \psi_-^{\gamma'} \middle| A_+^\gamma \left(E\right)\right\rangle = \frac{2\pi}{\hbar} \sqrt{\frac{\mu_{\gamma'} \mu_\gamma}{\left|k_{\gamma'}\right|\left|k_\gamma\right|}} \eta_-^* \left(+k_{\gamma'}'\right) \eta_+ \left(-k_\gamma\right) S_{+k_{\gamma'}',-k_\gamma}^{\gamma',\gamma} \qquad (2.24)$$

in this case. Referring to equation (2.20), it can be seen that the left-hand side of equation (2.24) may also be written,

$$\begin{aligned}
\left\langle \psi_-^{\gamma'} \middle| A_+^\gamma \left(E\right)\right\rangle &= \left\langle \psi_-^{\gamma'} \middle| \int_{-\infty}^\infty dt \exp\left(iEt\right) \mathbf{U}(t) \middle| \psi_+^\gamma \right\rangle \\
&= \int_{-\infty}^\infty dt \exp\left(iEt\right) \left\langle \psi_-^{\gamma'} \middle| \mathbf{U}(t) \middle| \psi_+^\gamma \right\rangle.
\end{aligned} \qquad (2.25)$$

This expresses $\left\langle \psi_-^{\gamma'} \middle| A_+^\gamma \left(E\right)\right\rangle$ as the Fourier transform of the correlation function,

$$C^{\gamma'\gamma}\left(t\right) = \left\langle \psi_-^{\gamma'} \middle| \mathbf{U}(t) \middle| \psi_+^\gamma \right\rangle. \qquad (2.26)$$

The correlation function (2.26) is the inner product of one Møller state and the time evolution of the other Møller state. Both Møller states can be calculated directly by the propagation methods of Chapter III, as applied to equations (2.18) and (2.19). Using equation (2.26), one Møller state is evolved in time from $t = -\infty$ to $t = -\infty$, and its inner product with the other Møller state is evaluated as a function of time. Then the Fourier transform is performed to produce $\left\langle \psi_-^{\gamma'} \middle| A_+^\gamma \left(E\right)\right\rangle$. By rearranging equation (2.24), one

quarter of the S-matrix for the energy range of interest is then given by

$$S_{+k'_{\gamma'},-k_\gamma}^{\gamma';\gamma} = \frac{\hbar}{2\pi} \sqrt{\frac{\left|k'_{\gamma'}\right| \left|k_\gamma\right|}{\mu_{\gamma'}\mu_\gamma}} \frac{\left\langle \psi_-^{\gamma'} \middle| A_+^\gamma (E) \right\rangle}{\eta_-^* \left(+k'_{\gamma'}\right) \eta_+ \left(-k_\gamma\right)}. \tag{2.27}$$

The other three cases, 2 to 4, deliver the rest of the S-matrix, according to the general formula,

$$S_{\pm k'_{\gamma'},\pm k_\gamma}^{\gamma';\gamma} = \frac{\hbar}{2\pi} \sqrt{\frac{\left|k'_{\gamma'}\right| \left|k_\gamma\right|}{\mu_{\gamma'}\mu_\gamma}} \frac{\left\langle \psi_-^{\gamma'} \middle| A_+^\gamma (E) \right\rangle}{\eta_-^* \left(\pm k'_{\gamma'}\right) \eta_+ \left(\pm k_\gamma\right)}, \tag{2.28}$$

providing the remaining three combinations of reactant and product momenta.

III. Computational Methods

The channel-packet method requires time-dependent propagation of wavepackets, first to arrive at the Møller states, then to evaluate the correlation function. A number of methods have been developed (34) to solve the time-dependent Schrödinger equation (2.1) numerically for $|\psi(t)\rangle$. Two such methods, the split-operator and the Lanczos algorithms, are discussed in Sections 3.1 and 3.2. Additional numerical techniques to apply these methods more efficiently to channel-packet calculations are presented in Sections 3.4 and 3.5.

3.1 Split-Operator Propagation

The split-operator scheme of Feit and Fleck originated in a homologous problem in optics(35,36). The technique, suitable for use with time-independent Hamiltonians, is based on the separation of the time-evolution operator into separately-diagonalizable kinetic- and potential-energy portions:

$$
\begin{aligned}
\mathbf{U}(t_0 + \Delta t) &= e^{-i\mathbf{H}\Delta t/\hbar}e^{-i\mathbf{H}t_0/\hbar} \\
&= e^{-i(\mathbf{T}+\mathbf{V})\Delta t/\hbar}\mathbf{U}(t_0) \\
&= e^{-i\mathbf{V}\Delta t/\hbar}e^{-i\mathbf{T}\Delta t/\hbar}e^{-i[\mathbf{T},\mathbf{V}]\Delta t^2/2\hbar^2}\mathbf{U}(t_0) + O(\Delta t^3)
\end{aligned} \tag{3.1}
$$

where $\mathbf{T}$ and $\mathbf{V}$ are kinetic- and potential-energy operators respectively, and $[\mathbf{T},\mathbf{V}] = \mathbf{TV} - \mathbf{VT}$ is their commutator. The Zassenhaus formula(37)

$$
e^{\mathbf{A}+\mathbf{B}} = e^{\mathbf{A}}e^{\mathbf{B}}e^{\frac{1}{2}[\mathbf{B},\mathbf{A}]} + O([\mathbf{A}-\mathbf{B},[\mathbf{A},\mathbf{B}]]) \tag{3.2}
$$

is required in order to obtain equation (3.1), since $\mathbf{T}$ and $\mathbf{V}$, in general, do not commute. The split-operator formulation of the time-evolution operator,

$$
\mathbf{U}(t_0 + \Delta t) = e^{-i\mathbf{V}\Delta t/2\hbar}e^{-i\mathbf{T}\Delta t/\hbar}e^{-i\mathbf{V}\Delta t/2\hbar}\mathbf{U}(t_0) + O\left(\Delta t^3\right), \tag{3.3}
$$

can be derived from a Taylor-series expansion of equation (3.1). Equation (3.3) has the benefit of retaining the second-order accuracy of (3.1) while involving only the two operators $\mathbf{T} = \mathbf{P}^2/2\mu$ and $\mathbf{V}$ by themselves, eliminating the commutator.

3-1

The kinetic-energy evolution operator, $e^{-i\mathbf{T}\Delta t/\hbar} = e^{-i\hbar \mathbf{k}^2 \Delta t/2\mu}$, is diagonal in the momentum representation, and the potential-energy evolution operator, $e^{-i\mathbf{V}\Delta t/2\hbar}$, is diagonal in the coordinate representation. Thus, the effect of the time-evolution operator on a state $|\psi(t_0)\rangle$ over a short interval Δt can be calculated easily with the help of two fast Fourier transforms (FFTs). The Fourier transform and its inverse have the effect of converting vectors back and forth between the momentum and coordinate representations. The calculation

$$
\begin{aligned}
\psi(x, t_0 + \Delta t) &= \langle x|\,\mathbf{U}(\Delta t)\,|\psi(t_0)\rangle \\
&= \langle x|\, e^{-i\mathbf{V}\Delta t/2\hbar} e^{-i\mathbf{T}\Delta t/\hbar} e^{-i\mathbf{V}\Delta t/2\hbar}\,|\psi(t_0)\rangle \\
&= \langle x|\, e^{-i\mathbf{V}\Delta t/2\hbar} \int dx'\,|x'\rangle\langle x'|\int dk\,|k\rangle\langle k|\,e^{-i\mathbf{T}\Delta t/\hbar}\int dk'\,|k'\rangle\langle k'| \\
&\quad \times \int dx''\,|x''\rangle\langle x''|\,e^{-i\mathbf{V}\Delta t/2\hbar}\int dx'''\,|x'''\rangle\langle x'''|\,\psi(t_0)\rangle \\
&= \int dx'\,\langle x|\,e^{-i\mathbf{V}\Delta t/2\hbar}\,|x'\rangle \int dk\,\langle x'\,|k\rangle \int dk'\,\langle k|\,e^{-i\mathbf{T}\Delta t/\hbar}\,|k'\rangle \\
&\quad \times \int dx''\,\langle k'\,|x''\rangle \int dx'''\,\langle x''|\,e^{-i\mathbf{V}\Delta t/2\hbar}\,|x'''\rangle\,\psi(x''', t_0) \\
&= \int dx'\,\delta(x - x')\,e^{-iV(x)\Delta t/2\hbar}\int dk\,\langle x'\,|k\rangle \int dk'\,\delta(k - k')\,e^{-ik^2\Delta t/2\mu\hbar} \\
&\quad \times \int dx''\,\langle k\,|x''\rangle\,e^{-iV(x'')\Delta t/2\hbar}\int dx'''\,\delta(x'' - x''')\,\psi(x''', t_0) \\
&= e^{-iV(x)\Delta t/2\hbar}\frac{1}{\sqrt{2\pi}}\int dk\,e^{ikx}\,e^{-ik^2\Delta t/2\hbar\mu} \\
&\quad \times \frac{1}{\sqrt{2\pi}}\int dx''\,e^{-ikx''}\,e^{-iV(x'')\Delta t/2\hbar}\,\psi(x'', t_0)
\end{aligned}
\tag{3.4}
$$

can be performed using an N-element complex vector to approximate any function $\chi(x, t) = \langle x\,|\chi(t)\rangle$, or its Fourier transform,

$$
\begin{aligned}
\widetilde{\chi}(k, t) &= \langle k\,|\chi(t)\rangle \\
&= \frac{1}{\sqrt{2\pi}}\int_{-\infty}^{\infty} dx\,e^{-ikx}\chi(x, t_0).
\end{aligned}
\tag{3.5}
$$

The diagonal operators $e^{-i\mathbf{V}\Delta t/2\hbar}$ and $e^{-i\mathbf{T}\Delta t/2\hbar}$ can be represented by N-element arrays. At each time step, the wave function is multiplied, element by element, by the diagonal operator elements, $e^{-iV(x_i)\Delta t/2\hbar}$, and the resulting vector transformed to the momentum

representation by FFT. The vector is then multiplied by the diagonal operator $e^{-ik_i^2 \Delta t/2\hbar\mu}$, transformed back to the coordinate representation by inverse FFT, and multiplied by the operator $e^{-iV(x_i)\Delta t/2\hbar}$ again. For a time-independent Hamiltonian, the time evolution of $|\psi(t)\rangle$ can be calculated by repeated applications of equation (3.4), using the same diagonal operators.

3.2 Lanczos Propagation

The split-operator technique is a fast, robust method of obtaining solutions to the time-dependent Schrödinger equation for time-independent Hamiltonians.(34) However, there are cases, as in the interaction picture (see Section 3.5), where the form of the time-evolution operator makes it impractical to separate the evolution operator into portions diagonalizable by FFTs. In such cases, the wavepacket may be propagated by the Lanczos method(44,45). In the Lanczos approach, the Hamiltonian is represented using basis vectors of a Krylov subspace generated by the Hamiltonian. The basis vectors of the Krylov subspace are formed by repeated operation of the Hamiltonian on some initial state $|\phi_0\rangle$:

$$|\varphi_n\rangle = \mathbf{H}^n |\phi_0\rangle. \tag{3.6}$$

It is generally neither necessary nor desirable to use more than a few basis vectors. Commonly, the dimension M of the Krylov subspace is between 5 and 8. An orthonormal set of basis vectors $|q_n\rangle$ is obtained from the non-orthogonal $|\varphi_n\rangle$ using Gram-Schmidt orthogonalization, and used to form an $M \times M$ finite-basis approximation of the Hamiltonian(45),

$$\mathbf{H} \longleftrightarrow H_M = \begin{bmatrix} \alpha_1 & \beta_2 & 0 & \cdots & \cdots & 0 \\ \beta_2 & \alpha_2 & \beta_3 & 0 & \cdots & 0 \\ 0 & \beta_3 & \alpha_3 & \ddots & \ddots & \vdots \\ \vdots & 0 & \ddots & \ddots & \beta_{M-1} & 0 \\ \vdots & \vdots & \ddots & \beta_{M-1} & \alpha_{M-1} & \beta_M \\ 0 & 0 & \cdots & 0 & \beta_M & \alpha_M \end{bmatrix}. \tag{3.7}$$

Matrix elements in equation (3.7) are given by

$$\alpha_n = \langle q_n | \, \mathbf{H} \, | q_n \rangle \, , \tag{3.8}$$

$$\beta_n | q_n \rangle = \mathbf{H} | q_{n-1} \rangle - \alpha_{n-1} | q_{n-1} \rangle - \beta_{n-1}^* | q_{n-2} \rangle \, , \tag{3.9}$$

$$\beta_1 = 0, \; | q_1 \rangle = | \phi_0 \rangle \, , \; | q_0 \rangle = | \, \rangle \, , \tag{3.10}$$

where $| \, \rangle$ is the null vector. The orthonormality of the basis vectors $| q_n \rangle$ is used to derive the subdiagonal values,

$$\beta_n = | \beta_n | = \left\| \mathbf{H} | q_{n-1} \rangle - \alpha_{n-1} | q_{n-1} \rangle - \beta_{n-1} | q_{n-2} \rangle \right\| \, , \tag{3.11}$$

from equation (3.9), employing the norm defined by

$$\| | \chi \rangle \| = \sqrt{\langle \chi \, | \chi \rangle}, \tag{3.12}$$

and choosing all β_n to be real, since employment of the norm renders the phase arbitrary. Within the reduced dimensionality of the Krylov subspace, the Hamiltonian is easily diagonalized. Once the Hamiltonian is diagonalized, the time-evolution operator is readily expressed as a matrix, and the time-evolved state vector,

$$| \psi \left(t + \Delta t \right) \rangle = e^{-i \mathbf{H} \Delta t / \hbar} | \psi \left(t \right) \rangle \, , \tag{3.13}$$

may be expanded in terms of the normalized basis vectors $| q_n \rangle$. This process is iterated to advance the initial state $| \psi \left(t_0 \right) \rangle$ over a sequence of small time steps, in order to arrive at a final state $| \psi \left(t \right) \rangle$.

Suppose the propagation is performed in the momentum representation. Then the evolution from time $t = t_{j-1}$ to $t = t_j$ is expressed,

$$
\begin{aligned}
\langle k \,|\, \psi(t_j) \rangle &= \langle k \,|\, \mathbf{U}(t_j, t_{j-1}) \,|\, \psi(t_{j-1}) \rangle \\
&= \sum_{n=1}^{M} \langle k \,|\, q_n^j \rangle \sum_{m=1}^{M} \langle q_n^j \,|\, \mathbf{U}(t_j, t_{j-1}) \,|\, q_m^j \rangle \langle q_m^j \,|\, \psi(t_{j-1}) \rangle .
\end{aligned}
\tag{3.14}
$$

Here $\left| q_n^j \right\rangle$ denotes the nth Krylov vector in the basis used to represent the Hamiltonian $\mathbf{H}(t_j)$ and generate the state vector $|\psi(t_j)\rangle$. The choice $\left| q_1^j \right\rangle = |\psi(t_{j-1})\rangle$, using the previous time step's state vector to seed the present time step's basis, allows equation (3.14) to be simplified to

$$
\begin{aligned}
\langle k \,|\, \psi(t_j) \rangle &= \sum_{n=1}^{M} \langle k \,|\, q_n^j \rangle \sum_{m=1}^{M} \langle q_n^j \,|\, \mathbf{U}(t_j, t_{j-1}) \,|\, q_m^j \rangle \left\langle q_m^j \,\middle|\, q_1^j \right\rangle \\
&= \sum_{n=1}^{M} \langle k \,|\, q_n^j \rangle \sum_{m=1}^{M} \langle q_n^j \,|\, \mathbf{U}(t_j, t_{j-1}) \,|\, q_m^j \rangle \, \delta_{m1} \\
&= \sum_{n=1}^{M} \langle k \,|\, q_n^j \rangle \left\langle q_n^j \,\middle|\, \mathbf{U}(t_j, t_{j-1}) \,\middle|\, q_1^j \right\rangle .
\end{aligned}
\tag{3.15}
$$

3.3 Computational Bottlenecks

The channel-packet method, based on time-dependent propagation, provides an efficient alternative to time-independent close-coupled type calculations (2–6) for computing S-matrix elements. However, peculiarities of the FFT and the time-dependent behavior of Gaussian wavepackets both may cause the method to require unnecessarily large coordinate grids and attendant long computation times.

The FFT is much faster to calculate than the equivalent discrete Fourier transform for large numbers N of points in space at which functions are evaluated. However, FFTs conflate the origin x_0 and the Nth grid point x_N, artificially imposing periodicity on the potential. A wavepacket which attempts to propagate off the edge of the grid at $x = x_N$ instead "wraps around" and appears on the other side, encountering the potential at $x = 0$ instead of the correct potential at quasi-infinite x. The same problem occurs in the momentum representation for wavepackets, the absolute value of whose momentum begins

to exceed the value that defines the positive or negative edge of the momentum grid. The "wrapping around" of all or part of the momentum representation of the system's wavefunction results in immediate severe degradation of the accuracy of the simulation as the momentum abruptly reverses and takes on the opposite sign. The common, brute-force way to avoid these grid-related errors is to make the grids so large that the wavepackets never approach the edges in either representation. The additional overhead requirement is compounded by the fact that the fastest FFTs constrain the allowed number of grid points N. (In the simplest implementation, the constraint is $N = 2^n$, where n is a natural number.)

Another factor tending to force the grid to be larger is the well-known spatial spreading of Gaussian wavepackets governed by free-particle Hamiltonians(27). For the channel-packet method, this means that grids must be large enough to accommodate spreading, as well as translation, of the product and reactant states as they are propagated backward and forward in time under the asymptotic Hamiltonian. Large grids lead in turn to long computation times for the FFT. Both of these grid-enlarging factors can be ameliorated, and the grid size reduced significantly, through the use of absorbing boundary conditions and the interaction picture.

3.4 Absorbing Boundary Conditions

Absorbing boundary conditions can combat the spurious periodicity of the FFT grid by including an imaginary component in the potential $V(x)$ for values of x near the edges of the grid(23,38–43). A complex potential $\widetilde{V}(x) = V(x) \pm if(x)$, for some real function $f(x)$ that is zero over most of the grid and begins to increase near the edges of the grid, adds a real exponential decay to the forward and reverse time-evolution operators. Careful choice of the function $f(x)$ can assure that the wavepacket is absorbed before it crosses the edge of the grid, and is not reflected or transmitted to any significant degree.

The success of the application of absorbing boundary conditions to the channel-packet method lies in the computation of the correlation function (2.26). The product Møller state $\left| \psi_-^{\gamma'} \right\rangle$ is localized in the interaction region near the origin, so the correlation function $C^{\gamma'\gamma}(t) = \left\langle \psi_-^{\gamma'} \middle| \mathbf{U}(t) \middle| \psi_+^{\gamma} \right\rangle$ need be evaluated only in this restricted region, once

the Møller state has been calculated. Computing the correlation on an FFT grid confined to this region saves time, but leads to invalid results if absorbing boundary conditions are not employed to keep portions of the evolving reactant state $|\psi_+^\gamma(t)\rangle$ which propagate out of the interaction region from "wrapping around" and spuriously returning from the other side. If the imaginary potential is confined to the portion of the grid where the product Møller state is zero, it does not effect the correlation function, so S-matrix elements may be derived correctly despite the altered potential. Calfas and Weeks(23) have demonstrated this technique in two dimensions with absorbing boundary conditions of the form $f(x) = A\exp\left[(x - x_0)^2 / B\right]$ for the collinear $H + H_2 \rightleftharpoons H_2 + H$ reaction, using the Liu-Siegbahn-Truhlar-Horowitz (LSTH) potential(62–64).

3.5 The Interaction Picture

Propagating the wavepackets in the interaction picture can nearly eliminate spreading, as has been confirmed for simple one-dimensional potentials(46–49). The interaction picture has also been applied to molecular predissociation in two and three dimensions, where a single arrangement channel and corresponding Jacobi coordinates are sufficient(50–52). The channel-packet approach allows the interaction picture to be extended for the first time to reactive scattering requiring two arrangement channels.

3.5.1 Essentials of the Interaction Picture.

In the usual (Schrödinger) picture of quantum mechanics, the time-dependent behavior of state vectors is governed by the time evolution operator $\mathbf{U}(t, t_0) = e^{-i\mathbf{H}(t-t_0)/\hbar}$, for time-independent Hamiltonians $\mathbf{H}$. An alternative approach, known as the interaction picture (also called the intermediate or Dirac picture), originated in time-dependent perturbation theory. In time-dependent perturbation theory, the Hamiltonian operator is defined as the sum $\mathbf{H} = \mathbf{H_0} + \mathbf{H_1}$, where $\mathbf{H_0}$ is a time-independent Hamiltonian susceptible of direct analysis, and $\mathbf{H_1}$ is a small, time-dependent perturbation(53). The construction of the interaction picture begins with such a splitting of the Hamiltonian(54).

In the interaction picture, the Hamiltonian is most commonly expressed,

$$\mathbf{H} = \mathbf{H}_0 + \mathbf{V}, \tag{3.16}$$

where $\mathbf{H}_0$ is the asymptotic Hamiltonian $\mathbf{H}_a$ and $\mathbf{V}$ is the potential, as in equation (1.5). However, this is not the only possible expression for the Hamiltonian, and is not necessarily the most useful. Therefore, let us retain the more general notation,

$$\mathbf{H} = \mathbf{H}_0 + \mathbf{H}_1, \tag{3.17}$$

where $\mathbf{H}_0$ is any time-independent portion of the full Hamiltonian. If the time-evolution operator corresponding to $\mathbf{H}_0$ is denoted,

$$\mathbf{U}_0\left(t\right) = e^{-i\mathbf{H}_0 t/\hbar}, \tag{3.18}$$

the transformation from the Schrödinger picture to the interaction picture is

$$\begin{aligned}
|\psi\left(t\right)\rangle_I &= \mathbf{U}_0^\dagger\left(t\right)|\psi\left(t\right)\rangle_S \\
&= e^{i\mathbf{H}_0 t/\hbar}|\psi\left(t\right)\rangle_S,
\end{aligned} \tag{3.19}$$

where the subscript I labels the interaction picture, and the subscript S refers to the Schrödinger picture. It is seen readily from equation (3.19) that $|\psi\left(0\right)\rangle_I = |\psi\left(0\right)\rangle_S$.

The Schrödinger equation in the interaction picture is

$$\begin{aligned}
i\hbar\frac{d}{dt}|\psi\left(t\right)\rangle_I &= i\hbar\frac{d}{dt}\left[\mathbf{U}_0^\dagger\left(t\right)|\psi\left(t\right)\rangle_S\right] \\
&= i\hbar\frac{d\mathbf{U}_0^\dagger\left(t\right)}{dt}|\psi\left(t\right)\rangle_S + i\hbar\mathbf{U}_0^\dagger\left(t\right)\frac{d}{dt}|\psi\left(t\right)\rangle_S \\
&= -\mathbf{U}_0^\dagger\left(t\right)\mathbf{H_0}|\psi\left(t\right)\rangle_S + \mathbf{U}_0^\dagger\left(t\right)\left(\mathbf{H}_0 + \mathbf{H}_1\right)|\psi\left(t\right)\rangle_S \\
&= \mathbf{U}_0^\dagger\left(t\right)\mathbf{H}_1|\psi\left(t\right)\rangle_S \\
&= \mathbf{U}_0^\dagger\left(t\right)\mathbf{H}_1\mathbf{U}_0\left(t\right)|\psi\left(t\right)\rangle_I \\
&= \mathbf{H}_I\left(t\right)|\psi\left(t\right)\rangle_I
\end{aligned} \tag{3.20}$$

where the interaction-picture Hamiltonian is defined as

$$\mathbf{H}_I(t) = \mathbf{U}_0^\dagger(t)\,\mathbf{H}_1\mathbf{U}_0(t). \tag{3.21}$$

In other words, $\mathbf{H}_I(t)$ is constructed in such a way as to make the form of the Schrödinger equation in the interaction picture the same as in the Schrödinger picture. Hence, the formal solutions of the Schrödinger equation in the interaction picture take the analogous form,

$$|\psi(t)\rangle_I = \mathbf{U}_I(t,t_0)\,|\psi(t_0)\rangle_I, \tag{3.22}$$

for some time evolution operator $\mathbf{U}_I(t,t_0)$ and initial state $|\psi(t_0)\rangle_I$. However, since the Hamiltonian $\mathbf{H}_I(t)$ is time-dependent, the simple expression $\mathbf{U}_I(t,t_0) = e^{-i\mathbf{H}_I(t-t_0)/\hbar}$ is not valid. Instead, integration of the Schrödinger equation with the initial condition $\mathbf{U}_I(t_0,t_0) = \mathbf{1}$ gives the perturbation expansion,

$$
\begin{aligned}
\mathbf{U}_I(t,t_0) &= \mathbf{1} + \frac{-i}{\hbar}\int_{t_0}^{t}\mathbf{H}_I(t')\,\mathbf{U}_I(t'-t_0)\,dt' \\
&= \mathbf{1} + \frac{-i}{\hbar}\int_{t_0}^{t}\mathbf{H}_I(t')\,dt' + \left(\frac{-i}{\hbar}\right)^2\int_{t_0}^{t}\int_{t_0}^{t'}\mathbf{H}_I(t')\,\mathbf{H}_I(t'')\,dt''dt' + \cdots
\end{aligned}
\tag{3.23}
$$

so called because its most common application lies in time-dependent perturbation theory. In perturbation theory, the time-dependent portion of the Hamiltonian is, by construction, small enough that the series (3.23) converges within the first few terms. For the interaction Hamiltonian, the truncated perturbation series may not be of sufficient accuracy for a given time interval $\Delta t = t - t_0$. The Magnus expansion,

$$\mathbf{U}_I(t,t_0) = \mathbf{1} + \left(\frac{-i}{\hbar}\right)\int_{t_0}^{t}\mathbf{H}_I(t')\,dt' + \frac{1}{2}\left(\frac{-i}{\hbar}\right)^2\int_{t_0}^{t}\int_{t_0}^{t'}\left[\mathbf{H}_I(t'),\mathbf{H}_I(t'')\right]dt''dt' + \dots,$$
$$\tag{3.24}$$

is a way to redress the convergence problem(55,56). The commutator,

$$\left[\mathbf{H}_I(t'),\mathbf{H}_I(t'')\right] = \mathbf{H}_I(t')\,\mathbf{H}_I(t'') - \mathbf{H}_I(t'')\,\mathbf{H}_I(t') \tag{3.25}$$

in equation (3.24), can be eliminated by using the equivalent expansion(57)

$$\mathbf{U}_I\left(t, t_0\right) = 1 - \frac{i}{\hbar} \int_{t_0}^{t} \mathbf{H}_I\left(t'\right) dt' \tag{3.26}$$

$$- \frac{1}{2\hbar^2} \int_{t_0}^{t} \int_{t_0}^{t} \left(\mathbf{H}_I\left(t'\right)\mathbf{H}_I\left(t''\right) - 2\Theta\left(t'' - t'\right)\mathbf{H}_I\left(t''\right)\mathbf{H}_I\left(t'\right)\right) dt''dt' + \cdots,$$

where $\Theta\left(t'' - t'\right)$ represents a Heaviside step function. In time-dependent numerical methods employing small-enough time steps Δt, first-order truncations of the series (3.23), (3.24), and (3.26) are equivalent and accurate. If the numerical propagator employs time steps that are large enough to require a second-order truncation, equations (3.24) and (3.26) provide the better approximation.

The relationship between the interaction- and Schrödinger-picture time-evolution operators follows from the definition of the interaction-picture state vector (equation (3.19)),

$$\begin{aligned}
|\psi\left(t\right)\rangle_I &= \mathbf{U}_0^\dagger\left(t\right) |\psi\left(t\right)\rangle_S \\
&= \mathbf{U}_0^\dagger\left(t\right) \mathbf{U}\left(t, t_0\right) |\psi\left(t_0\right)\rangle_S \\
&= \mathbf{U}_0^\dagger\left(t\right) \mathbf{U}\left(t, t_0\right) \mathbf{U}_0\left(t_0\right) |\psi\left(t_0\right)\rangle_I.
\end{aligned} \tag{3.27}$$

Hence, the time-evolution operator in the interaction picture can be written

$$\mathbf{U}_I(t, t_0) = \mathbf{U}_0^\dagger\left(t\right) \mathbf{U}\left(t, t_0\right) \mathbf{U}_0\left(t_0\right). \tag{3.28}$$

3.5.1.1 Alternative Formulations of the Interaction Picture. The construction of the terms $\mathbf{H}_0$ and $\mathbf{H}_1$ is worth a moment of consideration. Since the time evolution of a state in the Schrödinger picture occurs as

$$|\psi\left(t\right)\rangle_S = \exp\left[-i\left(\mathbf{H}_0 + \mathbf{H}_1\right)\left(t - t_0\right)/\hbar\right] |\psi\left(t_0\right)\rangle, \tag{3.29}$$

much of the spreading effect of the asymptotic Hamiltonian is counteracted in the time evolution of the interaction-picture state if the choice $\mathbf{H}_0 = \mathbf{H}_a$ is made. This is why the interaction picture is usually constructed this way. Another attractive choice is $\mathbf{H}_0 = \mathbf{T} = \sum_i \left(\hbar^2 \mathbf{k}_i^2/2\mu_i\right)$, the kinetic-energy operator, which simplifies the calculation of the interac-

tion Hamiltonian $\mathbf{H}_I = e^{i\mathbf{H}_0 t/\hbar} \mathbf{H}_1 e^{-i\mathbf{H}_0 t/\hbar}$ by making $\mathbf{H}_0$ and $\mathbf{H}_1$ functions of momentum and position alone. The same advantage accrues if $\mathbf{H}_0 = \mathbf{H}_{rel} = \hbar^2 \mathbf{k}_\gamma^2 / 2\mu_\gamma$ is chosen. The three choices, $\mathbf{H}_0 = \mathbf{H}_a$, $\mathbf{H}_0 = \mathbf{T}$, and $\mathbf{H}_0 = \mathbf{H}_{rel}$, are equivalent in one dimension, where $\mathbf{H}_a = \mathbf{T} = \mathbf{H}_{rel}$.

Two additional considerations affect the choice of $\mathbf{H}_0$. First, if, as in perturbation theory, the effect of $\mathbf{H}_1$ is small compared to that of $\mathbf{H}_0$, larger time steps may be taken in numerical propagations in the interaction picture(49,50). This favors $\mathbf{H}_0 = \mathbf{H}_a$, putting as much of the Hamiltonian into $\mathbf{H}_0$ as possible. Second, however, the interaction-picture methods that are the most successful in reducing computational grid size (the nested interaction pictures described in Section 3.5.4), are implemented using Lanczos propagation, which depends on diagonality of $\mathbf{H}_0$ in the momentum representation in the construction of Krylov basis vectors. In more than one dimension, therefore, the best choice of terms is generally *not* $\mathbf{H}_0 = \mathbf{H}_a$. This issue is discussed further in Section 3.5.3.

3.5.2 Scattering in the Interaction Picture.   The Møller states illustrate the application of the interaction picture to time-dependent scattering. Since Møller states are defined in the Schrödinger picture at time $t = 0$, they are equal to their counterparts in the interaction picture:

$$\left| \psi_\pm \right\rangle_I = \left| \psi_\pm \right\rangle_S .$$

(3.30)

For the same reason, the asymptotic reactant and product states are likewise invariant:

$$\left| \psi_{in(out)}^\gamma \right\rangle_I = \left| \psi_{in(out)}^\gamma \right\rangle_S .$$

(3.31)

Therefore, for example,

$$
\begin{aligned}
\left| \psi_+ \right\rangle_I &= \left| \psi_+ \right\rangle_S = \Omega_{+S}^\gamma \left| \psi_{in}^\gamma \right\rangle_S \\
&= \lim_{t \to -\infty} \mathbf{U}^\dagger (t,0) \, \mathbf{U}_a^\gamma (t) \left| \psi_{in}^\gamma \right\rangle_S \\
&= \mathbf{U}_0^{\gamma\dagger} (0) \lim_{t \to -\infty} \mathbf{U} (0,t) \, \mathbf{U}_a^\gamma (t) \left| \psi_{in}^\gamma \right\rangle_I \\
&\approx \mathbf{U}_0^\dagger (0) \, \mathbf{U} (0,-\tau) \, \mathbf{U}_a^\gamma (-\tau) \left| \psi_{in}^\gamma \right\rangle_I ,
\end{aligned}
$$

(3.32)

where the unit operator $\mathbf{U}_0^\dagger(0)$ is introduced to suggest the form of equation (3.28). The general form of the Møller operators in the interaction picture is

$$\Omega_{\pm I}^\gamma = \lim_{t \to \mp\infty} \mathbf{U}_0^\dagger(0)\, \mathbf{U}(0,t)\, \mathbf{U}_a^\gamma(t). \tag{3.33}$$

Here, our choice of the operator $\mathbf{H}_0$ comes into play. If the selection $\mathbf{H}_0 = \mathbf{H}_a^\gamma$ is made, then $\mathbf{U}_a^\gamma(t) = \mathbf{U}_0(t)$, and equation (3.33) gives

$$\begin{aligned}
\Omega_{\pm I}^\gamma &= \lim_{t \to \mp\infty} \mathbf{U}_0^\dagger(0)\, \mathbf{U}(0,t)\, \mathbf{U}_0(t) \\
&= \lim_{t \to \mp\infty} \mathbf{U}_I(0,t).
\end{aligned} \tag{3.34}$$

Another potentially useful alternative is to choose $\mathbf{H}_0 = \mathbf{H}_{rel}^\gamma$, in the sense of equation (1.16). Since $\mathbf{H}_{rel}^\gamma$ and $\mathbf{H}_{int}^\gamma$ commute, equation (3.33) can be written,

$$\begin{aligned}
\Omega_{\pm I}^\gamma &= \lim_{t \to \mp\infty} \mathbf{U}_0^\dagger(0)\, \mathbf{U}(0,t)\, \mathbf{U}_0(t)\, \mathbf{U}_{int}^\gamma(t) \\
&= \lim_{t \to \mp\infty} \mathbf{U}_I(0,t)\mathbf{U}_{int}^\gamma(t),
\end{aligned} \tag{3.35}$$

where $\mathbf{U}_{int}^\gamma(t) = \exp\left(-i\mathbf{H}_{int}^\gamma t/\hbar\right)$. The action of these Møller operators on channel packets $\left|\psi_{in(out)}^\gamma\right\rangle$ gives the Møller states

$$\begin{aligned}
\left|\psi_\pm\right\rangle_I &= \Omega_{\pm I}^\gamma \left|\psi_{in(out)}^\gamma\right\rangle \\
&= \lim_{t \to \mp\infty} \mathbf{U}_I(0,t)e^{i\mathbf{H}_{int}^\gamma t/\hbar}\left|\psi_{in(out)}^\gamma\right\rangle \\
&= \lim_{t \to \mp\infty} \mathbf{U}_I(0,t)e^{iE_\gamma t/\hbar}\left|\psi_{in(out)}^\gamma\right\rangle \\
&\approx e^{\mp iE_\gamma \tau/\hbar}\mathbf{U}_I(0,\mp\tau)\left|\psi_{in(out)}^\gamma\right\rangle.
\end{aligned} \tag{3.36}$$

Thus, with the appropriate choice of $\mathbf{H}_0$, the Møller operators become simple propagations in the interaction picture, possibly with a phase shift.

3.5.3 Wavepacket Propagation in the Interaction Picture.

Numerical propagation in the interaction picture is not a trivial problem, considering the form (3.21) of the Hamiltonian. Interaction-picture state vectors do not lend themselves to split-operator

propagation. Consider a simple first-order split-operator type propagation over a single time step, choosing $\mathbf{H}_0 = \mathbf{H}_{rel}^\gamma$:

$$
\begin{aligned}
|\psi(t_0 + \Delta t)\rangle_I &\approx \exp\left\{-\frac{i}{\hbar}\mathbf{H}_I\left(t_0 + \frac{\Delta t}{2}\right)\Delta t\right\}|\psi(t_0)\rangle \\
&= \exp\left\{-\frac{i\Delta t}{\hbar}e^{i(t_0+\Delta t/2)\mathbf{H}_{rel}^\gamma/\hbar}\mathbf{H}_{int}^\gamma e^{-i(t_0+\Delta t/2)\mathbf{H}_{rel}^\gamma/\hbar}\right\}|\psi(t_0)\rangle \\
&= \exp\left\{-\frac{i\Delta t}{\hbar}e^{i\hbar(t_0+\Delta t/2)\mathbf{k}_r^2/2m_\gamma}\left[\frac{\hbar^2\mathbf{k}_R^2}{2\mu_\gamma} + \mathbf{V}_\gamma(r_\gamma, R_\gamma)\right]\right. \\
&\qquad\qquad\left.\times e^{-i\hbar(t_0+\Delta t/2)\mathbf{k}_r^2/2m_\gamma}\right\}|\psi(t_0)\rangle \qquad\qquad (3.37)\\
&= \exp -\left\{\frac{i\Delta t\hbar\mathbf{k}_R^2}{2\mu_\gamma} - \frac{i\Delta t}{\hbar}e^{i\hbar(t_0+\Delta t/2)\mathbf{k}_r^2/2m_\gamma}\right. \\
&\qquad\qquad\left.\times\mathbf{V}_\gamma(r_\gamma, R_\gamma)e^{-i\hbar(t_0+\Delta t/2)\mathbf{k}_r^2/2m_\gamma}\right\}|\psi(t_0)\rangle \\
&= e^{-i\Delta t\hbar\mathbf{k}_R^2/4\mu_\gamma}\exp\left\{-\frac{i\Delta t}{\hbar}e^{i\hbar(t_0+\Delta t/2)\mathbf{k}_r^2/2m_\gamma}\right. \\
&\qquad\qquad\left.\times\mathbf{V}_\gamma(r_\gamma, R_\gamma)e^{-i\hbar(t_0+\Delta t/2)\mathbf{k}_r^2/2m_\gamma}\right\}e^{i\Delta t\hbar\mathbf{k}_R^2/4\mu_\gamma}|\psi(t_0)\rangle.
\end{aligned}
$$

The outer operators, $e^{\pm i\Delta t\hbar\mathbf{k}_R^2/4\mu_\gamma}$, are directly diagonalizable, but the inner exponential is not. Alternative formulations of the interaction picture fail to eliminate this problem. Thus, beneficial use of the interaction picture requires a finite-basis approach like the Lanczos method of Section 3.2, whereby the evolution operator $\mathbf{U}_I(\tau)$ may be diagonalized as a single entity.

The Lanczos approach is workable, though cumbersome unless further refinements are added. The computation of the Krylov basis vectors $\left|q_n^j\right\rangle$ via equation (3.9) involves evaluating the vectors

$$
\mathbf{H}_I(t_j)\left|q_n^j\right\rangle_I = \mathbf{U}_0^\dagger(t_j)\mathbf{H}_1\mathbf{U}_0(t_j)\left|q_n^j\right\rangle_I, \qquad\qquad (3.38)
$$

which, if taken head-on, implies propagation of the state vector under $\mathbf{H}_0$. The effect of equation (3.38) is to convert $\left|q_n^j\right\rangle_I$ to the Schrödinger picture, operate upon it with $\mathbf{H}_1$, and convert the result back to the interaction picture. If $\mathbf{H}_0$ is not a free-particle type Hamiltonian, each conversion back and forth involves a propagation over the full time t_j, not just the incremental time Δt. What is worse, this double propagation must be done M

times for each time step in order to obtain all of the Krylov vectors. Therefore, formulations of the interaction picture wherein $\mathbf{H}_0$ is not a function of momentum alone incur far too much computational overhead to be useful, even when compared to Schrödinger-picture propagations on much larger grids. For free-particle type $\mathbf{H}_0$, propagation is not necessary in the formation of the basis vectors, but the implicit conversion to the Schrödinger picture means no reduction in grid size is achieved, since the full spreading effect of $\mathbf{U}_0(\tau)$ is ultimately incurred before being reversed.

The direct "sequential" approach just described to computation of Krylov vectors makes Lanczos propagation in the interaction picture much slower than propagation in the Schrödinger picture using the same grid and time step. One possible way around this obstacle is the finite-basis approach, which spreads wavepackets only over short time intervals and does not use Fourier transforms. The finite-basis approach is a new idea, developed early in the course of this research project, which failed to find a stable computational implementation. The theory and some computational results of the finite-basis approach are described in Section 4.3. A better-developed idea that has, in contrast, proved computationally robust, is the nested interaction picture.

3.5.4 Nested Interaction Pictures. Tannor and others have observed that a reduction in the number of required grid points in the interaction picture can be achieved by optimizing the grid width in momentum space, or the grid-point *spacing* in coordinate space(49). They named their invention the nested interaction picture because the Hamiltonian becomes sandwiched between one or two additional pairs of operators.

Two forms of nested interaction pictures have been developed: the so-called P-adapted and PR-adapted varieties. In the P-adapted picture, the state vector is

$$
\begin{aligned}
|\psi\rangle_I' &= e^{-i\langle\mathbf{P}\rangle\mathbf{R}_S/\hbar}\,|\psi\rangle_I \\
&= e^{-i\langle\mathbf{P}\rangle\mathbf{R}_S/\hbar}e^{i\mathbf{H}_0 t/\hbar}\,|\psi\rangle_S,
\end{aligned}
\tag{3.39}
$$

where the expectation value of the momentum operator,

$$
\begin{aligned}
\langle \mathbf{P} \rangle &= \langle \psi |_I \, \mathbf{P}_I \, | \psi \rangle_I \\
&= \langle \psi |_S \, e^{-i\mathbf{H}_0 t/\hbar} e^{i\mathbf{H}_0 t/\hbar} \mathbf{P}_S e^{-i\mathbf{H}_0 t/\hbar} e^{i\mathbf{H}_0 t/\hbar} \, | \psi \rangle_S \\
&= \langle \psi |_S \, \mathbf{P}_S \, | \psi \rangle_S \,,
\end{aligned}
\tag{3.40}
$$

is taken to be constant for the duration of a single time step. The unitary transformation $e^{i\langle \mathbf{P} \rangle \mathbf{R}_S/\hbar}$ has the effect of shifting the state vector in such a way as to make its average momentum zero. The P-adapted state vector obeys the wave equation

$$
i\hbar \frac{d}{dt} | \psi \rangle_I' = \mathbf{H}' \, | \psi \rangle_I' \,,
\tag{3.41}
$$

where

$$
\mathbf{H}' = e^{-i\langle \mathbf{P} \rangle \mathbf{R}_S/\hbar} e^{i\mathbf{H}_0 t/\hbar} \mathbf{H}_1 \left(\mathbf{R}_S \right) e^{-i\mathbf{H}_0 t/\hbar} e^{i\langle \mathbf{P} \rangle \mathbf{R}_S/\hbar} \,.
\tag{3.42}
$$

The PR-adapted picture shifts the origins of both the momentum and the coordinate representations, defining the state vector,

$$
\begin{aligned}
| \psi \rangle_I'' &= e^{i\langle \mathbf{R} \rangle \mathbf{P}_S/\hbar} \, | \psi \rangle_I' \\
&= e^{i\langle \mathbf{R} \rangle \mathbf{P}_S/\hbar} e^{-i\langle \mathbf{P} \rangle \mathbf{R}_S/\hbar} e^{i\mathbf{H}_0 t/\hbar} \, | \psi \rangle_S \,,
\end{aligned}
\tag{3.43}
$$

where $\langle \mathbf{R} \rangle = \langle \psi |_I \, \mathbf{R}_I \, | \psi \rangle_I = \langle \psi |_S \, \mathbf{R}_S \, | \psi \rangle_S$ is the expectation value of the position operator. The PR-adapted equation of motion is given by

$$
i\hbar \frac{d}{dt} | \psi \rangle_I'' = \mathbf{H}'' \, | \psi \rangle_I'' \,,
\tag{3.44}
$$

where

$$
\mathbf{H}'' = e^{i\langle \mathbf{R} \rangle \mathbf{P}_S/\hbar} e^{-i\langle \mathbf{P} \rangle \mathbf{R}_S/\hbar} e^{i\mathbf{H}_0 t/\hbar} \mathbf{H}_1 \left(\mathbf{R}_S \right) e^{-i\mathbf{H}_0 t/\hbar} e^{i\langle \mathbf{P} \rangle \mathbf{R}_S/\hbar} e^{-i\langle \mathbf{R} \rangle \mathbf{P}_S/\hbar} \,.
\tag{3.45}
$$

Wavepackets can be propagated using fewer grid points in the nested interaction picture because they always remain centered on the grid. Translation of the wavepacket is corrected for, but at intermediate points in the calculations the wavepackets still may be spread by the effect of U_0. Further overhead is introduced by the necessity of calculating the expectation values $\langle R \rangle$ and $\langle P \rangle$ for every time step, then using them to update both the state vector (3.43) and the Hamiltonian (3.45). This is described in detail in Section 5.1. In some cases, the nested Hamiltonian may be simplified using what Tannor's group calls the Heisenberg approach. The Heisenberg approach requires an analytical expression for the potential, and may fall victim to undersampling of the potential. The underlying reasoning and some computational results of the Heisenberg approach are described in Section 4.2. The most accurate and reliable version of the nested interaction picture is the simplest, so-called "sequential," approach. The sequential method accepts the computational overhead described above, leading to computational times which may be several times longer than an equivalent Schrödinger-picture propagation in one dimension. The sequential nested interaction picture, however, does enable accurate computations using reduced grid sizes compared to propagation in the Schrödinger picture. This is demonstrated in Chapters V and VI.

IV. Alternative Computational Implementations of the Interaction Picture

Three approaches to the interaction picture were investigated in the course of this project that failed, either to yield reliably accurate results, or to promise any computational advantage over the Schrödinger picture. The sequential approach is the simplest, and is the equal of the Schrödinger split-operator method in stability and accuracy, but requires the same grid size and more computational time than the split-operator method. Tannor's so-called "Heisenberg" approach can reduce grid and computation-time requirements, but requires an analytic expression for the potential and is not accurate for many interaction potentials. A new approach was also developed and investigated, and named the "finite-basis approach." This approach proved to be computationally unstable.

4.1 The Sequential Method

The non-nested sequential approach was investigated early, not on the basis of any possibility of computational advantage, but simply to verify the claim of Section 3.5.2 that Møller states can be computed by single interaction-picture propagations. The sequential process uses the Lanczos propagation scheme of Section 3.2 to diagonalize a finite-basis approximation of the interaction-picture Hamiltonian,

$$\mathbf{H}_I\left(t\right) = \mathbf{U}_0^\dagger\left(t\right)\mathbf{H}_1\mathbf{U}_0\left(t\right). \tag{4.1}$$

As noted in Section 3.5.3, the diagonalization process for this Hamiltonian requires the same grid needed for the Schrödinger picture. However, it is comparatively simple to implement, particularly to first order, and serves to show that accurate Møller states do result from propagations of asymptotic states in the interaction picture.

This is demonstrated by the computation of Møller states of the square-well potential of Figure 4.1. The figure shows the positive-momentum reactant Møller state $\left\langle x\left|\psi_+\right\rangle_S\right.$, computed in the Schrödinger picture using a split-operator propagator, based on the parameters set out in Table 4.1. Figure 4.2 shows the same Møller state of the square well, also computed using the parameters stated in Table 4.1 in the interaction picture with a first-order Lanczos propagator and a four-vector Krylov basis. The reactant and product
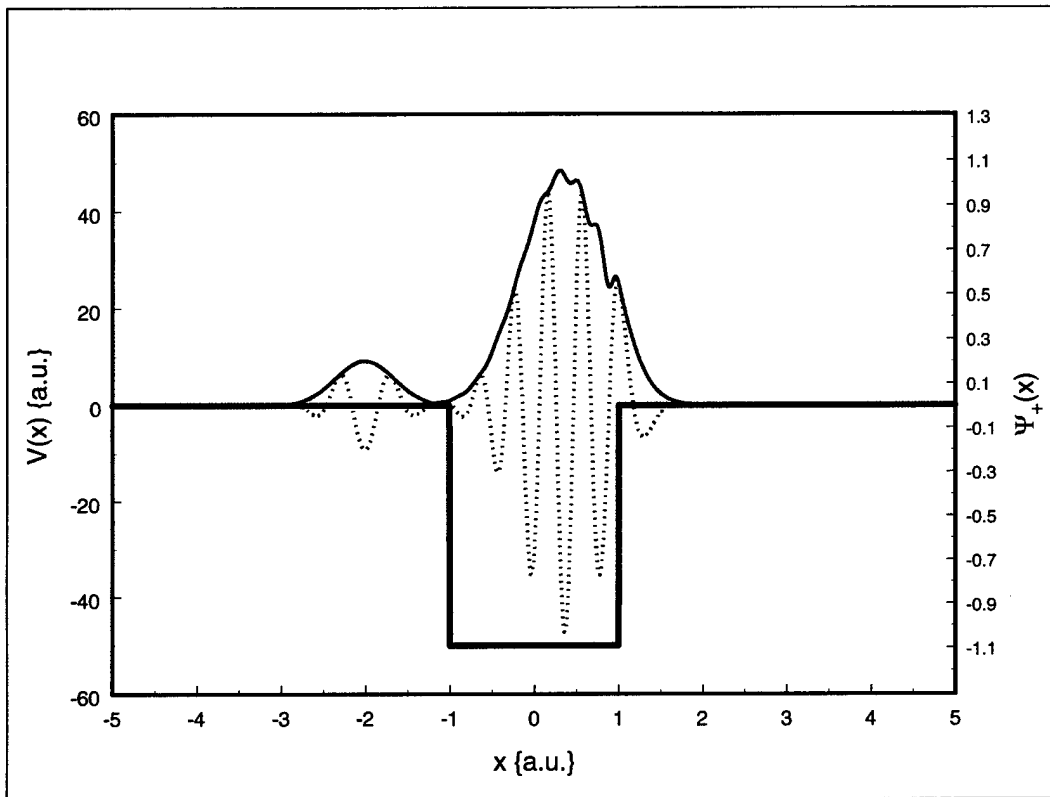
Figure 4.1   The reactant Møller state $\Psi_+\left(x\right)$, computed in the Schrödinger picture for the square-well potential represented by the heavy solid line. The dotted line represents the real part of the wavefunction; the thin solid line its modulus, $\sqrt{\langle\Psi_+\,|\Psi_+\rangle}$.
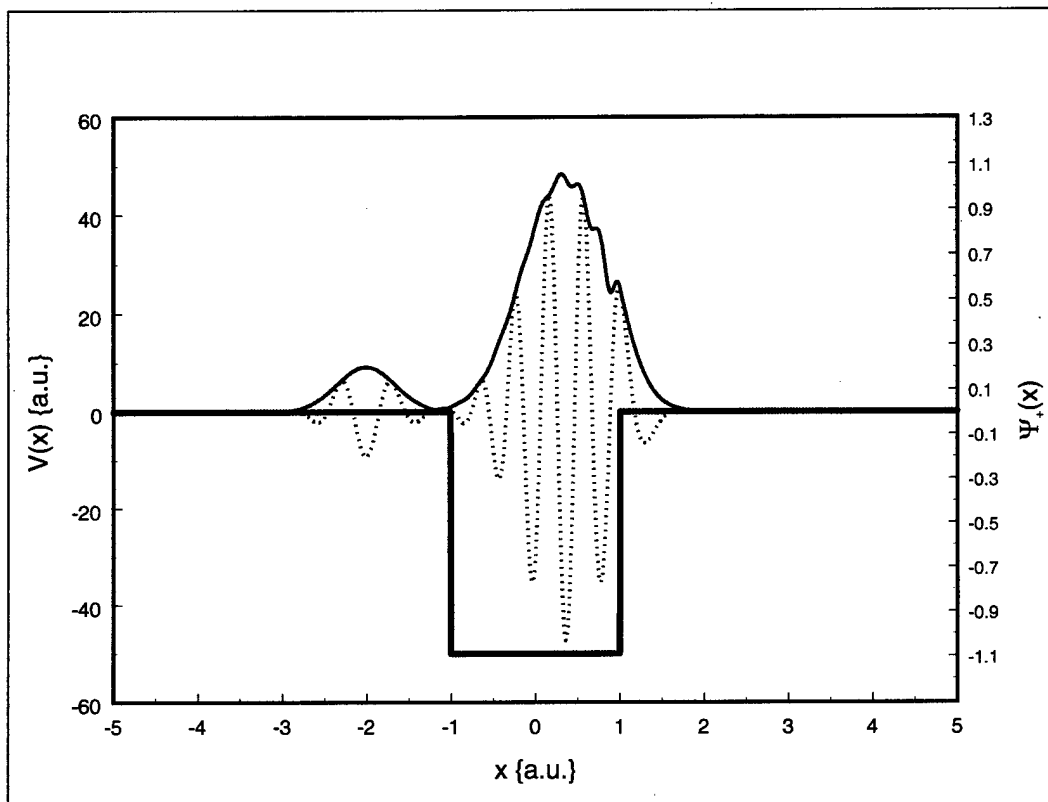
Figure 4.2   The reactant Møller state $\Psi_+(x)$, computed in the interaction picture for the square-well potential represented by the heavy solid line. The dotted line represents the real part of the wavefunction; the thin solid line its modulus, $\sqrt{\langle \Psi_+ | \Psi_+ \rangle}$.

states computed in the two pictures can be compared as to amplitude and phase, according to the following criteria. After Tannor et al.(49), the amplitude error is given by

$$\epsilon_A = \left| 1 - \left(a^2 + b^2 \right) \right|, \tag{4.2}$$

and the phase error by

$$\epsilon_\Phi = \left| \tan^{-1} \left(\frac{b}{a} \right) \right|, \tag{4.3}$$

Quantity	Variable	Value
Coordinate grid spacing	Δx	.005
Grid size	N	4096
Asymptotic time	τ	0.45
Reduced mass	μ	1.0
Time step size	Δt	0.001
Initial state position	x_0	0.0
Initial state momentum	k_0	11.3
Initial Gaussian width parameter	σ	0.25

Table 4.1 Parameters used to generate the Møller states in Figures 4.1 and 4.2. All quantities are in atomic units.

where a and b are the real and imaginary parts of the overlap of the respective wavefunctions—i.e., $\langle \psi_I^{\pm} | \psi_S^{\pm} \rangle = a + ib$. The pairs of Møller states illustrated have amplitude error $\epsilon_A = 3.7 \cdot 10^{-6}$ and phase error $\epsilon_\Phi = 4.2 \cdot 10^{-3}$.

In the Schrödinger picture, the process of computing the Møller states involves propagating the reactant state back to time $-\tau$ and the product state forward to time $+\tau$. As illustrated in Figure 4.3, this drives the requirement for a grid larger than that which would be needed to support only the initial and Møller states.

In the interaction picture, in contrast, the intermediate states are identical to the initial states, since this propagation is done using a free-particle potential. The Møller states evolve directly as single propagations from time $t = \pm\tau$ to $t = 0$. Were it not for the internal workings of the sequential method, the interaction picture would thus support the entire computation on a smaller grid. However, the sequential wavefunction $|\psi(t)\rangle$ is computed directly as

$$
\begin{aligned}
|\psi(t)\rangle_I &= \mathbf{U}_0^\dagger(t) |\psi(t)\rangle_S \\
&= \mathbf{U}_0^\dagger(t) \mathbf{U}(t,0) \mathbf{U}_0(0) |\psi(0)\rangle_I \\
&= \mathbf{U}_0^\dagger(t) \mathbf{U}(t,0) |\psi(0)\rangle_S \\
&= \mathbf{U}_0^\dagger(t) |\psi(t)\rangle_S .
\end{aligned}
\tag{4.4}
$$
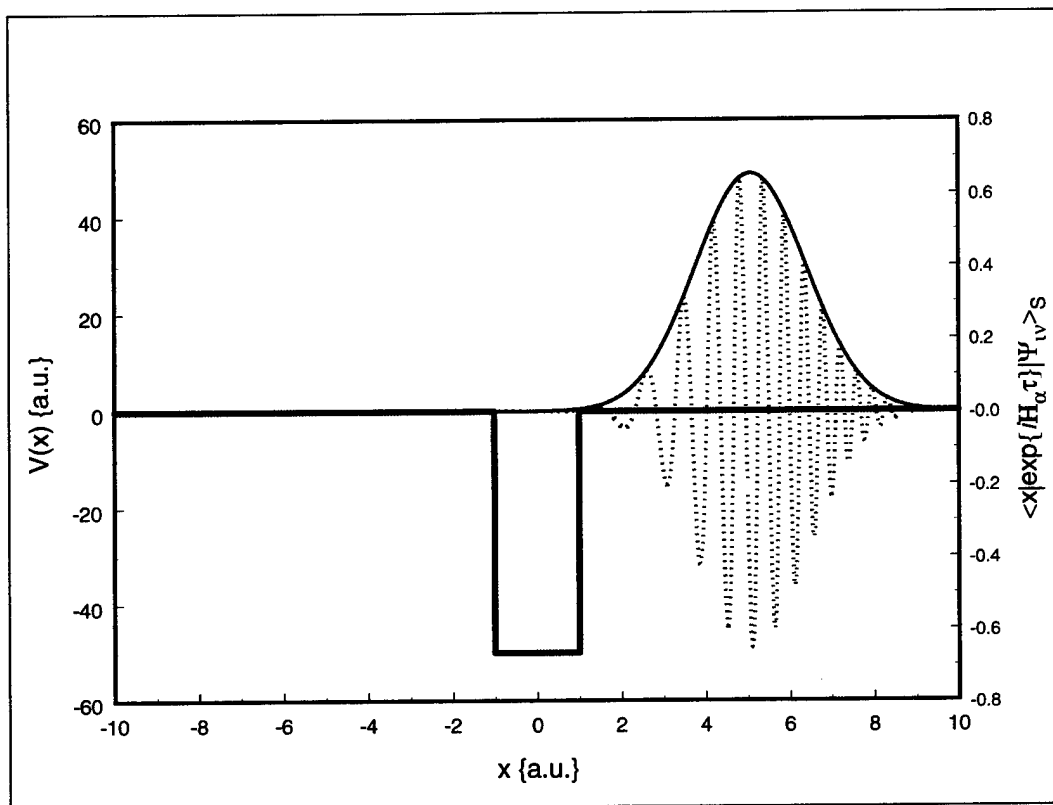
Figure 4.3   The intermediate state $\left\langle x \left| e^{-iH_0(-\tau)} \right| \Psi_{in} \right\rangle_S$ at time $-\tau = -4.5$ atomic units.

Thus at time $\pm\tau$, the intermediate states $\left|\psi^{\pm}\left(\tau\right)\right\rangle_I$ are in fact derived from the very states $\left|\psi^{\pm}\left(\tau\right)\right\rangle_S$ depicted in Figure 4.3, and therefore require the same grid size as the Schrödinger picture.

4.2 The "Heisenberg" Method

Tannor's "Heisenberg" approach succeeds in bypassing the Schrödinger picture and trimming the computational grid requirements for Møller states in the interaction picture(49). Tannor named the method "Heisenberg" because of the similarity of the equations of motion of its position and momentum operators to the Heisenberg picture's. It is not, however, a true Heisenberg picture; therefore here the name appears in quotation marks. The "Heisenberg" approach is based on manipulation of an analytic expression of the Hamiltonian, using a number of operator identities. The construction of the time-evolution operator in the method begins with a reformulated potential and Hamiltonian.

4.2.1 The "Heisenberg" Potential. Consider a full, N-dimensional, channel Hamiltonian in Jacobi coordinates,

$$\mathbf{H}_S^{\gamma} = \sum_{j=1}^{N} \frac{\mathbf{P}_{Sj}^2}{2\mu_j} + V\left(\overline{\mathbf{R}}_S\right), \qquad (4.5)$$

where the operator $\overline{\mathbf{R}}_S$ includes both internal and external coordinates. Let a generic operator $\mathbf{H}_0^{\gamma}$ be defined as the sum of any portion of the kinetic-energy operator and some analytic portion, $\Phi\left(\overline{\mathbf{R}}_S\right) = \sum_{j=1}^{N}\sum_{n=1}^{M} \phi_{jn}\mathbf{R}_{Sj}^n$, of the potential operator:

$$\mathbf{H}_0^{\gamma} = \sum_{j=1}^{L} \frac{\mathbf{P}_{Sj}^2}{2\mu_j} + \Phi\left(\overline{\mathbf{R}}_S\right). \qquad (4.6)$$

The equation of motion for an interaction-picture operator $\mathbf{O}_I\left(t\right) = e^{i\mathbf{H}_0 t/\hbar}\mathbf{O}_S e^{-i\mathbf{H}_0 t/\hbar}$ is

$$\begin{aligned}
i\hbar\frac{d}{dt}\mathbf{O}_I &= i\hbar\left(\frac{i}{\hbar}\mathbf{H}_0\right)\mathbf{O}_I + i\hbar\mathbf{O}_I\left(\frac{-i}{\hbar}\mathbf{H}_0\right) \\
&= [\mathbf{O}_I, \mathbf{H}_0^{\gamma}].
\end{aligned} \qquad (4.7)$$

Therefore, the time evolution of a position operator $\mathbf{R}_{Im} = e^{i\mathbf{H}_0 t/\hbar} \mathbf{R}_{Sm} e^{-i\mathbf{H}_0 t/\hbar}$ is given by

$$
\begin{aligned}
\frac{d}{dt}\mathbf{R}_{Im} &= \frac{i}{\hbar}\left[\mathbf{H}_0^\gamma, \mathbf{R}_{Im}\right] \\
&= \frac{i}{\hbar}\left[\sum_{j=1}^{L}\frac{\mathbf{P}_{Sj}^2}{2\mu_j} + \Phi\left(\overline{\mathbf{R}}_S\right), e^{i\mathbf{H}_0 t/\hbar}\mathbf{R}_{Sm}e^{-i\mathbf{H}_0 t/\hbar}\right] \\
&= \frac{i}{\hbar}e^{i\mathbf{H}_0 t/\hbar}\left[\sum_{j=1}^{L}\frac{\mathbf{P}_{Sj}^2}{2\mu_j} + \Phi\left(\overline{\mathbf{R}}_S\right), \mathbf{R}_{Sm}\right]e^{-i\mathbf{H}_0 t/\hbar} \\
&= \frac{i}{2\hbar}e^{i\mathbf{H}_0 t/\hbar}\sum_{j=1}^{L}\left[\frac{\mathbf{P}_{Sj}^2}{\mu_j}, \mathbf{R}_{Sm}\right]e^{-i\mathbf{H}_0 t/\hbar} \\
&= \frac{i}{2\hbar}e^{i\mathbf{H}_0 t/\hbar}\left[\frac{\mathbf{P}_{Sm}^2}{\mu_m}, \mathbf{R}_{Sm}\right]e^{-i\mathbf{H}_0 t/\hbar} \\
&= \frac{i}{2\hbar}e^{i\mathbf{H}_0 t/\hbar}\left\{\frac{-i2\hbar}{\mu_m}\mathbf{P}_{Sm}\right\}e^{-i\mathbf{H}_0 t/\hbar} \\
&= \frac{1}{\mu_m}\mathbf{P}_{Im}.
\end{aligned}
\tag{4.8}
$$

The derivation of equation (4.8) uses the commutator relations

$$
\begin{aligned}
\left[\mathbf{P}_j^2, \mathbf{R}_m\right] &= \left(\mathbf{P}_j\mathbf{P}_j\mathbf{R}_m - \mathbf{R}_m\mathbf{P}_j\mathbf{P}_j\right)\delta_{jm} \\
&= \left(\mathbf{P}_m\mathbf{P}_m\mathbf{R}_m - \mathbf{P}_m\mathbf{R}_m\mathbf{P}_m + \mathbf{P}_m\mathbf{R}_m\mathbf{P}_m - \mathbf{R}_m\mathbf{P}_m\mathbf{P}_m\right) \\
&= \left(\mathbf{P}_m\left[\mathbf{P}_m, \mathbf{R}_m\right] + \left[\mathbf{P}_m, \mathbf{R}_m\right]\mathbf{P}_m\right) \\
&= -i2\hbar\mathbf{P}_m,
\end{aligned}
\tag{4.9}
$$

$$
\left[\Phi\left(\mathbf{R}_j\right), \mathbf{R}_m\right] = 0,
\tag{4.10}
$$

and

$$
\left[\sum_j \mathbf{A}_j, \mathbf{B}\right] = \sum_j\left[\mathbf{A}_j, \mathbf{B}\right].
\tag{4.11}
$$

The time evolution of a momentum operator, $\mathbf{P}_{Im} = e^{i\mathbf{H}_0 t/\hbar} \mathbf{P}_{Sm} e^{-i\mathbf{H}_0 t/\hbar}$, is

$$
\begin{aligned}
\frac{d}{dt}\mathbf{P}_{Im} &= \frac{i}{\hbar}\left[\mathbf{H}_0^\gamma, \mathbf{P}_{Im}\right] \\
&= \frac{i}{\hbar}\left[\sum_{j=1}^{L}\frac{\mathbf{P}_{Sj}^2}{2\mu_j} + \Phi\left(\overline{\mathbf{R}}_S\right), e^{i\mathbf{H}_0 t/\hbar}\mathbf{P}_{Sm}e^{-i\mathbf{H}_0 t/\hbar}\right] \\
&= \frac{i}{\hbar}e^{i\mathbf{H}_0 t/\hbar}\left[\Phi\left(\overline{\mathbf{R}}_S\right), \mathbf{P}_{Sm}\right]e^{-i\mathbf{H}_0 t/\hbar} \\
&= \frac{i}{\hbar}e^{i\mathbf{H}_0 t/\hbar}\sum_{j=1}^{N}\sum_{n=1}^{M}\phi_{jn}\left[\mathbf{R}_{jS}^n, \mathbf{P}_{Sm}\right]e^{-i\mathbf{H}_0 t/\hbar} \\
&= \frac{i}{\hbar}e^{i\mathbf{H}_0 t/\hbar}\sum_{n=1}^{M}\phi_{mn}\left[\mathbf{R}_{mS}^n, \mathbf{P}_{Sm}\right]e^{-i\mathbf{H}_0 t/\hbar} \\
&= \frac{i}{\hbar}e^{i\mathbf{H}_0 t/\hbar}\sum_{n=1}^{M}\phi_{mn}\left[\mathbf{R}_{mS}^n, \mathbf{P}_{Sm}\right]e^{-i\mathbf{H}_0 t/\hbar} \\
&= \frac{i}{\hbar}e^{i\mathbf{H}_0 t/\hbar}\sum_{n=1}^{M}\phi_{mn}n\left(i\hbar\right)\mathbf{R}_{mS}^{n-1}e^{-i\mathbf{H}_0 t/\hbar} \\
&= -e^{i\mathbf{H}_0 t/\hbar}\nabla\Phi_m\left(\mathbf{R}_{mS}\right)e^{-i\mathbf{H}_0 t/\hbar}.
\end{aligned}
\tag{4.12}
$$

If the constraint $\nabla\Phi_m\left(\mathbf{R}_{mS}\right) = 0$ is imposed, then we have

$$
\frac{d}{dt}\mathbf{P}_{Im} = 0.
\tag{4.13}
$$

Equation (4.13) indicates that each component $\mathbf{P}_{Im}$ of the momentum operator $\mathbf{P}_I$ is constant in time, so that $\mathbf{P}_I(t) = \mathbf{P}_I(0) = \mathbf{P}_S$. Equation (4.8) can thus be integrated directly, to yield

$$
\begin{aligned}
\mathbf{R}_{Im}(t) &= \mathbf{R}_{Im}(0) + \int_0^t \frac{1}{\mu_m}\mathbf{P}_{Im}dt \\
&= \mathbf{R}_{Sm} + \frac{t}{\mu_m}\mathbf{P}_{Sm}.
\end{aligned}
\tag{4.14}
$$

Hence, by induction,

$$
\mathbf{R}_{Im}^n(t) = \left(\mathbf{R}_{Sm} + \frac{t}{\mu_m}\mathbf{P}_{Sm}\right)^n,
\tag{4.15}
$$

for any natural number n, and

$$V\left(\mathbf{R}_{Im}\right) = V\left(\mathbf{R}_{Sm} + \frac{t}{\mu_m}\mathbf{P}_{Sm}\right) \qquad (4.16)$$

for any analytic potential function $V\left(\overline{\mathbf{R}}\right)$.

4.2.2 The "Heisenberg" Hamiltonian and Evolution Operator. Using the reasoning of section 4.2.1, if the coordinate operator is

$$\mathbf{R}_I\left(t\right) = \mathbf{R}_S + \frac{t}{\mu_m}\mathbf{P}_S, \qquad (4.17)$$

then, after two applications of the operator identity

$$e^{\mathbf{A}}\mathbf{B}e^{-\mathbf{A}} = \mathbf{B} + [\mathbf{A},\mathbf{B}] + \frac{1}{2!}[\mathbf{A},[\mathbf{A},\mathbf{B}]] + \frac{1}{3!}[\mathbf{A},[\mathbf{A},[\mathbf{A},\mathbf{B}]]] + \dots, \qquad (4.18)$$

the coordinate operator in the PR-adapted nested interaction picture (Section 3.5.4), is

$$
\begin{aligned}
\mathbf{R}'' &= e^{-i\langle\mathbf{R}_S\rangle\mathbf{P}_S/\hbar}e^{-i\langle\mathbf{P}_S\rangle\mathbf{R}_S/\hbar}\mathbf{R}_Ie^{i\langle\mathbf{P}_S\rangle\mathbf{R}_S/\hbar}e^{i\langle\mathbf{R}_S\rangle\mathbf{P}_S/\hbar} \\
&= e^{-i\langle\mathbf{R}_S\rangle\mathbf{P}_S/\hbar}e^{-i\langle\mathbf{P}_S\rangle\mathbf{R}_S/\hbar}\left(\mathbf{R}_S + \frac{\mathbf{P}_S t}{\mu}\right)e^{i\langle\mathbf{P}_S\rangle\mathbf{R}_S/\hbar}e^{i\langle\mathbf{R}_S\rangle\mathbf{P}_S/\hbar} \\
&= e^{-i\langle\mathbf{R}_S\rangle\mathbf{P}_S/\hbar}\left(\mathbf{R}_S + \frac{\mathbf{P}_S t}{\mu} + \frac{\langle\mathbf{P}\rangle t}{\mu}\right)e^{i\langle\mathbf{R}_S\rangle\mathbf{P}_S/\hbar} \\
&= \mathbf{R}_S + \frac{\mathbf{P}_S t}{\mu} + \frac{\langle\mathbf{P}\rangle t}{\mu} + \langle\mathbf{R}\rangle. \qquad (4.19)
\end{aligned}
$$

Therefore, the PR-adapted Hamiltonian for a one-dimensional analytic potential is

$$
\begin{aligned}
\mathbf{H}'' &= e^{-i\langle\mathbf{R}\rangle\mathbf{P}_S/\hbar}e_I^{-i\langle\mathbf{P}\rangle\mathbf{R}_S/\hbar}\,\mathbf{H}_Ie^{i\langle\mathbf{P}\rangle\mathbf{R}_S/\hbar}e^{i\langle\mathbf{R}\rangle\mathbf{P}_S/\hbar} \\
&= H_1\left(\mathbf{R}_S + \frac{\mathbf{P}_S t}{\mu} + \langle\mathbf{R}\rangle + \frac{\langle\mathbf{P}\rangle t}{\mu}\right). \qquad (4.20)
\end{aligned}
$$

The time-evolution operator is now approximated using the iterated Lanczos method. Krylov basis vectors are built according to equation (3.6), by repeated operation of the Hamiltonian $\mathbf{H}''$ on the wavepacket $\psi\left(t\right)$. The computational savings of the "Heisenberg"

approach compared to a sequential approach vary depending on the chosen partition of $\mathbf{H}$ into $\mathbf{H}_0$ and $\mathbf{H}_1$.

4.2.3 A Reformulated "Heisenberg" Hamiltonian. The manipulations of Section 4.2.1 can lead to simpler formulation of the evolution and Møller operators in certain cases. In constructing a particular interaction picture, the choice of the operator $\mathbf{H}_0^\gamma$ is free. However, that choice immediately determines the remaining portion of the Hamiltonian to be

$$
\begin{aligned}
\mathbf{H}_1^\gamma &= \mathbf{H}^\gamma - \mathbf{H}_0^\gamma \\
&= \sum_{j=L+1}^{N} \frac{\mathbf{P}_{Sj}^2}{2\mu_j} + V\left(\overline{\mathbf{R}}_S\right) - \Phi\left(\overline{\mathbf{R}}_S\right) \\
&= \sum_{j=L+1}^{N} \frac{\mathbf{P}_{Sj}^2}{2\mu_j} + V'\left(\overline{\mathbf{R}}_S\right) .
\end{aligned}
\tag{4.21}
$$

The full interaction-picture Hamiltonian is then written,

$$
\begin{aligned}
\mathbf{H}_I^\gamma &= e^{i\mathbf{H}_0 t/\hbar} \mathbf{H}_1^\gamma e^{-i\mathbf{H}_0 t/\hbar} \\
&= e^{i\mathbf{H}_0 t/\hbar} \left(\sum_{j=L+1}^{N} \frac{\mathbf{P}_{Sj}^2}{2\mu_j} + V'\left(\overline{\mathbf{R}}_S\right) \right) e^{-i\mathbf{H}_0 t/\hbar} \\
&= e^{i\mathbf{H}_0 t/\hbar} \left(\sum_{j=L+1}^{N} \frac{\mathbf{P}_{Sj}^2}{2\mu_j} \right) e^{-i\mathbf{H}_0 t/\hbar} + e^{i\mathbf{H}_0 t/\hbar} V'\left(\overline{\mathbf{R}}_S\right) e^{-i\mathbf{H}_0 t/\hbar} \\
&= \sum_{j=L+1}^{N} \frac{1}{2\mu_j} e^{i\mathbf{H}_0 t/\hbar} \mathbf{P}_{Sj}^2 e^{-i\mathbf{H}_0 t/\hbar} + V'\left(\overline{\mathbf{R}}_I\right) \\
&= \sum_{j=L+1}^{N} \frac{1}{2\mu_j} e^{i\mathbf{H}_0 t/\hbar} \mathbf{P}_{Sj} e^{-i\mathbf{H}_0 t/\hbar} e^{i\mathbf{H}_0 t/\hbar} \mathbf{P}_{Sj} e^{-i\mathbf{H}_0 t/\hbar} + \sum_{m=1}^{M} V'_m \left(\mathbf{R}_{Sm} + \frac{t}{\mu_m} \mathbf{P}_{Sm} \right) \\
&= \sum_{j=L+1}^{N} \frac{1}{2\mu_j} \mathbf{P}_{Ij}^2 + \sum_{m=1}^{M} V'_m \left(\mathbf{R}_{Sm} + \frac{t}{\mu_m} \mathbf{P}_{Sm} \right) \\
&= \sum_{j=L+1}^{N} \frac{1}{2\mu_j} \mathbf{P}_{Sj}^2 + \sum_{m=1}^{M} V'_m \left(\mathbf{R}_{Sm} + \frac{t}{\mu_m} \mathbf{P}_{Sm} \right) .
\end{aligned}
\tag{4.22}
$$

The first term of the expansion of the time-evolution operator is therefore

$$
\begin{aligned}
\mathbf{U}_1^\gamma (t, t_0) &= \exp\left\{\frac{-i}{h} \int_{t_0}^{t} \mathbf{H}_I^\gamma (t') \, dt'\right\} \\
&\approx e^{-i\mathbf{H}_I^\gamma (t_0)(t-t_0)/h} \\
&= \exp\left\{\frac{-i\Delta t}{h}\left[\sum_{j=L+1}^{N} \frac{1}{2\mu_j}\mathbf{P}_{Sj}^2 + \sum_{m=1}^{M} V_m'\left(\mathbf{R}_{Sm}(t_0) + \frac{t_0}{\mu_m}\mathbf{P}_{Sm}\right)\right]\right\}.
\end{aligned}
\tag{4.23}
$$

This form of the operator is amenable to split-operator propagation for those potentials V' for which an analytic expression is available. Exponential potentials such as Morse oscillators are particularly tractable using this approach. Let us now examine the results of certain choices of interaction picture.

4.2.4 Examples of "Heisenberg" Interaction Pictures.

4.2.4.1 The One-Dimensional Case.   In one dimension, the Hamiltonian is given by

$$
\mathbf{H} = \frac{\hbar^2 \mathbf{k}^2}{2m} + \mathbf{V}(r).
\tag{4.24}
$$

Let

$$
\mathbf{H}_0 = \mathbf{H}_a = \frac{\hbar^2 \mathbf{k}^2}{2m},
\tag{4.25}
$$

$$
\mathbf{H}_1 = \mathbf{V}(r).
\tag{4.26}
$$

The Møller operators are time-evolution operators, as shown in Section 3.5.2. For small time intervals, the time-evolution operator is approximated by

$$
\begin{aligned}
\mathbf{U}_1^\gamma (t, t_0) &= \exp\left\{\frac{-i}{h} \int_{t_0}^{t} \mathbf{H}_I (t') \, dt'\right\} \\
&\approx \exp\left\{\frac{-i\Delta t}{h} V\left(\mathbf{r}_S + \frac{\hbar [t_0 + (t - t_0)/2]}{m}\mathbf{k}_S\right)\right\}.
\end{aligned}
\tag{4.27}
$$

This form is fast and simple to apply directly, but again requires an analytic expression for the potential $V(x)$.

4.2.4.2 Two-Dimensional Cases.

Suppose we have a two-dimensional Hamiltonian in Jacobi coordinates,

$$\mathbf{H}_\gamma = \frac{\hbar^2 \mathbf{k}_{r_\gamma}^2}{2m_\gamma} + \frac{\hbar^2 \mathbf{k}_{R_\gamma}^2}{2\mu_\gamma} + \mathbf{V}_\gamma(r_\gamma, R_\gamma). \tag{4.28}$$

As mentioned earlier, a number of different partitions of the Hamiltonian into the portions $\mathbf{H}_0^\gamma$ and $\mathbf{H}_1^\gamma$ are available in systems with two or more degrees of freedom.

- Consider the choice,

$$\mathbf{H}_0^\gamma = \mathbf{T}_\gamma = \frac{\hbar^2 \mathbf{k}_{r_\gamma}^2}{2m_\gamma} \tag{4.29}$$

$$\mathbf{H}_1^\gamma = \frac{\hbar^2 \mathbf{k}_{R_\gamma}^2}{2\mu_\gamma} + \mathbf{V}_\gamma(r_\gamma, R_\gamma). \tag{4.30}$$

In this interaction picture, the Møller operators are phase-shifted time evolutions. The short-time evolution operator is

$$\begin{aligned}
\mathbf{U}_I^\gamma(t, t_0) &= \exp\left\{\frac{-i}{h} \int_{t_0}^t \mathbf{H}_I^\gamma(t')\, dt'\right\} \\
&\approx \exp\left\{\frac{-i\Delta t}{h}\left[\frac{\hbar^2}{2\mu_\gamma}\mathbf{k}_{R_\gamma}^2 + V_\gamma\left(\mathbf{r}_\gamma + \theta\mathbf{k}_{r_\gamma}, \mathbf{R}_\gamma + \theta\mathbf{k}_{R_\gamma}\right)\right]\right\}, \tag{4.31}
\end{aligned}$$

where

$$\theta = \frac{\hbar\left[t_0 + (t - t_0)/2\right]}{\mu_m}. \tag{4.32}$$

This evolution operator can be applied in split-operator fashion, provided always that the interaction potential is available in analytic form.

- Suppose instead we choose,

$$\mathbf{H}_0^\gamma = \mathbf{T} = \frac{\hbar^2 \mathbf{k}_{r_\gamma}^2}{2m_\gamma} + \frac{\hbar^2 \mathbf{k}_{R_\gamma}^2}{2\mu_\gamma} \tag{4.33}$$

$$\mathbf{H}_1^\gamma = \mathbf{V}_\gamma(r_\gamma, R_\gamma). \tag{4.34}$$

In this interaction picture, the short-time evolution operator is approximately

$$\begin{aligned} \mathbf{U}_I^\gamma(t,t_0) &= \exp\left\{ \frac{-i}{h} \int_{t_0}^t \mathbf{H}_I^\gamma(t')\,dt' \right\} \\ &\approx \exp\left\{ \frac{-i\Delta t}{h} V_\gamma\left(\mathbf{r}_\gamma S + \theta \mathbf{k}_{r_\gamma} S, \mathbf{R}_\gamma S + \theta \mathbf{k}_{R_\gamma} S\right) \right\}, \end{aligned} \tag{4.35}$$

(where θ is given once again by equation 4.32) which can be applied directly in the coordinate representation, given an analytic form of the potential.

The Møller state, given by

$$
\begin{aligned}
|\psi_+\rangle_I &= |\psi_+\rangle_S \\
&= \Omega_{+S} |\psi_{in}\rangle_S \\
&= \lim_{t \to -\infty} \mathbf{U}_\gamma^\dagger(t) \, \mathbf{U}_a(t) \, |\psi_{in}\rangle_S \\
&= \lim_{t \to \infty} \mathbf{U}_\gamma(t) \, \mathbf{U}_a^\dagger(t) \, |\psi_{in}\rangle_I \\
&= \lim_{t \to \infty} e^{-i\mathbf{H}_\gamma t/\hbar} e^{i\mathbf{H}_a^\gamma t/\hbar} |\psi_{in}\rangle_I \\
&= \lim_{t \to \infty} e^{-i(\mathbf{H}_0^\gamma + \mathbf{H}_1^\gamma)t/\hbar} e^{i(\mathbf{H}_0^\gamma + \mathbf{V}_{int})t/\hbar} |\psi_{in}\rangle_I \\
&\approx \lim_{t \to \infty} e^{-i\mathbf{H}_0^\gamma t/2\hbar} e^{-i2\mathbf{H}_1^\gamma t/2\hbar} e^{-i\mathbf{H}_0^\gamma t/2\hbar} e^{i\mathbf{H}_0^\gamma t/2\hbar} e^{i2\mathbf{V}_{int}^\gamma t/2\hbar} e^{i\mathbf{H}_0^\gamma t/2\hbar} |\psi_{in}\rangle_I \\
&= \lim_{t \to \infty} e^{-i2\mathbf{H}_I^\gamma \left(\frac{t}{2}\right)t/2\hbar} e^{i2\mathbf{V}_{int_I}^\gamma \left(\frac{t}{2}\right)t/2\hbar} |\psi_{in}\rangle_I \\
&= \lim_{t \to \infty} e^{-i2\mathbf{H}_I^\gamma(t)t/\hbar} e^{i2\mathbf{V}_{int_I}^\gamma(t)t/\hbar} |\psi_{in}\rangle_I \\
&\approx \prod_{n=1}^{\tau/\Delta t} e^{-i2\mathbf{H}_I^\gamma(t_n)\Delta t/\hbar} \prod_{m=1}^{\tau/\Delta t} e^{i2\mathbf{V}_{int_I}^\gamma(t_m)\Delta t/\hbar} |\psi_{in}\rangle_I \\
&= \prod_{n=1}^{\tau/\Delta t} \exp\left\{ \frac{-i2\Delta t}{h} V_\gamma \left(\mathbf{r}_S + \frac{\hbar t_n}{m} \mathbf{k}_S \right) \right\} \\
&\quad \times \prod_{m=1}^{\tau/\Delta t} \exp\left\{ \frac{i2\Delta t}{h} V_{int}^\gamma \left(\mathbf{R}_{\gamma S} + \frac{\hbar t_m}{2\mu_m} \mathbf{k}_{R_\gamma S} \right) \right\} |\psi_{in}\rangle_I,
\end{aligned}
\tag{4.36}
$$

(employing the Zassenhaus identity (3.2) involves two propagations in this case, since $\mathbf{H}_0 \neq \mathbf{H}_a$. The final line of equation (4.36) is only of use for analytic forms of the potentials V_γ and V_{int}^γ. It should also be noted that the allowable size of the time step Δt is halved in this case because the Hamiltonian is doubled in the propagation operator.

- A final interesting partition, choosing $\mathbf{H}_0$ as the full Hamiltonian, results in a true Heisenberg picture. In this special case of the interaction picture, state vectors are time independent:

$$
\begin{aligned}
|\psi\rangle_H &= e^{i\mathbf{H}t/\hbar} |\psi(t)\rangle_S \\
&= e^{i\mathbf{H}t/\hbar} e^{-i\mathbf{H}t/\hbar} |\psi(0)\rangle_S \\
&= |\psi(0)\rangle_S.
\end{aligned}
\tag{4.37}
$$

Therefore, time-dependent propagation methods do not apply in the way discussed thus far. Instead, operators must be evaluated directly as functions of time,

$$\mathbf{O}_H\left(t\right) = e^{i\mathbf{H}t/\hbar}\mathbf{O}_S e^{-i\mathbf{H}t/\hbar}. \tag{4.38}$$

The Møller operators are only defined at $t = 0$, so they are the same as in the Schrödinger picture,

$$
\begin{aligned}
\left|\psi_\pm\right\rangle_H &= \left|\psi_\pm\right\rangle_S = \Omega_{\pm S}\left|\psi_{in(out)}\right\rangle_S \\
&= \lim_{t\to\mp\infty} e^{i\mathbf{H}_\gamma t/\hbar}e^{-i\mathbf{H}_a^\gamma t/\hbar}\left|\psi_{in(out)}\right\rangle_S \\
&= \lim_{t\to\pm\infty} e^{-i\mathbf{H}_\gamma t/\hbar}e^{i\mathbf{H}_a^\gamma t/\hbar}\left|\psi_{in(out)}\right\rangle_H \\
&\approx e^{-i\mathbf{H}_\gamma \tau/\hbar}e^{i\mathbf{H}_a^\gamma \tau/\hbar}\left|\psi_{in(out)}\right\rangle_H.
\end{aligned}
\tag{4.39}
$$

The problem of computing Møller states is thus formally identical in the Schrödinger and Heisenberg pictures. The Møller operator could be decomposed into its two evolution-operator components, and each operation performed in the Heisenberg picture using a variant of the Lanczos technique, but this approach has no apparent advantage over a judiciously chosen interaction-picture propagation.

4.2.5 Computational Problems of the "Heisenberg" Approach. First- and second-order Lanczos propagators were developed to demonstrate the "Heisenberg" interaction picture. The results were good for the exponential potential functions $V\left(x\right) = De^{-ax}$ already demonstrated by Tannor's group(49), but not at all reliable for realistic interaction potentials. The problem may lie in the fact that the effect of the potential is evaluated entirely in the Krylov subspace, using only a few sampling points instead of the many used when the potential is sampled at each grid point in coordinate or momentum space. In a one-dimensional PR-adapted nested "Heisenberg" interaction picture, for example, the Hamiltonian is evaluated as

$$\mathbf{H}'' = \mathbf{V}\left(\mathbf{x} + \frac{\hbar\mathbf{k}t}{\mu} + \left\langle\mathbf{x}\right\rangle + \frac{\hbar\left\langle\mathbf{k}\right\rangle t}{\mu}\right), \tag{4.40}$$

where the argument $\mathbf{y}(t) = \mathbf{x} + \frac{\hbar \mathbf{k} t}{\mu} + \langle \mathbf{x} \rangle + \frac{\hbar \langle \mathbf{k} \rangle t}{\mu}$ is diagonalized, leading to the potential being evaluated at the Ritz values $y_i(t) = \langle q_i | \mathbf{y}(t) | q_i \rangle$ Figure 4.4 shows the dispersion of
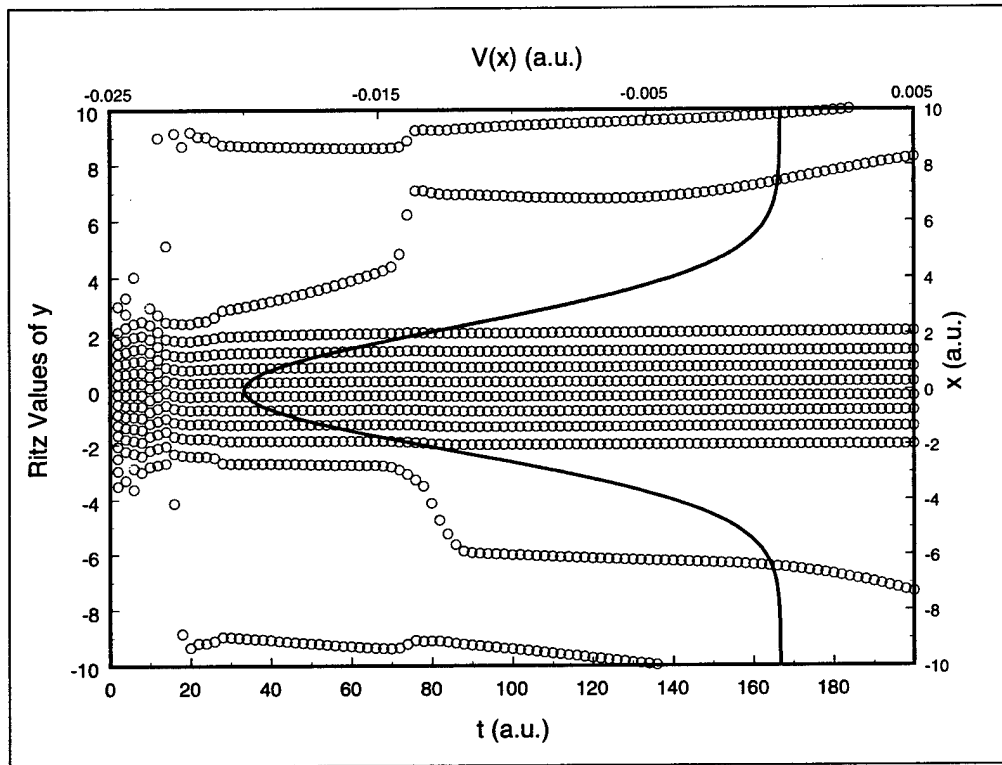
Figure 4.4   The coordinate representation of the first seventeen Ritz values of a Gaussian wavepacket propagated in the "Heisenberg" interaction picture using a twenty-vector Krylov basis, with a Gaussian well potential. The progression of the Ritz values over time is represented with open circles. The Hamiltonian is evaluated as the value of the potential $V(y)$, represented by the solid curve, where only the Ritz values of y are used instead of the relatively much more densely distributed coordinate values x.

the Ritz values for a localized scattering potential as propagation time progresses. Since the Hamiltonian is approximated by evaluating the potential function at the Ritz values, the Ritz values are plotted in conjunction with $V(x)$. As time progresses, some Ritz values follow the dispersing wavepacket, while some remain in the region where the potential is significant. This opens the computation to loss of accuracy as the resulting basis may come to bear less and less of a relationship to either the Hamiltonian or the wavefunction.

This is a speculative explanation for the observed unreliability of the technique. Of several analytic potentials examined using this technique, only an exponential potential yielded accurate propagated wavepackets using the "Heisenberg" technique.

4.3 The Finite-Basis Approach

The third approach tried and abandoned was named the finite-basis approach. It had the advantage of speed, based on the virtual elimination of the requirement to perform FFTs by performing the entire computation in a Krylov subspace based on either the coordinate or momentum representation of the wavefunction, rather than both. However, this approach could not be made computationally stable.

4.3.1 Derivation.

In the iterative Lanczos method(44), the evolution operator $U_I(t)$ is expressed in a finite basis of dimension $M \ll N$, where N is the grid size(49–51). In matrix notation,

$$
\begin{bmatrix}
\langle x_1 | \psi(t + \Delta t) \rangle \\
\vdots \\
\vdots \\
\langle x_N | \psi(t + \Delta t) \rangle
\end{bmatrix}
=
\begin{bmatrix}
\langle x_1 | q_1 \rangle & \cdots & \langle x_1 | q_M \rangle \\
\vdots & \cdots & \vdots \\
\vdots & \cdots & \vdots \\
\langle x_N | q_1 \rangle & \cdots & \langle x_N | q_M \rangle
\end{bmatrix}
\tag{4.41}
$$

$$
\times
\begin{bmatrix}
\langle q_1 | U(t + \Delta t, t) | q_1 \rangle & \cdots & \langle q_1 | U(t + \Delta t, t) | q_M \rangle \\
\vdots & \cdots & \vdots \\
\langle q_M | U(t + \Delta t, t) | q_1 \rangle & \cdots & \langle q_M | U(t + \Delta t, t) | q_M \rangle
\end{bmatrix}
$$

$$
\times
\begin{bmatrix}
\langle q_1 | x_1 \rangle & \cdots & \cdots & \langle q_1 | x_N \rangle \\
\vdots & \cdots & \cdots & \vdots \\
\langle q_M | x_1 \rangle & \cdots & \cdots & \langle q_M | x_N \rangle
\end{bmatrix}
\begin{bmatrix}
\langle x_1 | \psi(t) \rangle \\
\vdots \\
\vdots \\
\langle x_N | \psi(t) \rangle
\end{bmatrix}.
$$

The M basis vectors, $|q_n\rangle$, in the Lanczos method, are derived from orthonormalized Krylov vectors

$$|\phi_n\rangle = \mathbf{H}_I^n |\psi(t)\rangle = \mathbf{U}_0^\dagger(t)\,\mathbf{V}^n\mathbf{U}_0(t)\,|\psi(t)\rangle. \qquad (4.42)$$

This expression, if computed directly as in the sequential method, involves two free-particle type propagations over the full time t, not just the incremental time Δt: first by $\mathbf{U}_0(t)$ and then by $\mathbf{U}_0^\dagger(t)$. This double propagation must be done M times for each time step in order to obtain all of the Krylov vectors. Furthermore, the same grid size is required as in the Schrödinger picture, since the full spreading effect of $\mathbf{U}_0(t)$ is ultimately incurred before being reversed by $\mathbf{U}_0^\dagger(t)$. This direct approach for computing the Krylov vectors must therefore be avoided, if propagation in the interaction picture is to have any advantage over the Schrödinger picture.

The need to propagate for the full time t and back again can be finessed by performing the propagations using $\mathbf{U}_0(\pm\Delta t)$ instead of $\mathbf{U}_0(\pm t)$. The interaction Hamiltonian at any time $t_j = t_{j-1} + \Delta t$ is related to the previous time's Hamiltonian as

$$
\begin{aligned}
\mathbf{H}_I(t_j) &= \mathbf{U}_0^\dagger(t_j)\,\mathbf{V}\mathbf{U}_0(t_j) \\
&= e^{i\mathbf{H}_0(t_{j-1}+\Delta t)/\hbar}\mathbf{V}e^{-i\mathbf{H}_0(t_{j-1}+\Delta t)/\hbar} \\
&= e^{i\mathbf{H}_0\Delta t/\hbar}\left(e^{i\mathbf{H}_0 t_{j-1}/\hbar}\mathbf{V}e^{-i\mathbf{H}_0 t_{j-1}/\hbar}\right)e^{-i\mathbf{H}_0\Delta t/\hbar} \\
&= e^{i\mathbf{H}_0\Delta t/\hbar}\mathbf{H}_I(t_{j-1})\,e^{-i\mathbf{H}_0\Delta t/\hbar}.
\end{aligned}
\qquad (4.43)
$$

The previous Hamiltonian, $\mathbf{H}_I(t_{j-1})$, has already been diagonalized in its own finite basis, and may be transformed to the full momentum representation by means of a non-square matrix $\mathbf{Q}$, whose elements $\mathbf{Q}_{nm} = \left\langle k_n \middle| q_m^{j-1} \right\rangle$ are computed as part of the Lanczos tri-diagonalization process. This enables $\mathbf{H}_I(t_j)$ to be represented in turn in an M-dimensional subspace, and then applied to a wavepacket in the momentum representation.

For each time step t_j, the first Krylov vector is chosen to be

$$\left| q_1^j \right\rangle = |\psi(t_{j-1})\rangle, \qquad (4.44)$$

4-18

and is computed in its momentum representation, $\left\langle k \middle| q_1^j \right\rangle$. To obtain each subsequent basis vector, $\left| q_n^j \right\rangle$, it is necessary to calculate the vector

$$\begin{aligned}
\left| \phi_{n-1}^j \right\rangle &= \mathbf{H}_I\left(t_j\right) \left| \phi_{n-1}^j \right\rangle \\
&= e^{i\mathbf{H}_0 \Delta t/\hbar} \mathbf{H}_I\left(t_{j-1}\right) e^{-i\mathbf{H}_0 \Delta t/\hbar} \left| \phi_{n-1}^j \right\rangle.
\end{aligned} \tag{4.45}$$

In the momentum representation,

$$\begin{aligned}
\left\langle k \middle| \phi_{n-1}^j \right\rangle &= \left\langle k \middle| e^{i\mathbf{H}_0 \Delta t/\hbar} \mathbf{H}_I\left(t_{j-1}\right) e^{-i\mathbf{H}_0 \Delta t/\hbar} \middle| \phi_{n-1}^j \right\rangle \\
&= \int dk' \left\langle k \middle| e^{i\mathbf{H}_0 \Delta t/\hbar} \middle| k' \right\rangle \sum_{n'=1}^{M} \left\langle k' \middle| q_{n'}^{j-1} \right\rangle \sum_{n''=1}^{M} \left\langle q_{n'}^{j-1} \middle| \mathbf{H}_I\left(t_{j-1}\right) \middle| \phi_{n''}^{j-1} \right\rangle \\
&\quad \times \int dk'' \left\langle q_{n''}^{j-1} \middle| k'' \right\rangle \int dk''' \left\langle k'' \middle| e^{-i\mathbf{H}_0 \Delta t/\hbar} \middle| k''' \right\rangle \left\langle k''' \middle| \phi_{n-1}^j \right\rangle. \tag{4.46}
\end{aligned}$$

The linearly independent Krylov basis vectors $\left| \phi_n^j \right\rangle$ are orthonormalized to obtain the basis vectors $\left| q_n^j \right\rangle$. Thus, the basis vectors are calculated using propagations over just the durations $\pm \Delta t$, enabling a reduction in grid size and eliminating FFTs entirely from the propagation process.

Further examination of the process for calculating subsequent basis vectors reveals another benefit of pairing the interaction picture with the Lanczos propagation method. The vector $\left| q_n^j \right\rangle$ is generated according to equation (3.9),

$$\begin{aligned}
\left| q_n^j \right\rangle &= \frac{1}{\beta_n} \left\{ \mathbf{H}_I\left(t_j\right) \left| q_{n-1}^j \right\rangle - \alpha_{n-1} \left| q_{n-1}^j \right\rangle - \beta_{n-1} \left| q_{n-2}^j \right\rangle \right\} \\
&= \frac{1}{\beta_n} \left\{ \frac{1}{\beta_{n-1}} \mathbf{H}_I\left(t_j\right) \left[\mathbf{H}_I\left(t_j\right) \left| q_{n-2}^j \right\rangle - \alpha_{n-2} \left| q_{n-2}^j \right\rangle - \beta_{n-2} \left| q_{n-3}^j \right\rangle \right] \right. \\
&\quad \left. - \alpha_{n-1} \left| q_{n-1}^j \right\rangle - \beta_{n-1} \left| q_{n-2}^j \right\rangle \right\} \tag{4.47} \\
&= \frac{1}{\beta_n \beta_{n-1}} \left[\mathbf{H}_I\left(t_j\right) \mathbf{H}_I\left(t_j\right) \left| q_{n-2}^j \right\rangle - \alpha_{n-2} \mathbf{H}_I\left(t_j\right) \left| q_{n-2}^j \right\rangle - \beta_{n-2} \mathbf{H}_I\left(t_j\right) \left| q_{n-3}^j \right\rangle \right] \\
&\quad - \frac{\alpha_{n-1}}{\beta_n} \left| q_{n-1}^j \right\rangle - \frac{\beta_{n-1}}{\beta_n} \left| q_{n-2}^j \right\rangle.
\end{aligned}$$

The vectors $\left|p_m^j\right\rangle$, for $1 < m < M$, are given by

$$
\begin{aligned}
\left|p_m^j\right\rangle &= \mathbf{H}_I\left(t_j\right)\left|q_m^j\right\rangle \\
&= \mathbf{H}_I\left(t_j\right)\frac{1}{\beta_m}\left\{\mathbf{H}_I\left(t_j\right)\left|q_{m-1}^j\right\rangle - \alpha_{m-1}\left|q_{m-1}^j\right\rangle - \beta_{m-1}\left|q_{m-2}^j\right\rangle\right\} \\
&= \frac{1}{\beta_m}\left\{\mathbf{H}_I\left(t_j\right)\left|p_m^j\right\rangle - \alpha_{m-1}\left|p_{m-1}^j\right\rangle - \beta_{m-1}\left|p_{m-2}^j\right\rangle\right\}. \qquad (4.48)
\end{aligned}
$$

Then for $1 < n \leq M$, equation (4.47) becomes

$$
\begin{aligned}
\left|q_n^j\right\rangle &= \frac{1}{\beta_n\beta_{n-1}}\left[\mathbf{H}_I\left(t_j\right)\left|p_{n-2}^j\right\rangle - \alpha_{n-2}\left|p_{n-2}^j\right\rangle - \beta_{n-2}\left|p_{n-3}^j\right\rangle\right] \\
&\qquad -\frac{\alpha_{n-1}}{\beta_n}\left|q_{n-1}^j\right\rangle - \frac{\beta_{n-1}}{\beta_n}\left|q_{n-2}^j\right\rangle \\
&= \frac{1}{\beta_n}\left\{\left|p_{n-1}^j\right\rangle - \alpha_{n-1}\left|q_{n-1}\left(t_j\right)\right\rangle_I - \beta_{n-1}\left|q_{n-2}\left(t_j\right)\right\rangle_I\right\}, \qquad (4.49)
\end{aligned}
$$

where the values of $\left|p_{n-2}^j\right\rangle$ and $\left|p_{n-3}^j\right\rangle$ are known from previous calculations. Only one new vector, $\mathbf{H}_I\left(t_j\right)\left|p_{n-2}^j\right\rangle$, is computed for the first time. The sum

$$
\left|p_{n-1}^j\right\rangle = \frac{1}{\beta_{n-1}}\left\{\mathbf{H}_I\left(t_j\right)\left|p_{n-2}^j\right\rangle - \alpha_{n-2}\left|p_{n-2}^j\right\rangle - \beta_{n-2}\left|p_{n-3}^j\right\rangle\right\} \qquad (4.50)
$$

is saved for future use.

It is now clear that the operation of the Hamiltonian is going to be evaluated only in expressions of the form of the first term of equation (4.50). Such vectors can be evaluated as outlined above, by recourse to the previously diagonalized operator $\mathbf{H}_I\left(t_{j-1}\right)$:

$$
\begin{aligned}
\mathbf{H}_I\left(t_j\right)\left|p_{n-2}^j\right\rangle &= \frac{1}{\beta_{n-2}}\left\{\mathbf{H}_I\left(t_j\right)\mathbf{H}_I\left(t_j\right)\left|p_{n-3}^j\right\rangle - \alpha_{n-3}\mathbf{H}_I\left(t_j\right)\left|p_{n-3}^j\right\rangle\right. \\
&\qquad\left. - \beta_{n-3}\mathbf{H}_I\left(t_j\right)\left|p_{n-4}^j\right\rangle\right\} \\
&= \frac{1}{\beta_{n-2}}\left\{e^{i\mathbf{H}_0\Delta t/\hbar}\mathbf{H}_I\left(t_{j-1}\right)e^{-i\mathbf{H}_0\Delta t/\hbar}e^{i\mathbf{H}_0\Delta t/\hbar}\mathbf{H}_I\left(t_{j-1}\right)e^{-i\mathbf{H}_0\Delta t/\hbar}\left|p_{n-3}^j\right\rangle\right. \\
&\qquad - \alpha_{n-3}e^{i\mathbf{H}_0\Delta t/\hbar}\mathbf{H}_I\left(t_{j-1}\right)e^{-i\mathbf{H}_0\Delta t/\hbar}\left|p_{n-3}^j\right\rangle \\
&\qquad\left. - \beta_{n-3}e^{i\mathbf{H}_0\Delta t/\hbar}\mathbf{H}_I\left(t_{j-1}\right)e^{-i\mathbf{H}_0\Delta t/\hbar}\left|p_{n-4}^j\right\rangle\right\} \qquad (4.51) \\
&= \frac{1}{\beta_n}e^{i\mathbf{H}_0\Delta t/\hbar}\left\{\mathbf{H}_I\left(t_{j-1}\right)\left|s_{n-3}^j\right\rangle - \alpha_{n-3}\left|s_{n-3}^j\right\rangle - \beta_{n-3}\left|s_{n-4}^j\right\rangle\right\}.
\end{aligned}
$$

The terms $\left|s_m^j\right\rangle$ in equation (4.51) represent the vectors

$$\left|s_0^j\right\rangle = e^{-i\mathbf{H}_0\Delta t/\hbar}\left|q_1^j\right\rangle_I, \tag{4.52}$$

and for $1 < m \le M$,

$$\left|s_m^j\right\rangle = \mathbf{H}_I\left(t_{j-1}\right)e^{-i\mathbf{H}_0\Delta t/\hbar}\left|p_m^j\right\rangle, \tag{4.53}$$

which turn out to be a more convenient form in which to store the information contained in the vectors $\left|p_m^j\right\rangle$, taking advantage of the cancellation of evolution operators which occurs in repeated operations of $\mathbf{H}_I\left(t_{j-1}\right)$. The operations contained in the braces in equation (4.51) are all performed in the Krylov subspace of the time $t = t_{j-1}$, and the result transformed to the momentum representation and propagated by $-\Delta t$. The propagated vector is then added to the remaining terms of equations (4.49) and (4.50) in momentum space. Only $M + 1$ FFTs are required over the entire propagation to compute the first M basis vectors if $\mathbf{H}_0$ and $\mathbf{H}_1$ are respectively functions of position and momentum alone, as opposed to $2M$ FFTs *per time step* required by the Lanczos method in the Schrödinger picture.

4.3.2 Implementation Problems and Possible Solutions. The finite-basis algorithm was implemented in a one-dimensional propagator, using a first-order truncation of the time-evolution operator and no re-orthogonalization of the basis vectors. In this crude form, the method falls victim to two idiosyncracies of the iterative Lanczos approach.

First, equation 4.46 implicitly assumes that the $\left|q_n^j\right\rangle$ span the full N-dimensional space. This approximation that $\left|\psi\left(t_{j+1}\right)\right\rangle$ can be expressed as a linear combination of the $\left|q_n^j\right\rangle$ is adequate for a single time step, but its error, compounded over several time steps, is sufficient to cause the pure finite-basis method described above to become unstable for long-time propagations of the type required for reactive scattering calculations. The loss of accuracy begins immediately with the highest-order Krylov basis vectors, so increasing the basis size delays the onset of inaccuracy for the wavefunction itself, but does not prevent it permanently. Once the degradation progresses far enough, too few appropriate basis

4-21

vectors remain to represent the wavefunction accurately. Figure 4.5 shows the onset of degradation in wavefunctions constructed in Krylov bases of various order.
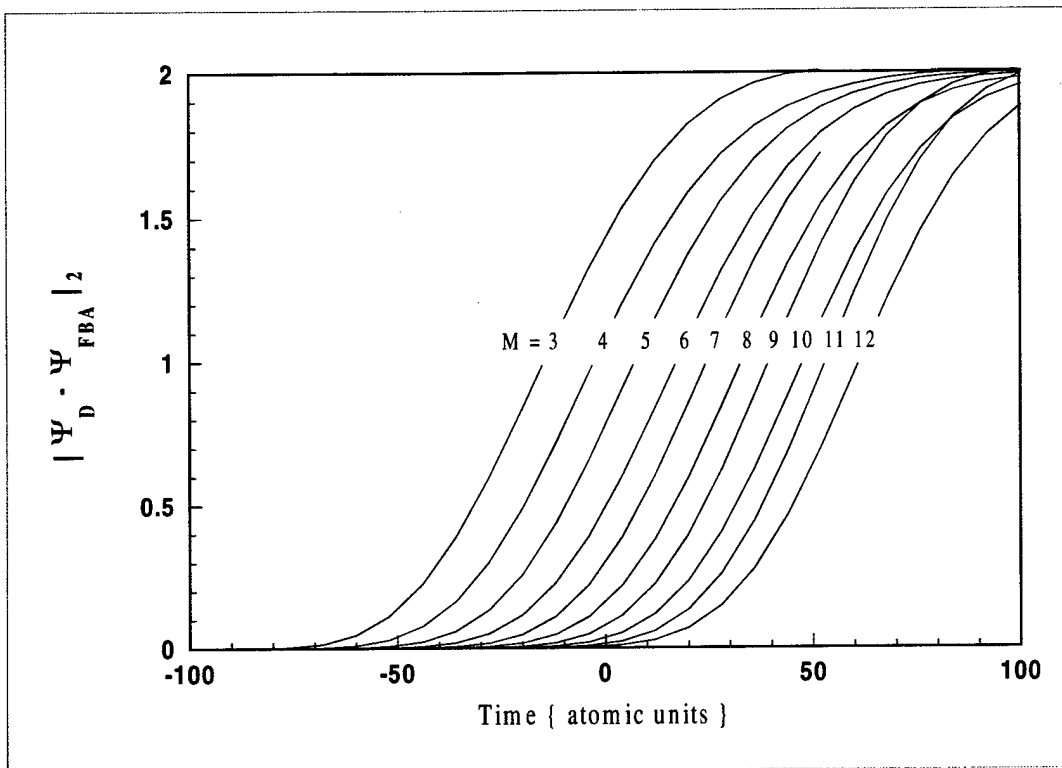
Figure 4.5   Increasing error with propagation time for Gaussian wavepackets on a linear potential, using a first-order finite-basis nested interaction picture propagator with various Krylov basis dimensions M. The reference wavefunction Ψ_D is computed using the sequential non-nested interaction picture described in Section 4.1.

Second, the Lanczos tri-diagonalization algorithm suffers from a tendency for the orthogonality of the basis vectors to degrade with repeated iterations. This results from a well-known numerical problem of Gram-Schmidt orthogonalization, which can be dealt with when necessary by periodically re-orthogonalizing all or some of the basis vectors(72–75).

Three possibilities for stabilizing the finite-basis algorithm were considered:

- Periodic "resetting" of the approximation by performing a direct-propagation step using FFTs on the momentum grid. This lengthens the lifetime of the propagation, but ultimately the propagation still fails catastrophically (Figure 4.6). Degradation

4-22
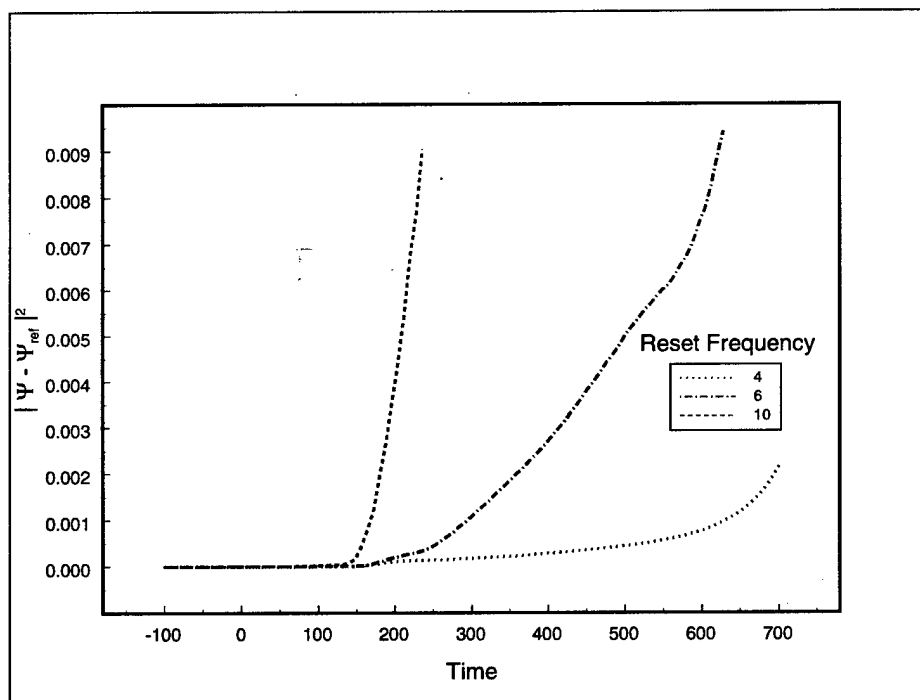
Figure 4.6   Degradation in accuracy of propagated wavepacket with time. Propagations were done on a linear ramp potential, using the finite-basis algorithm, "reset" periodically by performing a time step using the sequential non-nested interaction picture. The reference wavefunction Ψ_{ref} is computed entirely in the sequential non-nested interaction picture.

is not entirely eliminated even when every other time step is performed using the inefficient non-nested sequential method, as reflected in the gradual destruction of the state vector illustrated in Figure 4.7.
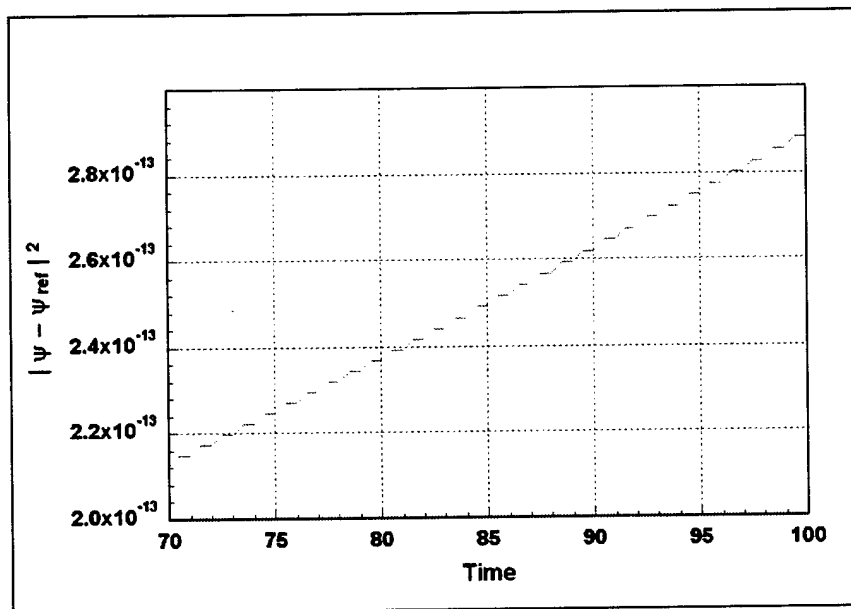
Figure 4.7   Even alternating every other iteration between nested finite-basis and non-nested sequential interaction pictures results in a gradual but continuous degradation in accuracy of the propagated wavepacket as compared to Ψ_{ref}, obtained entirely by using the sequential non-nested propagator.

- Re-orthogonalization of the basis vectors to allow larger, more stable basis sets. This was attempted, and failed to have any effect on the degradation of accuracy in propagated wavepackets.

- Implementation of higher-order Magnus representations of the time evolution operator to improve the accuracy of transitions from one time step's basis to the next, and allow longer propagations with less error. This would only postpone the degradation by allowing longer propagations with the same number of time steps, so second-order Lanczos propagation was never applied to the finite-basis approach.

V. Software Implementation and Validation

5.1 Code Implementation

The core activity of this project, described in Chapter VI, involves computing S-matrix elements by generating Møller states in the interaction picture, then evaluating the Fourier transform of the time-dependent correlation function (2.24), computed in the Schrödinger picture with absorbing boundary conditions. The Møller states are generated using a Lanczos propagator based on the second-order Magnus expansion of the time-evolution operator to propagate product and reactant wavepackets from $t = \pm\tau$ to $t = 0$. The Tannor sequential PR-adapted nested interaction picture, introduced in Section 3.5.4, is used. For comparison, Møller states are also computed in the Schrödinger picture, using the split-operator method of Section 3.1. The Schrödinger spilt-operator method is faster and more commonly used than the Lanczos method in the Schrödinger picture, and thus presents the primary benchmark for comparison of computational effort required to obtain similar results in the interaction picture.

All code for calculating the Møller states is written in C++. Several legacy subroutines in standard C are employed, including Basic Linear Algebra Subprograms (BLAS) and CLAPACK linear-algebra subroutines from Netlib, and a matrix diagonalizer and FFT from *Numerical Recipes in C* (76–79).

The Møller states are passed to a modified version of a Fortran program, developed by R. S. Calfas to generate correlation functions, using split-operator propagation with absorbing boundary conditions in the Schrödinger picture(23,80). S-matrix elements are then derived from the correlation functions using another C++ application. The Delta C++ compiler and Silicon Graphics Fortran compilers were used on MIPS 3000 and higher-performance Silicon Graphics workstations.

5.1.1 Initial Conditions.
The interaction-picture Møller states are computed in the PR-adapted interaction picture(49) defined by

$$H_0 = H_a = T \leftrightarrow \frac{\hbar k^2}{2\mu}. \tag{5.1}$$

The channel-packet method begins with four initial states,

$$\left| \psi_{in/out}^{\lambda/\rho}\left(\pm \tau \right) \right\rangle_I = e^{\mp \mathbf{H}_0 \tau / \hbar} \left| \psi_{in/out}^{\lambda/\rho} \right\rangle_I = \left| \psi_{in/out}^{\lambda/\rho} \right\rangle_S , \tag{5.2}$$

made up of one reactant (*in*) and one product (*out*) state in each of the two channels (to the left (λ) and right (ρ) of the interaction region of the potential. These initial wavepackets are constructed analytically in the Schrödinger picture as Gaussians

$$\left\langle x \left| \psi_{in/out}^{\lambda/\rho} \right\rangle_S = \left[2\pi\sigma^2 \right]^{-\frac{1}{4}} \exp\left[-\frac{(x - x_0)^2}{4\sigma^2} + ik_0 x \right] . \tag{5.3}$$

(the coordinate representation of Equation 2.5) centered near the interaction region at $t = 0$, but are the same as the corresponding interaction-picture states $\left\langle x \left| \psi_{in/out}^{\lambda/\rho}\left(\pm\tau \right) \right\rangle_I$ at time $+\tau$ for products and $-\tau$ for reactants. The corresponding PR-adapted intermediate states,

$$\left| \psi_{in/out}^{\lambda/\rho}\left(\pm\tau \right) \right\rangle_I'' \leftrightarrow e^{ix_0 k} e^{-ik_0 x} \psi_{in/out}^{\lambda/\rho}\left(x, \pm\tau \right)_I , \tag{5.4}$$

are then calculated, using the initial conditions $\langle x \rangle = x_0$ and $\langle k \rangle = k_0$. Subsequently, new values of $\langle x \rangle$ and $\langle k \rangle$ must be computed after each time step and used to update the evolving wavepacket. At $t = t_0$, the end of the channel-packet method's first propagation, the Møller states are converted from the nested interaction picture to the Schrödinger picture, as

$$\left\langle x \left| \psi \pm \right\rangle_S = \left\langle x \left| e^{-i\langle \mathbf{k}\rangle \mathbf{x}} e^{i\langle \mathbf{x}\rangle \mathbf{k}} \right| \psi \pm \right\rangle_I'' . \tag{5.5}$$

5.1.2 Computation of Møller States. The short-time evolution operator is approximated by a second-order Magnus expansion,

$$
\begin{aligned}
U_I\left(t_{k+1}, t_k \right) &\approx \exp\left\{ -\frac{i}{\hbar} \int_{t_k}^{t_{k+1}} \mathbf{H}_I\left(t' \right) dt' - \frac{1}{2\hbar^2} \int_{t_k}^{t_{k+1}} dt' \int_{t_k}^{t_k'} \left[\mathbf{H}_I\left(t' \right), \mathbf{H}_I\left(t'' \right) \right] dt'' \right\} \\
&\approx \exp\left\{ -\frac{i}{\hbar} \mathbf{H}_I\left(t_k + \frac{\Delta t}{2} \right) \Delta t - \frac{1}{12\hbar^2} \left[\mathbf{H}_I\left(t_{k+1} \right), \mathbf{H}_I\left(t_k \right) \right] \left(\Delta t \right)^2 \right\} \tag{5.6}
\end{aligned}
$$

where midpoint quadrature is employed to approximate the first-order term, and trapezoidal integration for the second-order term. The geometry of the derivation of the second-order term,

$$\mathbf{B}\left(t_{k+1}, t_k\right) = \frac{1}{2\hbar^2} \int_{t_k}^{t_{k+1}} dt' \int_{t_k}^{t'} dt'' \left[\mathbf{H}\left(t'\right), \mathbf{H}\left(t''\right)\right], \qquad (5.7)$$

is illustrated in Figure 5.1. Two-dimensional trapezoidal quadrature operates in a super-
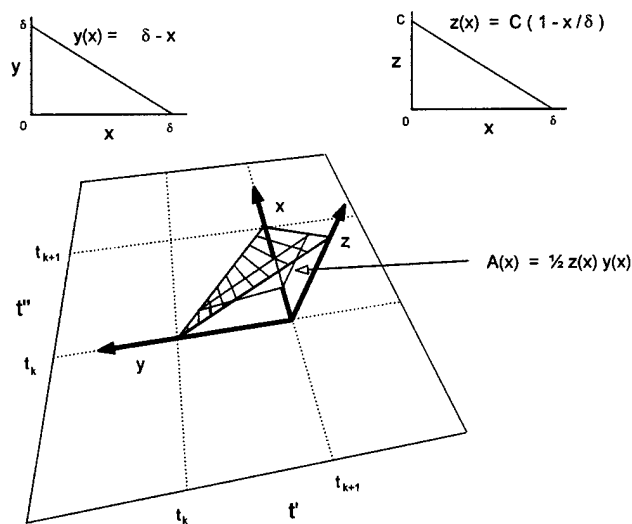
Figure 5.1   Calculation of the two-dimensional trapezoidal integral.

space which adds the time dimensions t' and t'' to the Hilbert space containing the commutator. The hypersurface of integration, $z\left(t', t''\right) = \left[\mathbf{H}\left(t'\right), \mathbf{H}\left(t''\right)\right]$, is approximated by a plane. The integral is the volume between the $\left(t', t''\right)$ plane and the triangle containing the points $\left(t' = t'' = t_k, z = 0\right)$, $\left(t' = t'' = t_{k+1}, z = 0\right)$, and $\left(t' = t_{k+1}, t'' = t_k, z = \left[\mathbf{H}\left(t_{k+1}\right), \mathbf{H}\left(t_k\right)\right] = \mathbf{C}\right)$. The integral is easily performed in the coordinates $x = t'' - t_k, y = t_{k+1} - t'$,

where $\delta = \Delta t = t_k - t_{k-1}$. Thus,

$$
\begin{aligned}
\mathbf{B}\left(t_{k+1}, t_k\right) &\approx \frac{1}{2\hbar^2} \int_0^\delta dx \left\{ \frac{1}{2} z\left(x\right) y\left(x\right) \right\} \\
&= \frac{1}{4\hbar^2} \int_0^\delta dx \left\{ \mathbf{C} \left(1 - \frac{x}{\delta}\right)\left(\delta - x\right) \right\} \\
&= \frac{\mathbf{C}}{4\hbar^2} \int_0^\delta dx \left\{ \delta - 2x + \frac{x^2}{\delta} \right\} \\
&= \frac{\mathbf{C}}{4\hbar^2} \left[\delta x - x^2 + \frac{x^3}{3\delta} \right]_0^\delta \\
&= \frac{\delta^2}{12\hbar^2} \mathbf{C} \\
&= \frac{\left(\Delta t\right)^2}{12\hbar^2} \left[\mathbf{H}\left(t_{k+1}\right), \mathbf{H}\left(t_k\right)\right].
\end{aligned} \tag{5.8}
$$

The result of applying the evolution operator to a PR-adapted wavepacket $\left\langle x \mid \psi^j \right\rangle_I''$ at time $t = t_j$ is

$$
\xi^{j+1}\left(x\right) = \left\langle x \left| e^{i\langle \mathbf{x}\rangle_j \mathbf{k}} e^{-i\langle \mathbf{k}\rangle_j \mathbf{x}} \right| \psi^{j+1} \right\rangle_I'', \tag{5.9}
$$

a representation of the wavepacket at time $t = t_{j+1}$, but in the interaction picture defined by the displacement-boost operator $e^{i\langle \mathbf{x}\rangle_j \mathbf{k}} e^{-i\langle \mathbf{k}\rangle_j \mathbf{x}}$, corresponding to time $t = t_j$. The wavepacket is brought into the correct interaction picture by first updating the expectation values,

$$
\langle \mathbf{x} \rangle_{j+1} = \langle \mathbf{x} \rangle_j + \left\langle \xi^{j+1} \left| \mathbf{x} \right| \xi^{j+1} \right\rangle, \tag{5.10}
$$

and

$$
\langle \mathbf{k} \rangle_{j+1} = \langle \mathbf{k} \rangle_j + \left\langle \xi^{j+1} \left| \mathbf{k} \right| \xi^{j+1} \right\rangle, \tag{5.11}
$$

5-4

then computing,

$$
\begin{aligned}
\langle x | \psi^{j+1} \rangle_I'' &= \left\langle x \left| e^{i\langle \mathbf{x} \rangle_{j+1} \mathbf{k}} e^{-i\langle \mathbf{k} \rangle_{j+1} \mathbf{x}} \right| \psi^{j+1} \right\rangle_I \\
&= e^{i\langle \mathbf{x} \rangle_{j+1} k} e^{-i\langle \mathbf{k} \rangle_{j+1} x} e^{i\langle \mathbf{k} \rangle_j x} e^{-i\langle \mathbf{x} \rangle_j k} \xi^{j+1}(x) \\
&= e^{i\left(\langle \mathbf{x} \rangle_j + \langle \xi | \mathbf{x} | \xi \rangle \right)k} e^{-i\left(\langle \mathbf{k} \rangle_{j+1} - \langle \mathbf{k} \rangle_j \right)x} e^{-i\langle \mathbf{x} \rangle_j k} \xi^{j+1}(x) \\
&= e^{i\langle \xi | \mathbf{x} | \xi \rangle \, k} e^{i\langle \mathbf{x} \rangle_j k} e^{-i\langle \xi | \mathbf{k} | \xi \rangle \, x} e^{-i\langle \mathbf{x} \rangle_j k} \xi^{j+1}(x) \\
&= e^{i\langle \xi | \mathbf{x} | \xi \rangle \, k} e^{-i\langle \xi | \mathbf{k} | \xi \rangle \, x} e^{i\langle \mathbf{x} \rangle_j k} e^{-i\langle \xi | \mathbf{k} | \xi \rangle \, \langle \mathbf{x} \rangle_j} e^{-i\langle \mathbf{x} \rangle_j k} \xi^{j+1}(x) \\
&= e^{i\langle \xi | \mathbf{x} | \xi \rangle \, k} e^{-i\langle \xi | \mathbf{k} | \xi \rangle \, x} e^{-i\langle \xi | \mathbf{k} | \xi \rangle \, \langle \mathbf{x} \rangle_j} \xi^{j+1}(x). \qquad (5.12)
\end{aligned}
$$

The derivation of equation (5.12) uses the lemma,

$$
e^{a\mathbf{k}} e^{b\mathbf{x}} = e^{a\mathbf{x}} e^{b\mathbf{k}} e^{iab}, \qquad (5.13)
$$

which is a corollary of the Zassenhaus formula (3.2), since

$$
e^{a\mathbf{x}+b\mathbf{k}} = e^{a\mathbf{x}} e^{b\mathbf{k}} e^{-\frac{1}{2}[a\mathbf{x},b\mathbf{k}]} = e^{b\mathbf{k}+a\mathbf{x}} = e^{b\mathbf{k}} e^{a\mathbf{x}} e^{\frac{1}{2}[a\mathbf{x},b\mathbf{k}]}. \qquad (5.14)
$$

5.2 Validation with Square Potentials

To confirm the capability of the interaction-picture approach to compute accurate Møller states and S-matrix elements, the process can be tested using an asymmetric square-well potential, with one asymptotic potential energy higher than the other (Figure 5.2). This potential is chosen because its transmission and reflection coefficients can be calculated analytically, and it exercises the capability of the channel-packet method to deal with disparate asymptotic energy levels. Square potentials, however, cannot be represented with complete accuracy on a discrete grid. No finite grid can support the true vertical slopes that characterize such a potential; however, a successful method will be able to demonstrate convergence toward the analytic solution as the potential is more accurately approximated.

5.2.1 Sources of Numerical Error.

All time-dependent propagation techniques are prone to error resulting from the discretization of continuous events. Position and momentum are considered as finite sets of non-contiguous points, usually separated by
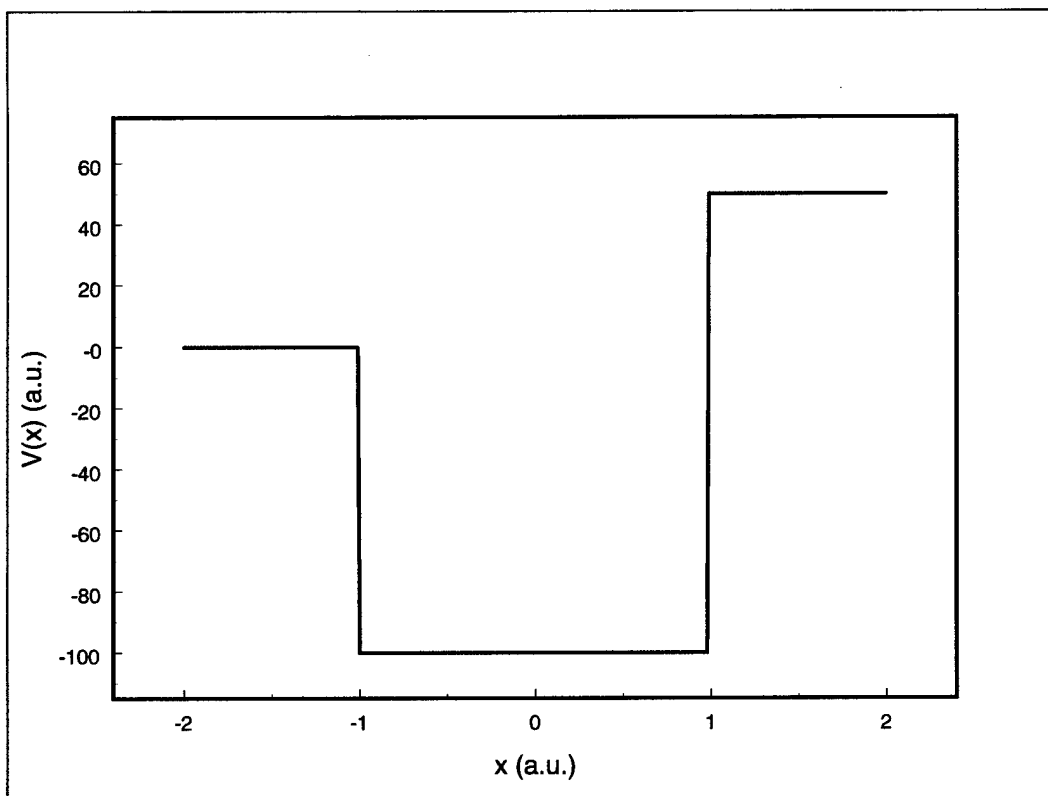
Figure 5.2   The asymmetric square-well potential used to validate the propagators. The well's discontinuities are at ±1 atomic unit, the well bottom is at -100 atomic units of energy, and the left and right asymptotes are at 0 and 50 atomic units.

constant spacings Δx and Δk to accommodate the FFT. Time also is divided into discrete intervals Δt. Decreasing the size of any of these intervals increases the accuracy of the numerical approximation, while increasing the numerical effort required. Discontinuous potentials such as the square well pose special numerical problems of their own. When expressed on a discrete coordinate grid, what should be square becomes trapezoidal, as the infinitesimal distance across the discontinuity is stretched out to a finite Δx. This effect is illustrated in Figure 5.3.
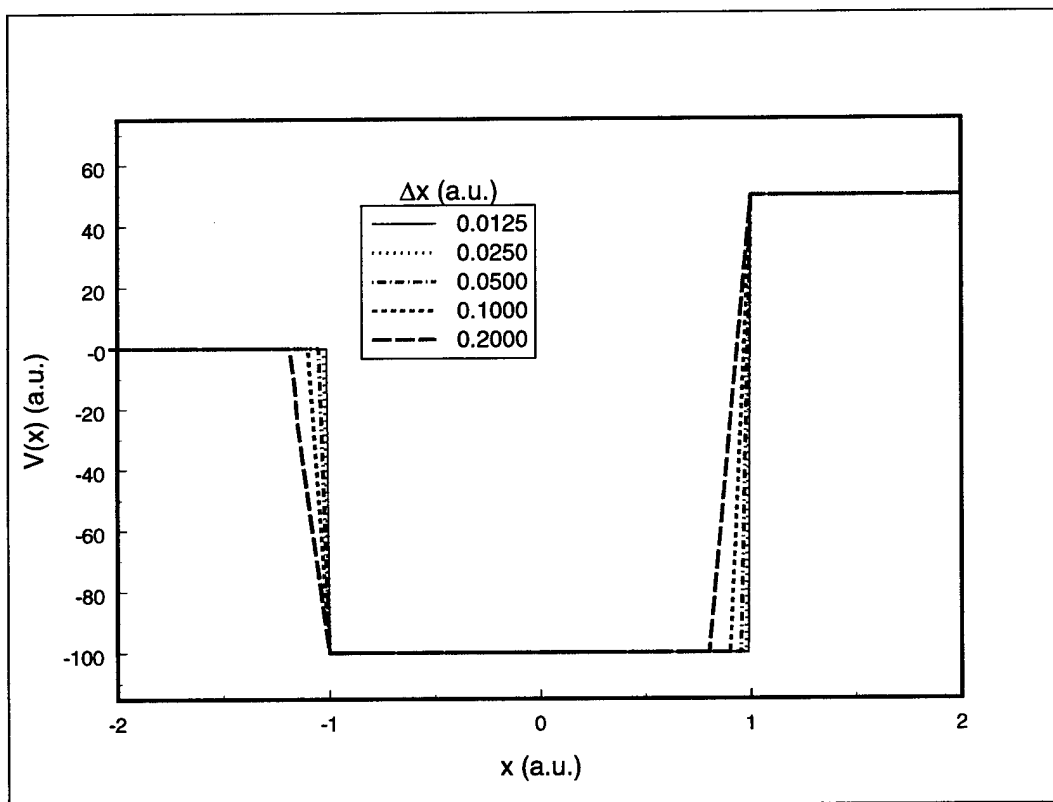
Figure 5.3   The asymmetric square well potential, to successively better approximations resulting from finer grid spacings.

5.2.2   Analytic Calculation of Transmission and Reflection Coefficients.   The analytic calculation of the probabilities of transmission and reflection is a straightforward but interesting exercise based on continuity of wavefunctions and their derivatives across

the discontinuities. Bohm's lucid treatment of the simple square well is easily adapted to accommodate one asymptote of the potential at nonzero energy(81). For a square well with left asymptote at energy $E = 0$, right asymptote at $E = V_1$, and well of width $2a$ at potential $-V_0$, the transmission coefficient from left to right is

$$T_1(E) = \left[\frac{1}{16} \left(A^2 + B^2 + 2AB \cos(4k_2 a) \right) \right]^{-1} \frac{k_3}{k_1}, \tag{5.15}$$

where

$$A = \left(1 + \frac{k_3}{k_2} \right) \left(1 + \frac{k_2}{k_1} \right), \tag{5.16}$$

$$B = \left(1 - \frac{k_3}{k_2} \right) \left(1 - \frac{k_2}{k_1} \right), \tag{5.17}$$

$$k_1 = \frac{\sqrt{2\mu E}}{\hbar}, \tag{5.18}$$

$$k_1 = \frac{\sqrt{2\mu(E + V_0)}}{\hbar}, \tag{5.19}$$

and

$$k_1 = \frac{\sqrt{2\mu(E - V_1)}}{\hbar}. \tag{5.20}$$

The probability of reflection for a wavepacket traveling from left to right is of course,

$$R_1 = 1 - T_1. \tag{5.21}$$

The analytic transmission and reflection coefficients for the square well of Figure 5.2 are shown in Figures 5.4 and 5.5.
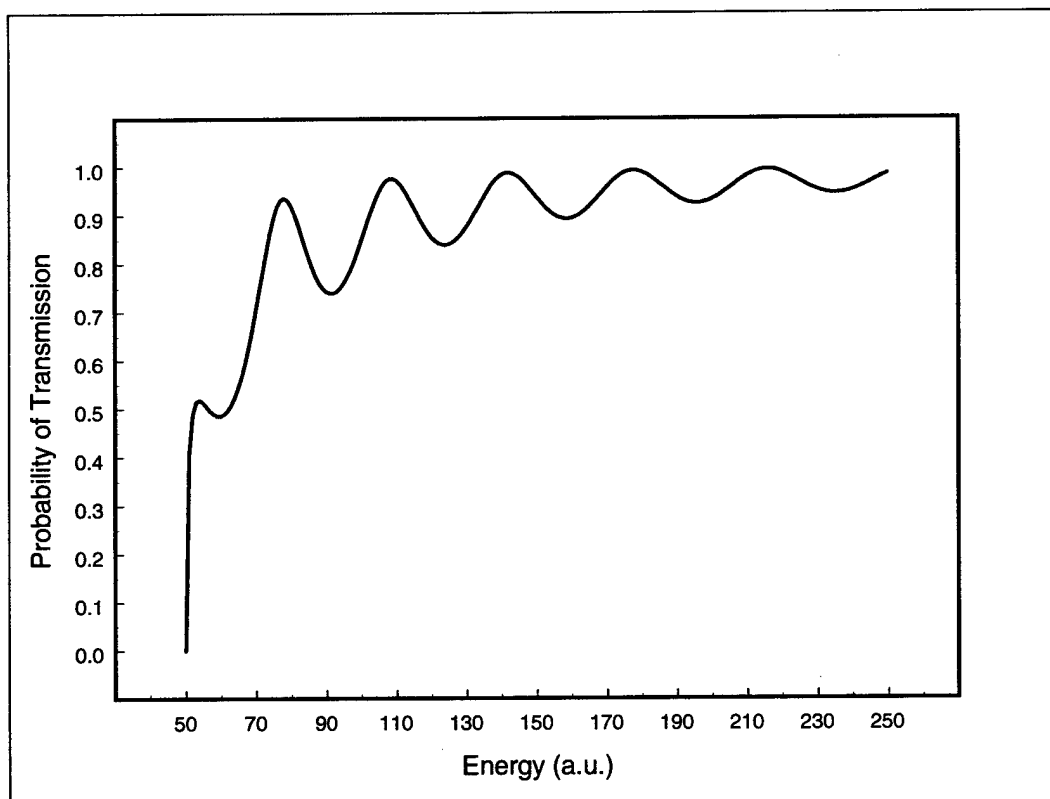
Figure 5.4   Transmission coefficient (from left to right) for the asymmetric square well.
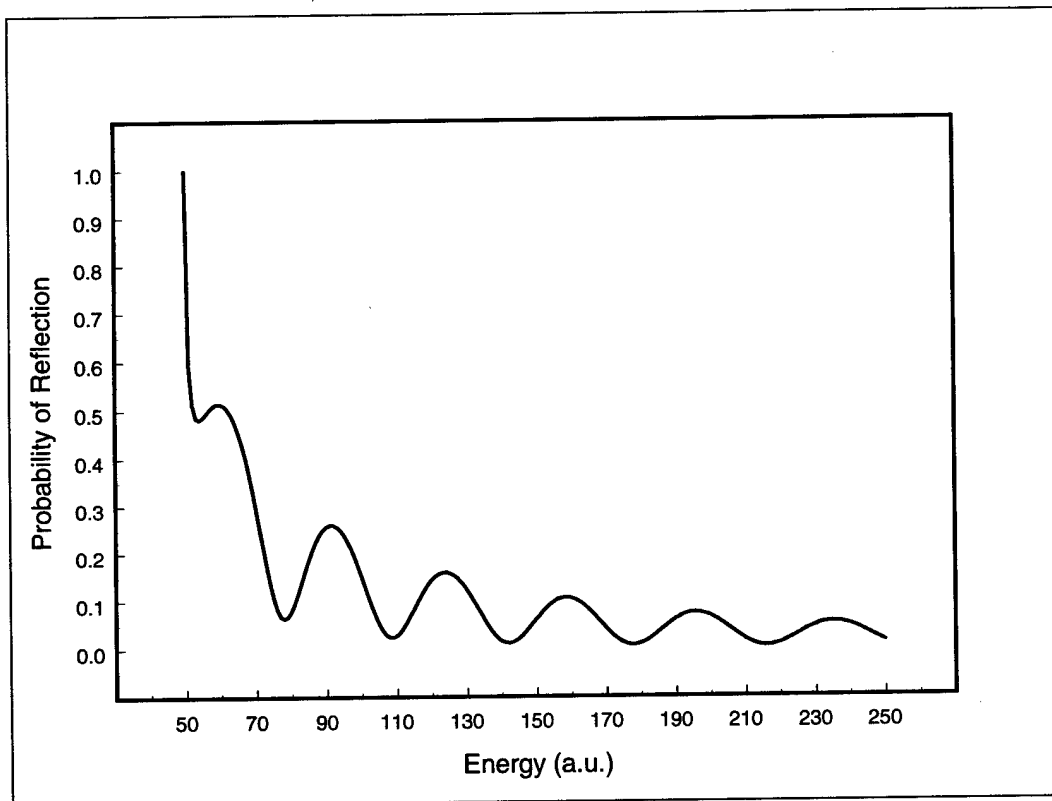
Figure 5.5   Reflection coefficient for the asymmetric square well.

5.2.3 Numerical Approximations of S-Matrix Elements. The square and trape-
zoidal potentials dealt with in this chapter are formed along the lines of Figure 5.3, with
anchors at the leftmost points of the well and right asymptote. Square potentials con-
structed in this manner approximate the desired width $2a$ of the discontinuous section to
the best ability of the computational grid. The alternative of anchoring the potentials at
the two ends of the well bottom would lead to an approximation to a true square potential
of width $2a - \Delta x$, with a different corresponding analytic transmission function for each
grid spacing. The choice of this configuration would lead to unnecessary error in calcula-
tions at larger grid spacings Δx, as the well widths diverged from the reference width. This
type of error is visible in a plot of transmission functions (Figure 5.6), where the period
of oscillation of the resonances in the transmission function can be seen to vary with the
grid spacing, corresponding to changing well widths (80). By contrast, a similar series of
calculations made with asymmetric potentials in the style of Figure 5.3 shows the period
of oscillation remaining constant as the propagation time step is varied (Figure 5.7).

Aside from the unavoidable error incumbent in the discretization of a discontinuous
potential, some error in wavepacket calculations is controlled by the selection of the grid
spacing Δx and the time step Δt, based on their conjugate relationships with momentum
and energy quantities, respectively(7). Let the maximum available energy in the system
be called

$$E_{\max} = E_{int} + T_{\max} + V_{\max}, \tag{5.22}$$

where E_{int} is internal energy (not present in these one-dimensional cases), $T_{\max} = \hbar^2 k_{\max}^2/2\mu$
is the maximum translational energy represented on the grid, and $V_{\max}$ the maximum po-
tential energy. The maximum momentum, $k_{\max} = \pi/\Delta x$, is fixed via the FFT by its
conjugate relationship with the coordinate grid. Therefore a coordinate spacing $\Delta x_{\max}$ ex-
ists, beyond which the momentum grid will not support the evolving wavepackets needed
for the channel-packet calculations. With regard to the time step Δt, similar conditions
exist with regard to $E_{\max}$. Specifically, the conjugate relationship between energy and time
requires that $\Delta t \leq \hbar/E_{\max}$.

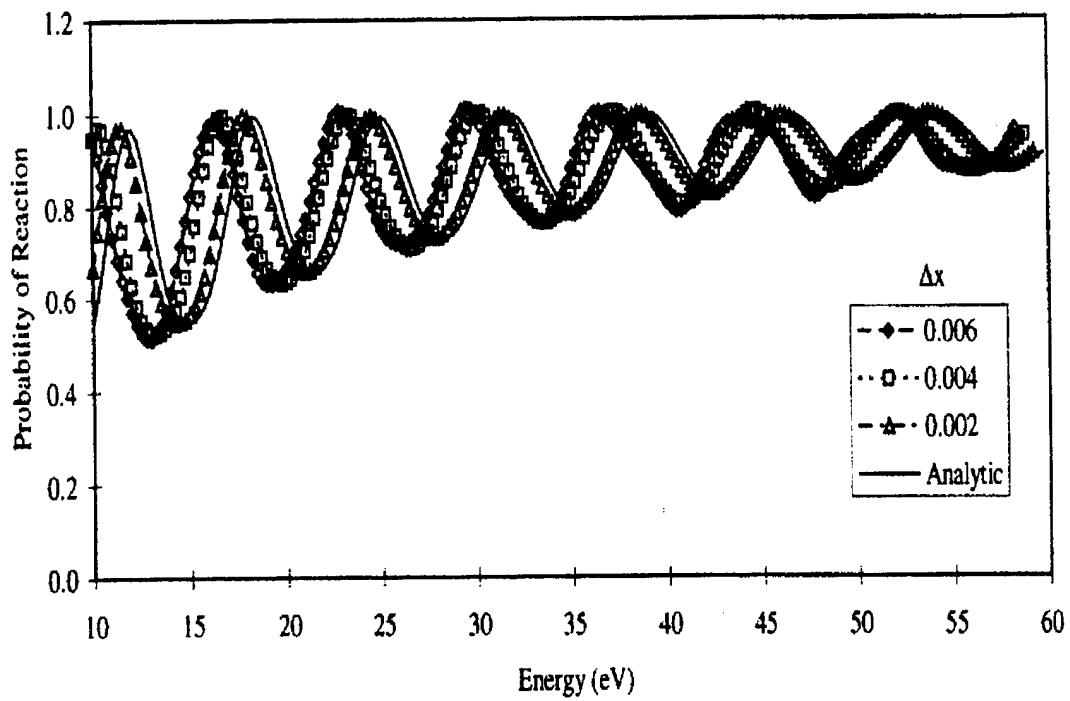Figure 5.6   Convergence behavior at decreasing grid spacings Δx for the transmission functions of a family of symmetric square wells whose width depends on the grid spacing(80).
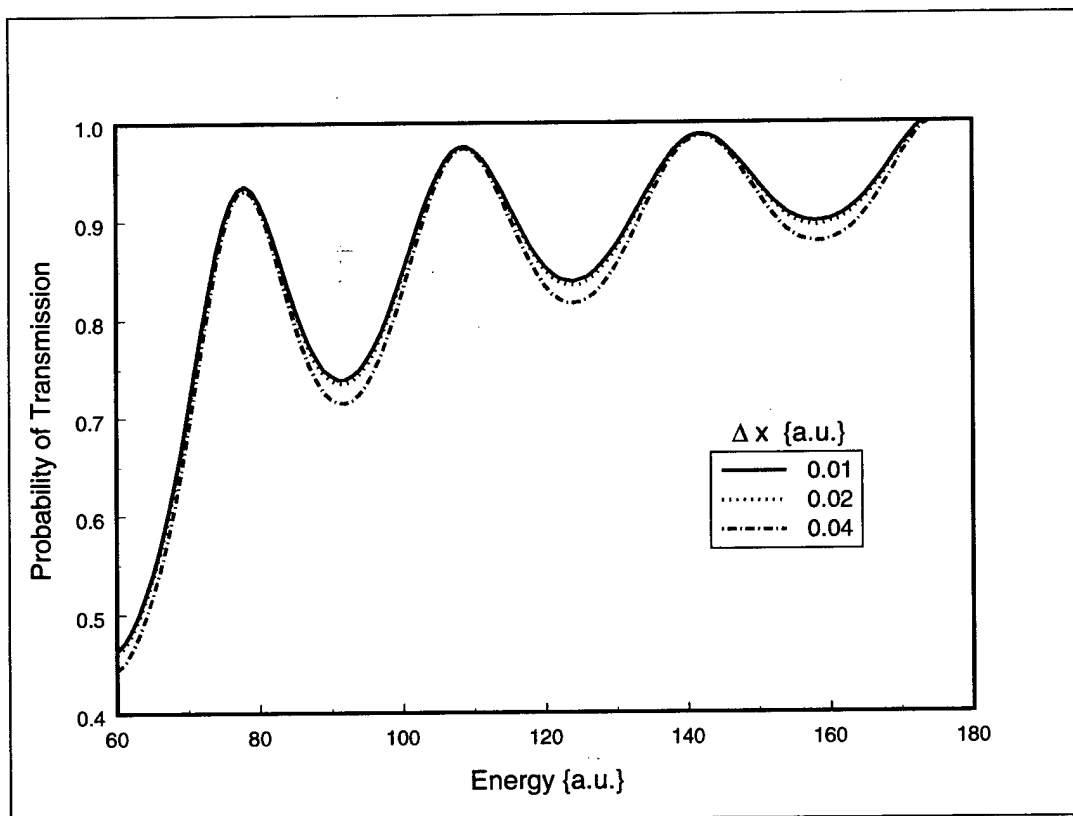
Figure 5.7   Transmission functions of some asymmetric square wells resembling Figure
5.3, made by the channel-packet method in the Schrödinger picture.

Variable	Value	Description
x_1	-1	Lowest coordinate in well
x_2	1	Lowest coordinate in right asymptotic channel
$-V_0$	-50	Potential energy in well
V_1	0	Potential energy of left asymptotic channel
V_2	100	Potential energy of right asymptotic channel

Table 5.1   Potential parameters held constant for all transmission-function calculations in this chapter. All quantities are in atomic units.

The potentials used in this chapter all share the parametric values given in Table 5.1. Grids are always chosen such that the anchor points at the leftmost ends of the well and the right asymptote both reside on the grid.

A baseline is needed to compare against the results of interaction-picture calculations for which no analytic solutions exist. This role is filled by a split-operator propagator. The split-operator method has become a standard propagation technique in the Schrödinger picture because it is very stable and delivers accurate results comparatively quickly(34). Three series of calculations were run in the Schrödinger picture for comparison to interaction-picture results. All three were transmission functions for various approximations to the asymmetric square potential of Figure 5.2. The first set fixes the coordinate spacing at $\Delta x = 0.0025$, and demonstrates the convergence of the transmission function toward the analytic version with decreasing computational time step Δt. The second set of calculations uses a fixed time step $\Delta t = 1.0 \cdot 10^{-5}$ atomic units, and demonstrates convergence as the coordinate spacing Δx is decreased. It is recognized that changes in accuracy in this series are related to both the decrease in the grid spacing and the improvement in the accuracy of the potential itself as finer grid spacing allows closer approach to truly vertical well walls. The third set of calculations explores this source of error in two ways. First, both Δt and Δx are fixed at $1.0 \cdot 10^{-5}$ atomic units and 0.01 atomic units respectively, and potentials with various degrees of slope in the sides of the well instead of the best possible square-well approximation are tested. Second, a trapezoidal potential is tested with a fixed distance $W = 0.08$ atomic units between the endpoints of the well bottom and the beginning points of the asymptotes, using $\Delta t = 1.0 \cdot 10^{-5}$ atomic units, on grids of various spacings Δx that represent the potential identically except for the number of

Variable	Value	Description
$-x_{\max}$	-10.24	Lowest value on coordinate grid for Møller states
σ	0.25	Width parameter for initial Gaussians $\psi_{in/out}(x)$
x_0	0	Position parameter for $\psi_{in/out}(x)$
k_0	12	Momentum parameter for $\psi_{in/out}(x)$
μ	1	Mass parameter for $\psi_{in/out}(x)$
τ	± 0.45	Asymptotic time

Table 5.2   Grid and wavepacket parameters held constant for all transmission-function calculations in this chapter. All quantities are in atomic units.

points sampled. This series isolates the source of degradation in accuracy with increased grid spacing to only the grid itself, holding the potential constant. The convergence of the transmission function for this series is measured relative to the calculation with the smallest Δx. To the greatest degree possible, the same parameters were used across all correlation-function calculations, in order to isolate the variation in the results to the portion of the S-matrix calculation that uses the interaction picture; namely, the derivation of the Møller states.

The parameters listed in Table 5.2 are common to all the calculations of transmission function, in both the Schrödinger and interaction pictures. The grid parameter N, the total number of grid points, is varied in tandem with the grid spacing Δx to hold the parameter $x_{\max} = N\Delta x$ constant for all calculations. This ensures that sufficient space will exist on the coordinate grid for the intermediate states $\psi_{in/out}(x, \tau)$.

All calculations use a modified version of Calfas' code for calculation of the correlation function, with the parameters given in Table 5.3 common to all(80). The code was modified for this project to support asymmetric potentials and to run on larger grids. The grid spacing Δx_C for the correlation function was always the same as that for the Møller states, and the number of grid points N_C for the correlation function was always twice the number used to calculate the Møller states. The grid for the correlation function can be this small because the code uses absorbing boundary conditions of the form,

$$V'(x) = \begin{cases} \pm iAe^{(x-x_b)^2/B} & |x| \geq x_b \\ 0 & \text{elsewhere} \end{cases}. \tag{5.23}$$

Variable	Value	Description
$-x_{\max_C}$	-20.48	Lowest value on coordinate grid for correlation function
A	$1.0 \cdot 10^{-4}$	Absorbing boundary condition multiplier (Equation 5.23)
Δt_C	$1.0 \cdot 10^{-5}$	Time step for correlation function
τ_1	-0.5	Negative asymptotic time
τ_2	1.0	Positive asymptotic time

Table 5.3   Grid and wavepacket parameters held constant for all correlation-function calculations in this chapter. All quantities are in atomic units.

In this chapter, all calculations of the correlation function used the value $A = 1.0 \cdot 10^{-4}$ given in Table 5.3, along with values of B chosen to make $|V'(x_{\max_C})| = 6$. Such boundary conditions were found for each grid by trial and error to prevent both reflection from and transmission across the grid boundary by wavepackets to any detectable degree. The value of x_b varies with the grid size.

The calculation of the transmission function from the correlation function can only be valid over a certain range of energies. It can be seen from equation 2.28 that this method can be numerically stable only over the range of energies where the wavefunction product $\eta_-^* \left(\pm k'_{\gamma'} \right) \eta_+ (\pm k_\gamma)$ is numerically appreciable. The energy spectra $\eta'_\pm (E)$ of the wavepackets ψ_{in} and ψ_{out} used in this chapter's calculations are shown with their product in Figure 5.8. Error in the transmission function is measured as the average,

$$\varepsilon = \frac{1}{n} \sum_{i=1}^{n} \frac{\left| f_i^{CPM} - f_i^{analytic} \right|}{f_i^{analytic}} \tag{5.24}$$

where the channel-packet result f_i^{CPM} is compared to the analytic function only at those contiguous energy values where the divisor $\eta'^*_- (E_i) \eta'_+ (E_i) \geq 0.01$. For the wavepackets used here, this energy range in atomic units is $67 \leq E \leq 157$.

5.2.3.1 Schrödinger-Picture Calculations.

Asymmetric Square Wells With Various Time Steps.   For the scenario of this calculation, with a fixed $\Delta x = 0.0025$ atomic units, the predicted maximum safe
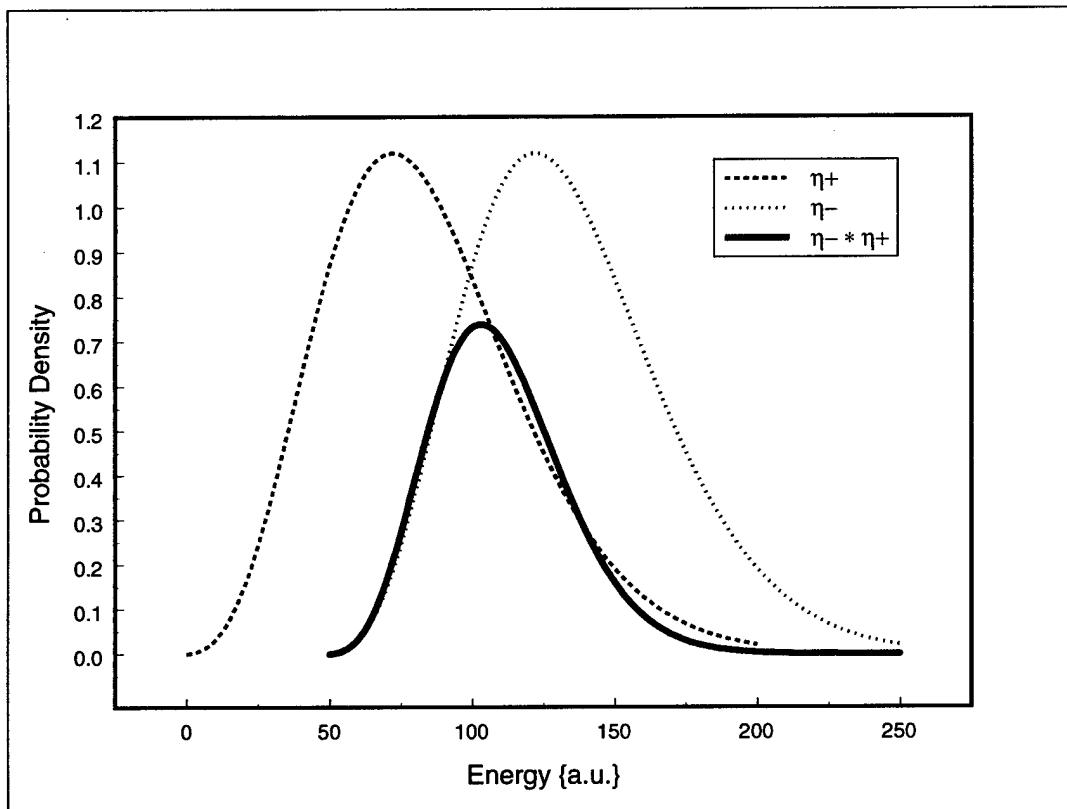
Figure 5.8   The product $\eta'^*_-(E_{in})\,\eta'_+(E_{out})$ and its components, the energy spectra of
the reactant and product wavepackets. Since this product is the divisor of
the formula for the S matrix, its spectrum bounds the range of energies over
which the S matrix may be calculated by the channel-packet method using a
given pair of initial states $\psi_{in/out}$.

time step is

$$\begin{aligned}
\Delta t_{max} &= \frac{\hbar}{E_{max}} \\
&= \frac{\hbar}{T_{max} + V_{max}} \\
&= \frac{\hbar}{\hbar^2 k_{max}^2 / 2\mu + V_{max}} \\
&= \frac{\hbar}{\hbar^2 \pi^2 / 2\mu \left(\Delta x\right)^2 + V_{max}} \\
&= \frac{1}{\pi^2 / 2 \left(0.0025\right)^2 + 100} \\
&= 1 \cdot 10^{-6}
\end{aligned} \tag{5.25}$$

in atomic units. This turns out to be unnecessarily conservative, based as it is on the maximum possible total energy in the model, rather than the maximum energy actually seen in the collision. As seen in Figures 5.9 and 5.10, accurate results are achieved over the selected energy range at much larger time steps. The momentum grid in a square-well model must necessarily have excess capacity, since the coordinate spacing $\Delta x = \pi / k_{max}$ must be made small in order to approximate the potential with accuracy.

Figure 5.10 shows an order of convergence of approximately 1.5 at the right end of the curve, and ceases to converge for time steps smaller than 0.0001 atomic units. The failure to continue to converge results from the inaccuracy in the potential inherent to the discrete representation with $\Delta x = 0.0025$ atomic units.

Asymmetric Square Wells With Various Coordinate Steps. A quadratic order of convergence is evident when the time step is held constant and the grid spacing is varied, as shown in Figure 5.11. In this case the convergence is limited by the finite time step $\Delta t = 1.0 \cdot 10^{-5}$ used throughout the calculations.

Asymmetric Trapezoidal Wells With Various Coordinate Steps. The previous result (Figure 5.11) includes two simultaneously varying quantities that contribute to error in the transmission function; one being the coordinate spacing itself, the other the variation of the potential that is incumbent in seeking the best approximation to the
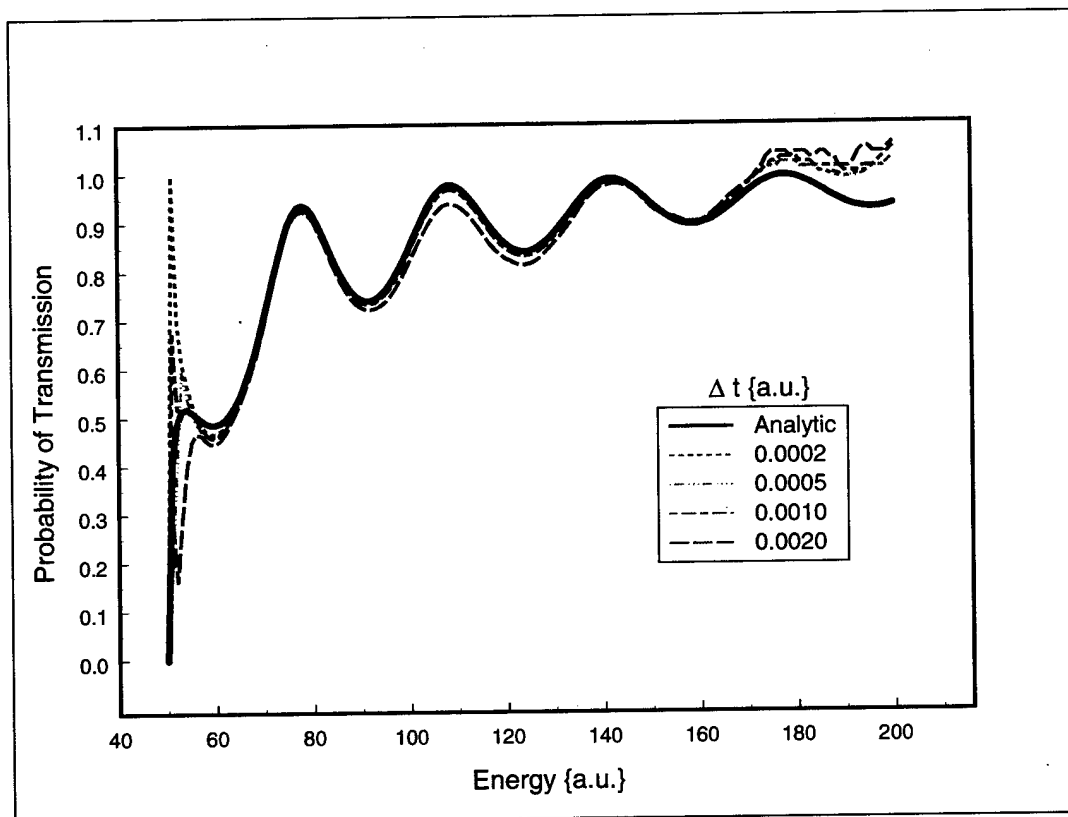
Figure 5.9 Transmission coefficient of the asymmetric square well for several choices of propagation time step Δt for the Møller states only. The correlation-function step of the channel-packet process uses $\Delta t_C = 1.0 \cdot 10^{-5}$ atomic units in all cases.
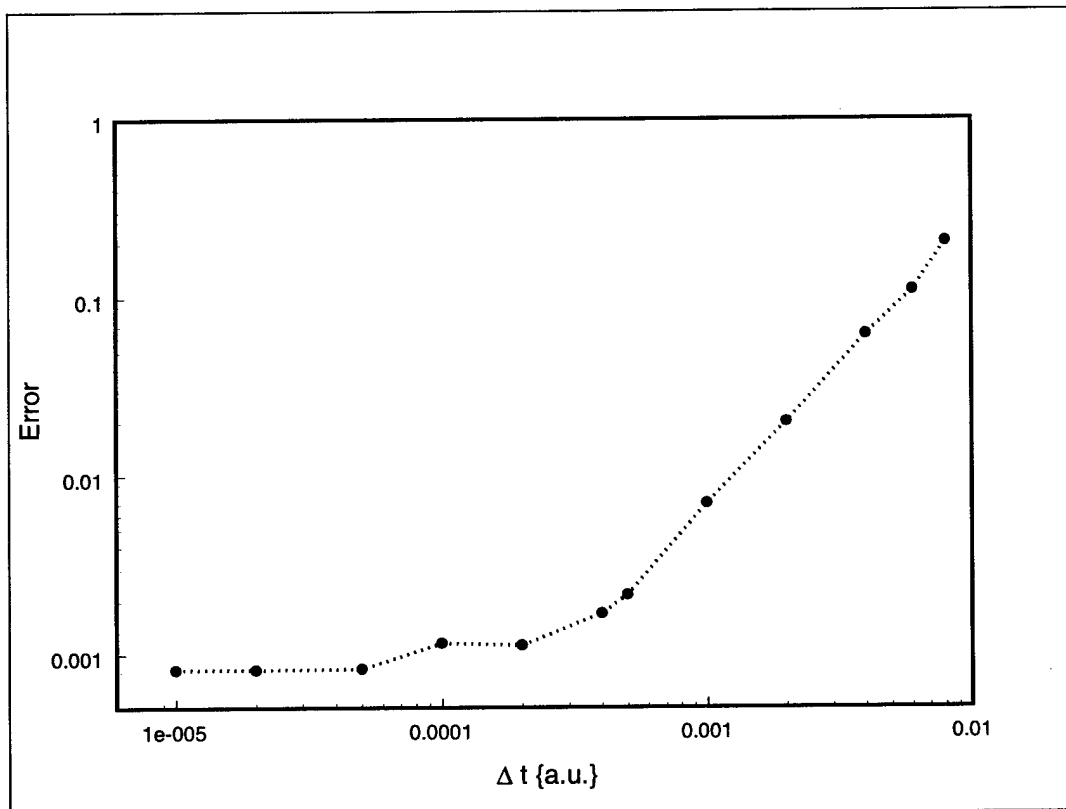
Figure 5.10   The error in the transmission coefficients of the asymmetric square well
transmission function as computed in the Schrödinger picture. Error is
computed using equation (5.24), with the analytic square-well potential as
the reference.
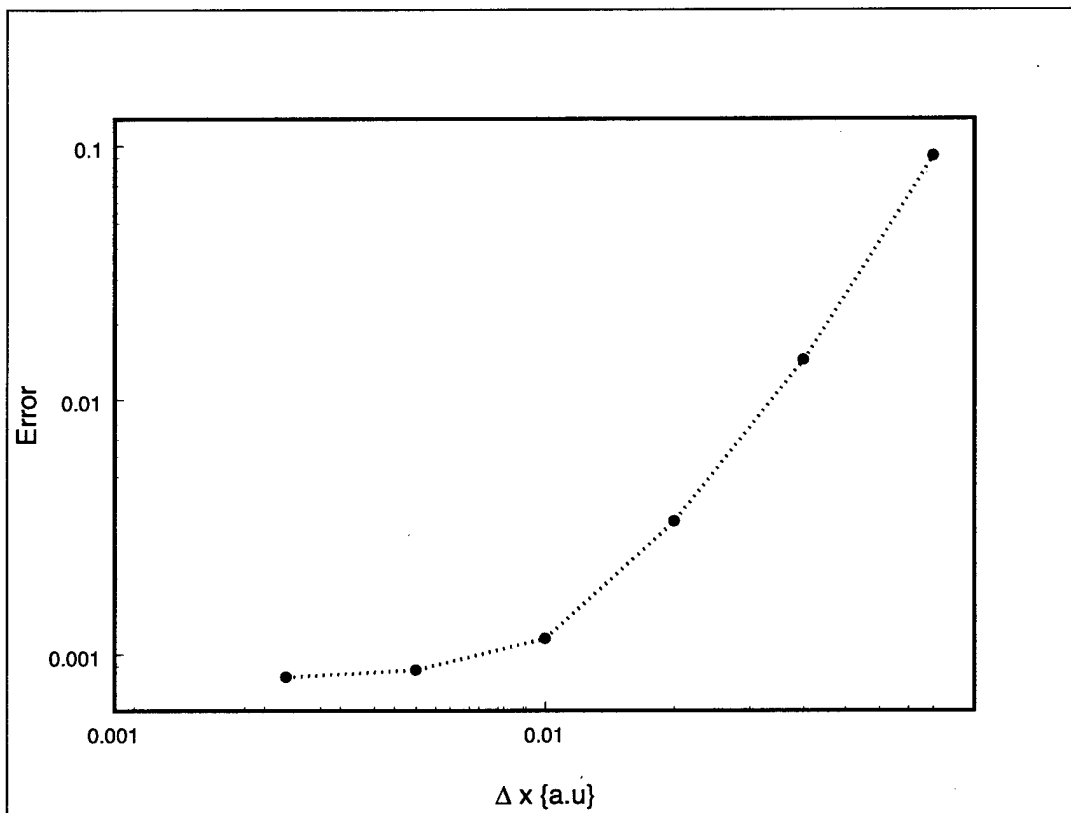
Figure 5.11   Convergence of the transmission coefficient for the asymmetric square well as the coordinate spacing Δx is decreased in the Schrödinger picture. The accuracy of the discrete representation of the square potential is also improving with decreasing Δx. Error is computed using equation (5.24), with the analytic square-well potential as the reference.

Grid Spacing of "Square" Well	Extra Points in Trapezoidal Well Sides	Equivalent Δx
0.01	0	0.01
0.02	1	0.02
0.04	3	0.04
0.08	7	0.08
0.16	15	0.16

Table 5.4   Summary of the potentials compared in Figures 5.12 and 5.17. The first and third columns are expressed in atomic units of distance. "Equivalent Δx" is seen to be idendical to the grid spacing of the "square" well that is being compared to the trapezoidal well on the grid with spacing $\Delta x = 0.01$ atomic units. The trapezoidal wells on the finer grid are formed by adding enough extra points to the well sides (between the outer points of the well bottom and the inner points of the asymptotes) that the slopes of the well sides become identical to the corresponding slopes of the "square" potentials on the coarser grids.

square potential that is possible in each grid. These factors can be examined one at a time by mimicking the trapezoidal configuration of the wells constructed on the more coarsely-spaced grids on grids with smaller Δx. Figure 5.12 holds the first factor constant, comparing the convergence of trapezoidal wells, all with $\Delta t = 1.0 \cdot 10^{-5}$ and $\Delta x = 0.01$ atomic units, with various numbers of extra points added to the well walls to make the potentials the same shape as the "square" potentials previously constructed on grids with larger values of Δx. For example, a well with one extra point between the inner ends of the asymptotes and the outer ends of the well is compared to one with no extra points (a "square" well) on a grid with $\Delta x = 0.02$ atomic units. Table 5.4 enumerates the comparisons depicted in Figure 5.12. The figure shows that the order of convergence to the analytic square-well solution remains quadratic when the same potentials are modeled on more finely spaced grids, with the finer grids showing somewhat improved accuracy in the transmission function relative to those computed on the same potential using a coarser grid.

Figure 5.13 addresses the second factor. Here a single trapezoidal shape is maintained with distance $W = 0.08$ atomic units between the rightmost point of the well bottom and the leftmost point of the right asymptote, while the coordinate spacing is varied over the range $0.0025 \leq \Delta x \leq 0.08$ atomic units. Quadratic convergence of the transmission
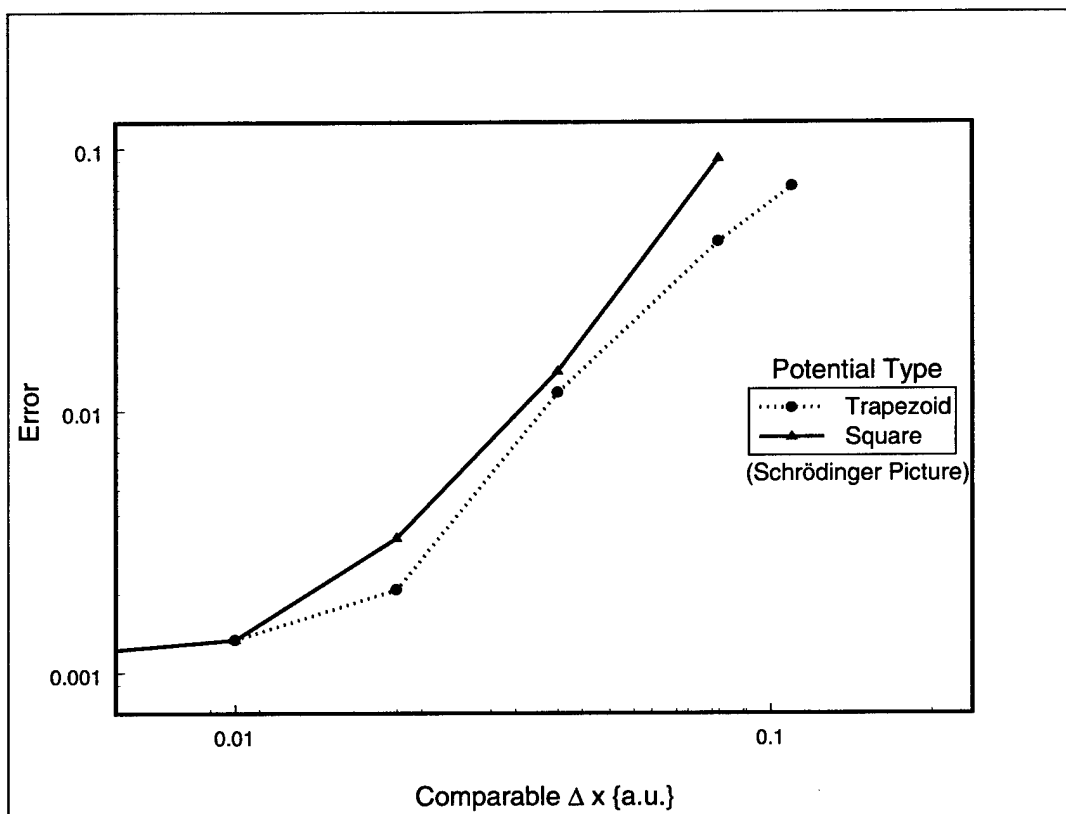
Figure 5.12   Error in transmission coefficients for asymmetric trapezoidal well potentals (dotted curve), compared to those for the corresponding asymmtetric square wells on coarser numerical grids (solid curve). The trapezoidal wells have no grid points within the well walls for $\Delta x = 0.01$, one for $\Delta x = 0.02$, three for $\Delta x = 0.04$, and so on, as enumerated in Table 5.4. The entire channel-packet calculation is done in the Schrödinger picture. Error is computed using equation (5.24), with the analytic square-well potential as the reference.
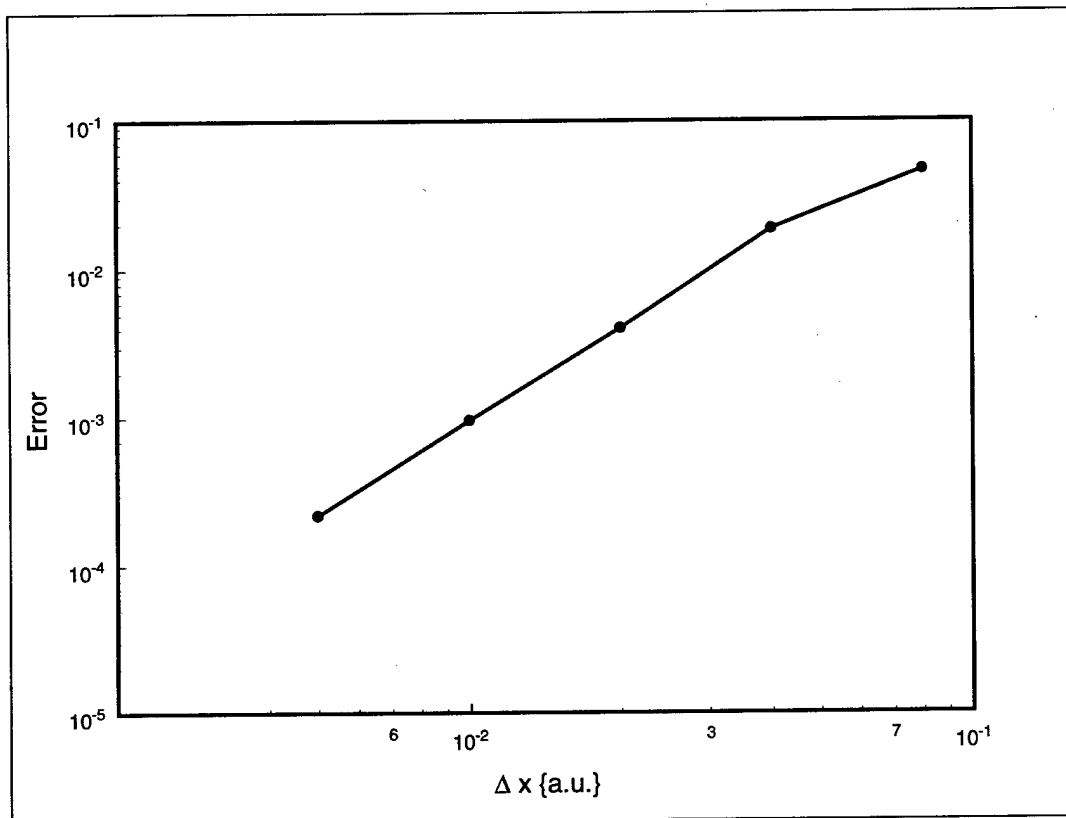
Figure 5.13   Convergence in the Schrödinger picture of the transmission function for a trapezoidal well of fixed shape as coordinate spacing Δx is varied. The reference transmission function uses $\Delta x = 0.0025$ atomic units. All calculations use $\Delta t = 1.0 \cdot 10^{-5}$ atomic units.

function is seen, not, of course, toward the analytic square-well transmission function, but toward the most accurate calculation of the transmission function for this particular trapezoidal well; namely, the calculation performed using the smallest grid spacing.

5.2.3.2   Interaction-Picture Calculations.

Asymmetric Square Wells With Various Time Steps.   For larger time steps in the Møller-state calculation, the interaction-picture approach shows linear convergence behavior, at a higher level of error than in the Schrödinger picture for a given time step Δt. This is illustrated in Figure 5.14. The interaction-picture calculation of the Møller
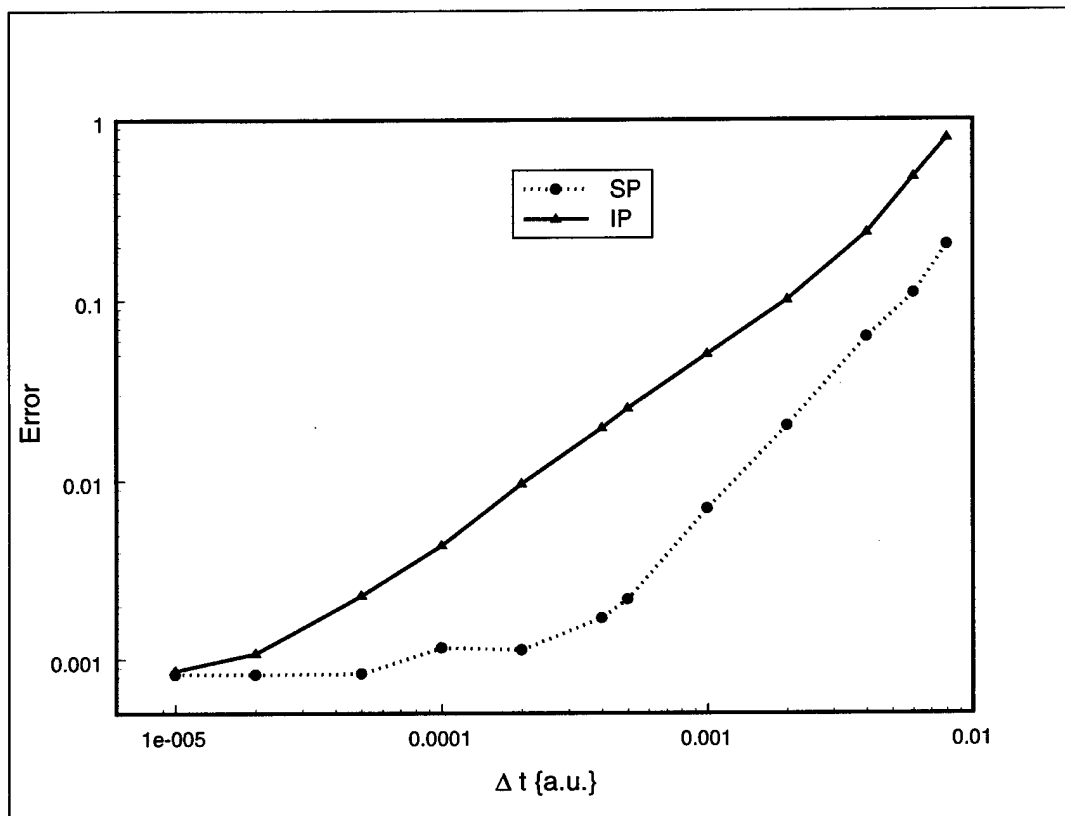
Figure 5.14   Convergence with decreasing time step Δt of transmission functions computed in the Schrödinger picture using Møller states produced in the interaction picture, compared to transmission functions produced entirely in the Schrödinger picture. Error is computed using equation (5.24), with the analytic square-well potential as the reference.

states, while still limited by the common use of the fixed time step $\Delta t_C = 1.0 \cdot 10^{-5}$ in the Schrödinger picture for the calculation of the correlation function, appears ultimately to converge to a result of equal accuracy to that achieved by calculation of the Møller states in the Schrödinger picture at the shortest time steps. This is reasonably seen as an effect of the time dependence of the interaction-picture Hamiltonian. Discontinuous or rapidly varying potentials such as square and highly sloped trapezoidal wells and barriers would be expected to cause the interaction-picture Hamiltonian to vary rapidly in time while the wavepackets are in the interaction region of the potential.

Asymmetric Square Wells With Various Coordinate Steps.   The convergence behavior of the transmission function based on interaction-picture Møller states as coordinate spacing Δx decreases is consistent with this interpretation. At the chosen small value $\Delta t = \Delta t_C = 1.0 \cdot 10^{-5}$ atomic units, Figure 5.14 predicts equal accuracy between the Schrödinger and interaction pictures. Figure 5.15 confirms this prediction, with an indication at the largest grid spacing, where its Hamiltonian is the least time-dependent, of somewhat more accurate results than the Schrödinger picture at the common time step. A similar experiment using the common time step $\Delta t = \Delta t_C = 1.0 \cdot 10^{-4}$ makes the point even more nicely, as shown in Figure 5.16. Use of the longer time step exposes the interaction picture to increased error relative to the Schrödinger picture for the more steeply sloped potentials, while remaining of comparable accuracy for the less steeply sloped potentials. Constraints on the coordinate grid required to keep the potential's anchor points at $x = \pm 1$ atomic unit on the grid restrict the available number of large values of Δx below the momentum-grid limit. Both the interaction-picture and the Schrödinger methods appear to converge toward the analytic result approximately quadratically in this scenario.

Asymmetric Trapezoidal Wells With Various Coordinate Steps.   The interaction picture does not show the same benefit from decreasing the coordinate spacing as the Schrödinger picture in the test used here, where the time step is held constant and the coordinate spacing is held constant at $\Delta x = 0.01$ atomic units, while the slope of the well sides is varied. The interaction picture remains similar in accuracy to the Schrödinger picture at this time-step size, as shown in Figure 5.17.

Figure 5.18 demonstrates that the interaction picture converges similarly toward the benchmark Schrödinger-picture calculation of the transmission function for the fixed-shape trapezoidal well as grid spacing decreases. Not surprisingly, the approach of the interaction-picture version to the benchmark ceases at higher grid resolutions as the interaction picture converges to its own best version of the transmission function.
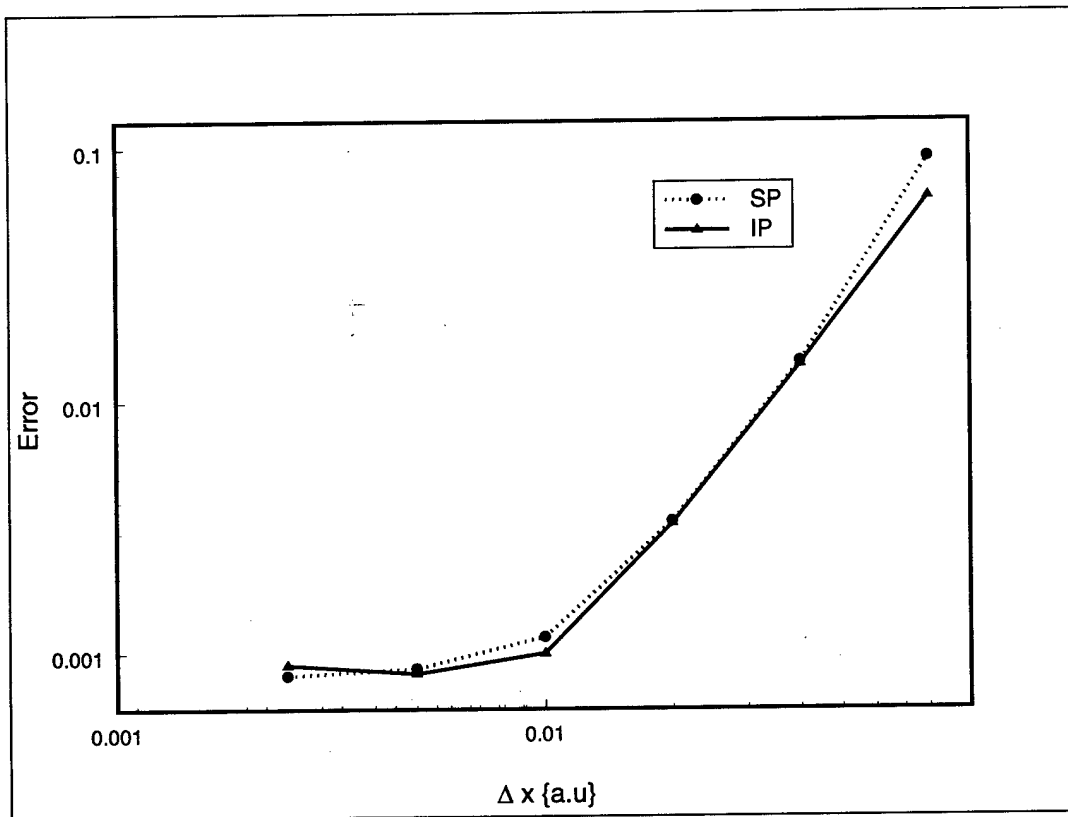
Figure 5.15   Error with varying grid spacing Δx of transmission functions for the asymmetric square well with Møller states computed in the interaction picture, compared to results obtained entirely in the Schrödinger picture. These calculations use $\Delta t = \Delta t_C = 1.0 \cdot 10^{-5}$ atomic units. Error is computed using equation (5.24), with the analytic square-well potential as the reference.
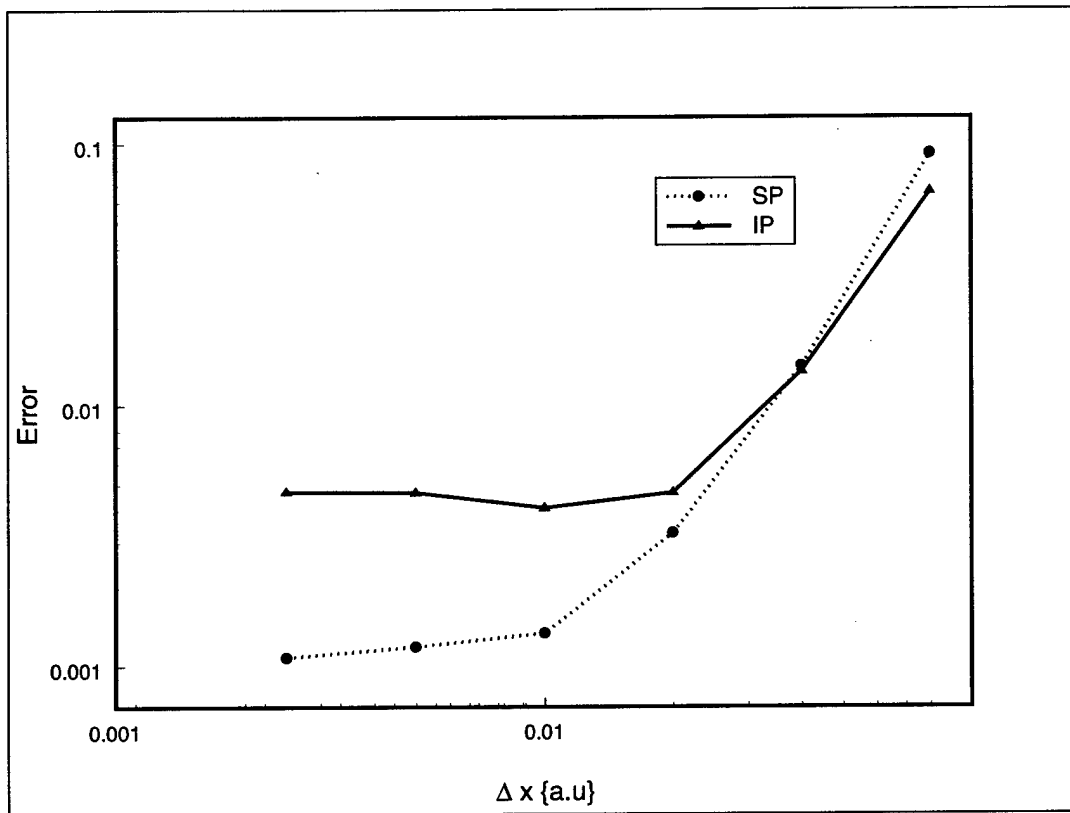
Figure 5.16   Error with varying grid spacing Δx of transmission functions for the asymmetric square well with Møller states computed in the interaction picture, compared to results obtained entirely in the Schrödinger picture. These calculations use $\Delta t = \Delta t_C = 1.0 \cdot 10^{-4}$ atomic units. Error is computed using equation (5.24), with the analytic square-well potential as the reference.
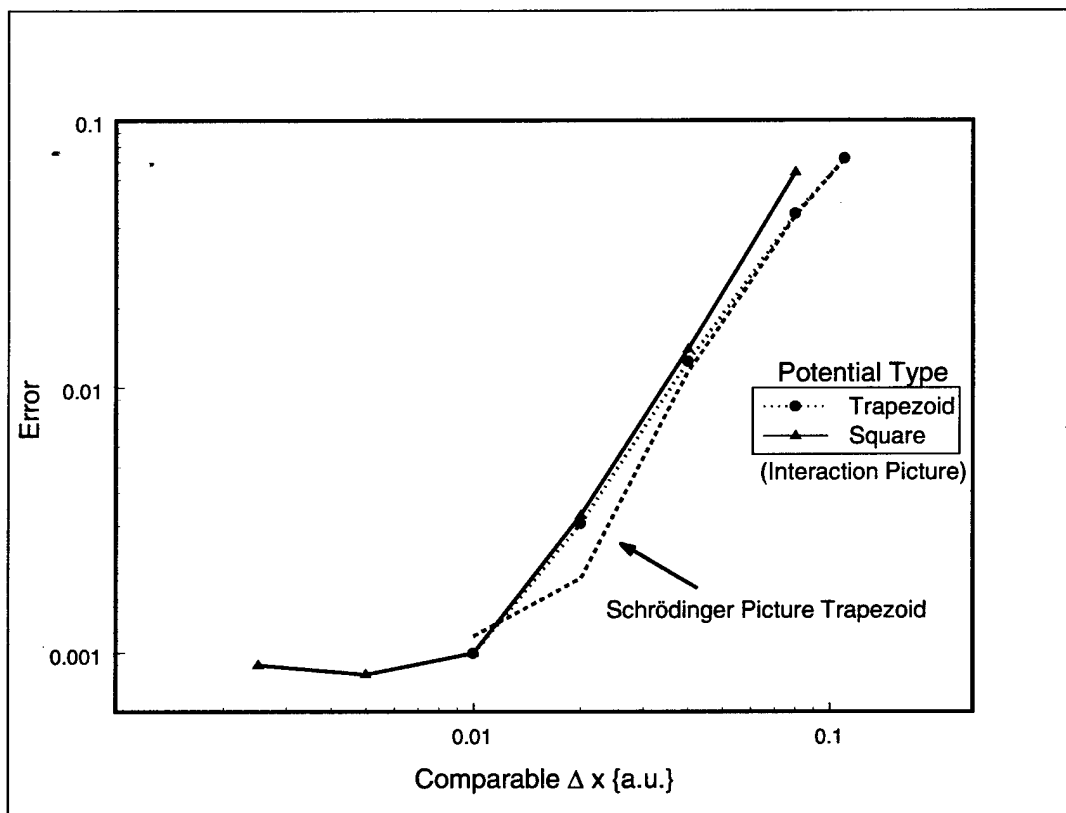
Figure 5.17   Error in transmission functions for asymmetric trapezoidal well potentals (dotted curve), compared to those for the corresponding asymmtetric square wells on coarser numerical grids (solid curve). The trapezoidal wells have no grid points within the well walls for $\Delta x = 0.01$, one for $\Delta x = 0.02$, three for $\Delta x = 0.04$, and so on, as enumerated in Figure 5.4. The Møller states for these channel-packet calculations are obtained in the interaction picture. The equivalent curve for trapezoidal wells modeled in the Schrödinger picture (dashed line) is included for comparison. Error is computed using equation (5.24), with the analytic square-well potential as the reference.
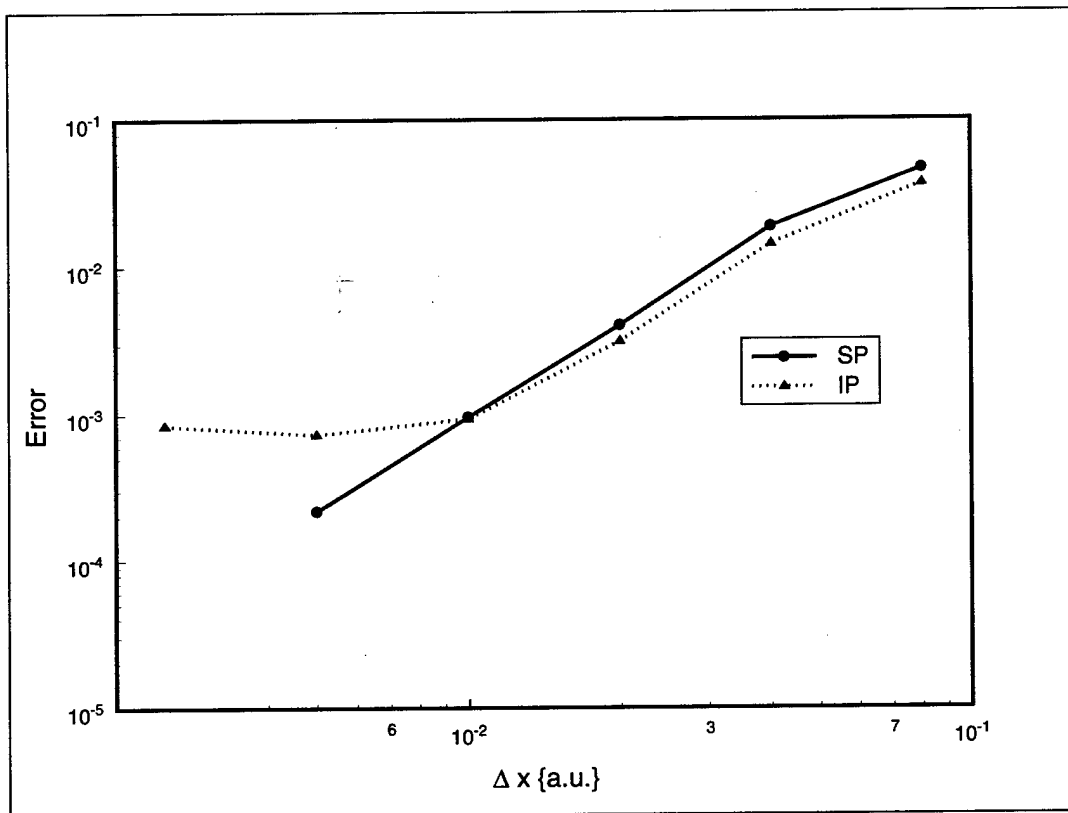
Figure 5.18   Convergence in the interaction picture of the transmission function for a trapezoidal well of fixed shape as coordinate spacing Δx is varied. The reference transmission function uses $\Delta x = 0.0025$ atomic units in the Schrödinger picture. All calculations use $\Delta t = 1.0 \cdot 10^{-5}$ atomic units.

5.3 Summary

The Schrödinger-picture split-operator propagator delivers results that improve in accuracy consistently with increasing coordinate and time sampling rates. It can be used as a basis for comparison for the interaction-picture propagator. The calculation of Møller states in the interaction picture is also a valid technique, but must take into account the rapidity of changes in the potential in the choice of time steps in order to achieve accuracy similar to that attained by the Schrödinger-picture method.

VI. Application of the Interaction Picture in Reactive Scattering

This chapter uses Møller-state and S-matrix calculations on various one-dimensional potentials to demonstrate the utility of the interaction picture in reactive scattering calculations. Various potentials of the general form (Figure 6.1),

$$V(x) = Ae^{-\alpha(x-a)^2} - Be^{-\beta(x-b)^2} + Ce^{-\gamma(x-c)^2} + D\Theta(x-a)\Theta(c-x)x + V_0\Theta(x-a),$$

$$(6.1)$$

where $\Theta(x)$ represents a Heaviside step function, are chosen to schematically represent the reaction path of a reactive molecular collision that may have two different asymptotic Hamiltonians. A potential barrier of the form

$$V(x) = A\,\mathrm{sech}\,(Bx) \tag{6.2}$$

is used to demonstrate a type of case where the interaction picture is advantageous relative to the Schrödinger picture for the channel-packet technique.

6.1 Application to a Reactive Potential

The channel-packet method's applicability to potentials with multiple asymptotic potential energies was demonstrated in both the interaction and Schrödinger pictures in Chapter V. For this potential, as $x \to -\infty$, the asymptotic Hamiltonian is

$$\mathbf{H}_a^L = \mathbf{p}^2/2\mu, \tag{6.3}$$

and as $x \to -\infty$, the asymptotic Hamiltonian is

$$\mathbf{H}_a^R = \mathbf{p}^2/2\mu + V_0. \tag{6.4}$$

An example using the values for the parameters in equation (6.1) given in Table 6.1 appears as the dotted curve in Figure 6.2.

6-1
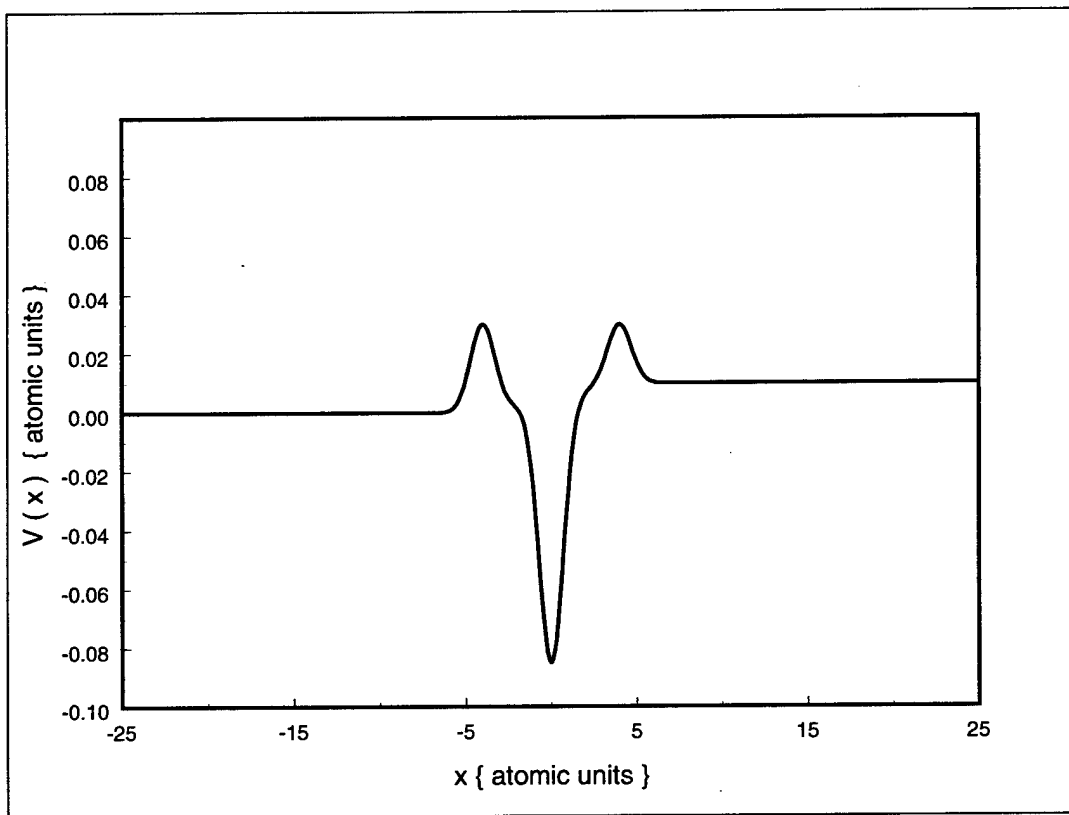
Figure 6.1   An asymmetric triple Gaussian potential.

Parameter	Value
A	0.03
B	0.09
C	0.02
D	0.00125
a	-4.0
b	0.0
c	4.0
α	1.0
β	1.0
γ	1.0

Table 6.1   The coefficients used in Equation 6.1 to create the potential function that appears in Figures 6.2 *et. seq.* All quantities use atomic units.

Parameter	Value
x_0	0.0
k_0	8.5
σ	0.55
μ	1224

Table 6.2   The coefficients used in Equation 5.3 to create the asymptotic wavepackets shown in Figure 6.2. All quantities use atomic units.

The transmission function of this potential can be computed by the channel-packet method using the interaction picture, beginning with the product and reactant wavepackets shown in Figure 6.2. The choice of $+k_0$ in equation (5.3) will yield the probability, as a function of kinetic energy, that reactants approaching from the left will form products exiting to the right. The values of the coefficients used in equation (5.3) used to generate the reactant and product states are given in Table 6.2. In the Schrödinger picture, the first propagation in equation (2.18) is performed analytically(27), using the initial wavepackets together with $\mathbf{H}_a^L$ and $\mathbf{H}_a^R$ to obtain intermediate reactant and product wavepackets respectively. As shown in Figure 6.3, these wavepackets undergo both translation and spreading relative to the initial wavepackets.

Typically, this wavepacket translation and spreading in the Schrödinger picture generates a requirement for large grids. However, in the interaction picture, the intermediate wavepackets do not translate or spread, and remain identical to the initial wavepackets. Figure 6.3 also illustrates the intermediate interaction-picture channel packets, and demon-
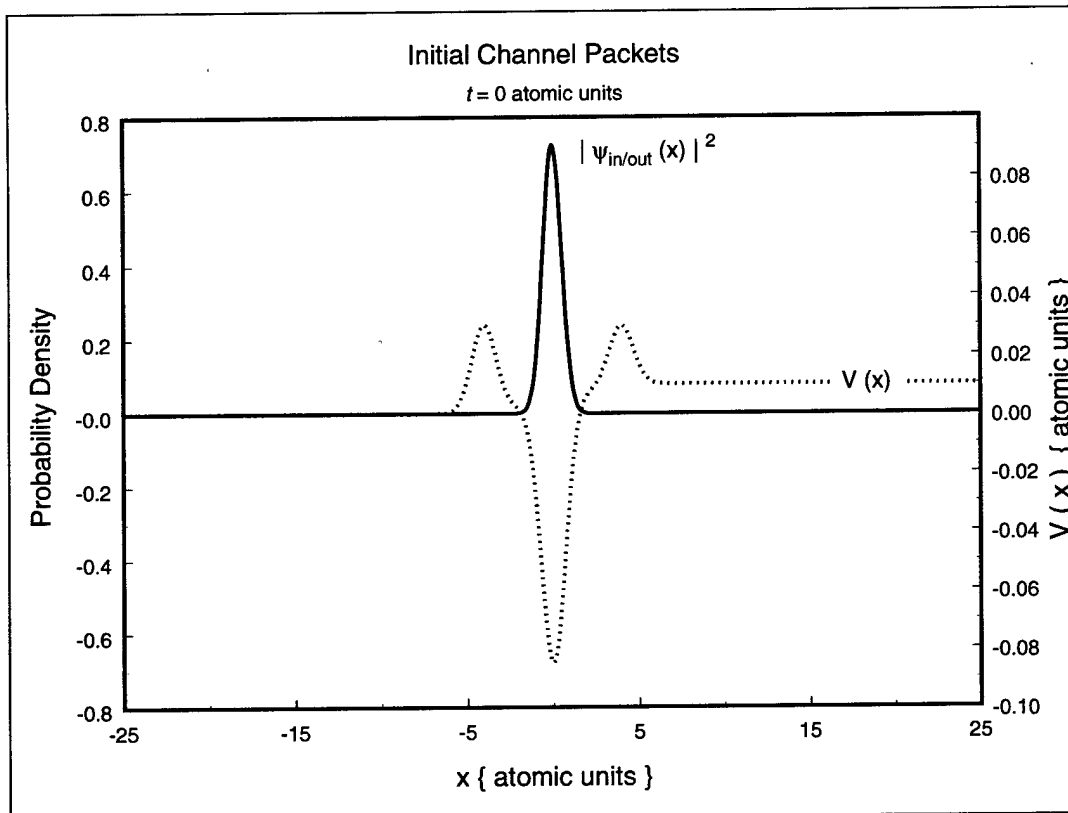
Figure 6.2   The initial channel packets $\psi_{in}(x)$ and $\psi_{out}(x)$ (solid line), are the same in the interaction and Schrödinger pictures, since they are evaluated at $t = 0$. The potential (dotted line) is the sum of two Gaussian barriers, a Gaussian well, and a ramp function which is zero for $x < -4$, 0.01 for $x > 4$, and rises linearly in between.
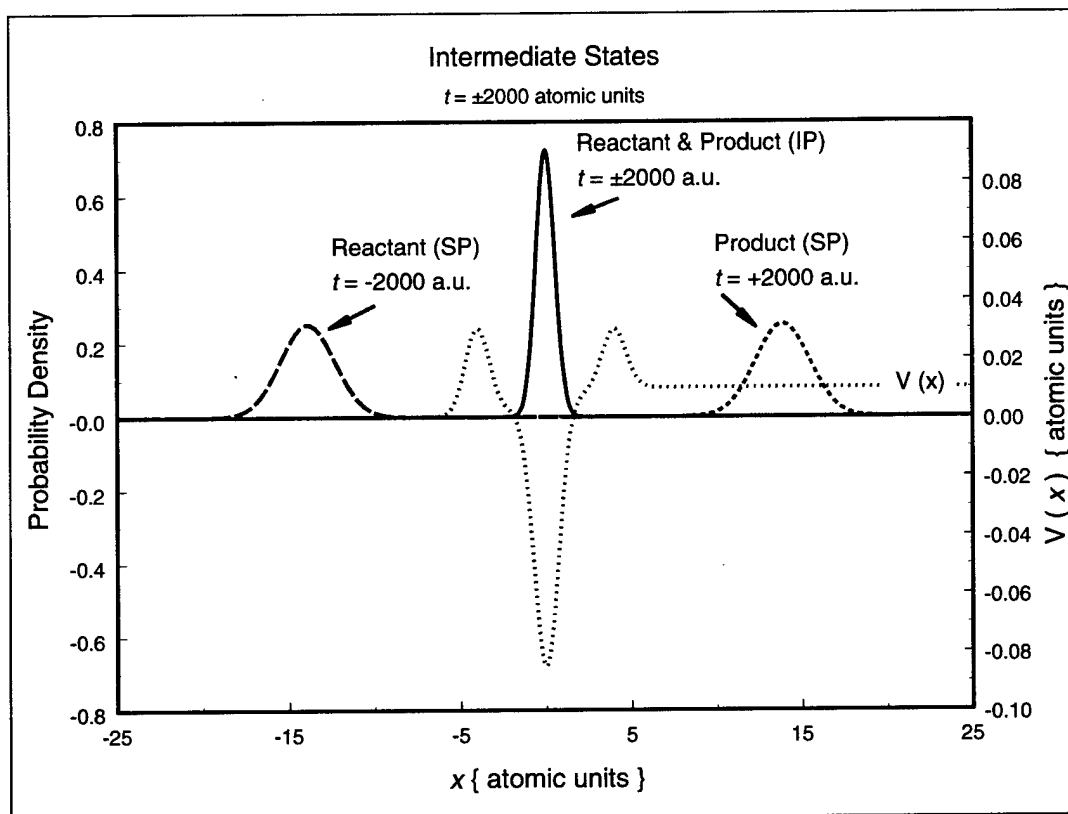
Figure 6.3   The reactant channel packet propagated backward in time to $t = -2000$ atomic units, and the product channel packet propagated forward in time to $t = 2000$ atomic units. Since the propagation occurs under a free-particle Hamiltonian, the wavepackets are unaffected in the interaction picture (solid line). The Schrödinger-picture packet (dashed lines) translates to the left (reactant, long dashes) or right (product, short dashes), and spreads, requiring a larger grid.

Parameter	Value
τ	± 2000
t_0	8.5
Δt_I	0.5
Δt_S	1.0

Table 6.3 The quantities associated with the generation of the intermediate states in Figure 6.3 and the Møller states in Figure 6.4. Intermediate states (Figure 6.3) are calculated analytically for the Gaussian asymptotic states at time $\tau = -2000$ atomic units for the reactant state, and $\tau = +2000$ atomic units for the reactant state. Møller states (Figure 6.4) are generated by propagating the intermediate states to the time $t_0 = 0$, using the computational time step $\Delta t_I = 0.5$ atomic units in the interaction picture, and $\Delta t_S = 1.0$ atomic units in the Schrödinger picture.

strates that they require a smaller grid when compared with the intermediate Schrödinger-picture wavepackets. In the interaction picture, the intermediate wavepackets are used in equation (3.36) together with the appropriate asymptotic Hamiltonian to compute the reactant and product Møller states. The Møller states shown in Figure 6.4 were computed on a grid of 256 points using the nested interaction picture with a four-dimensional Krylov subspace. Constants used for the propagation are listed in Table 6.3. For comparison, the same Møller states are computed in the Schrödinger picture, requiring a grid of 512 points.

To complete the calculation, the Møller states were propagated in the Schrödinger picture using a split-operator propagator together with absorbing boundary conditions to compute the correlation function in equation (2.26), represented in Figure 6.5(23,80). S-matrix elements are then computed using equation (2.28), resulting in the probability for reaction shown in Figure 6.6. For comparison, the probability of reaction computed entirely within the Schrödinger picture is also shown in Figure 6.6. It is important to note that since short iterative Lanczos propagation is employed when using the nested interaction picture, a greater number of FFTs is required per time step when compared to the split-operator approach commonly used for time-independent Hamiltonians in the Schrödinger picture.
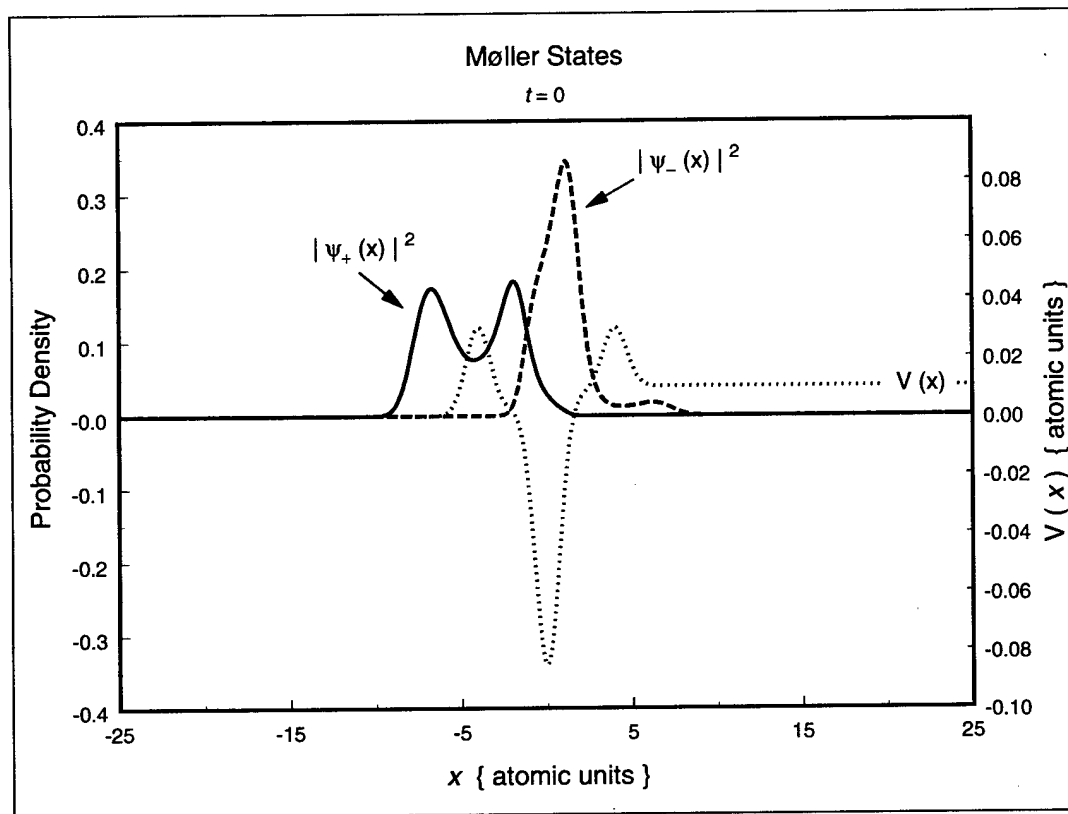
Figure 6.4 The reactant Møller state, $\psi_+(x)$ (solid line), is the result of propagating the intermediate reactant state forward in time to $t = 0$, where the interaction and Schrödinger pictures are again identical. The dashed line is the product Møller state, $\psi_-(x)$, the result of propagating the intermediate product state backward in time to $t = 0$.
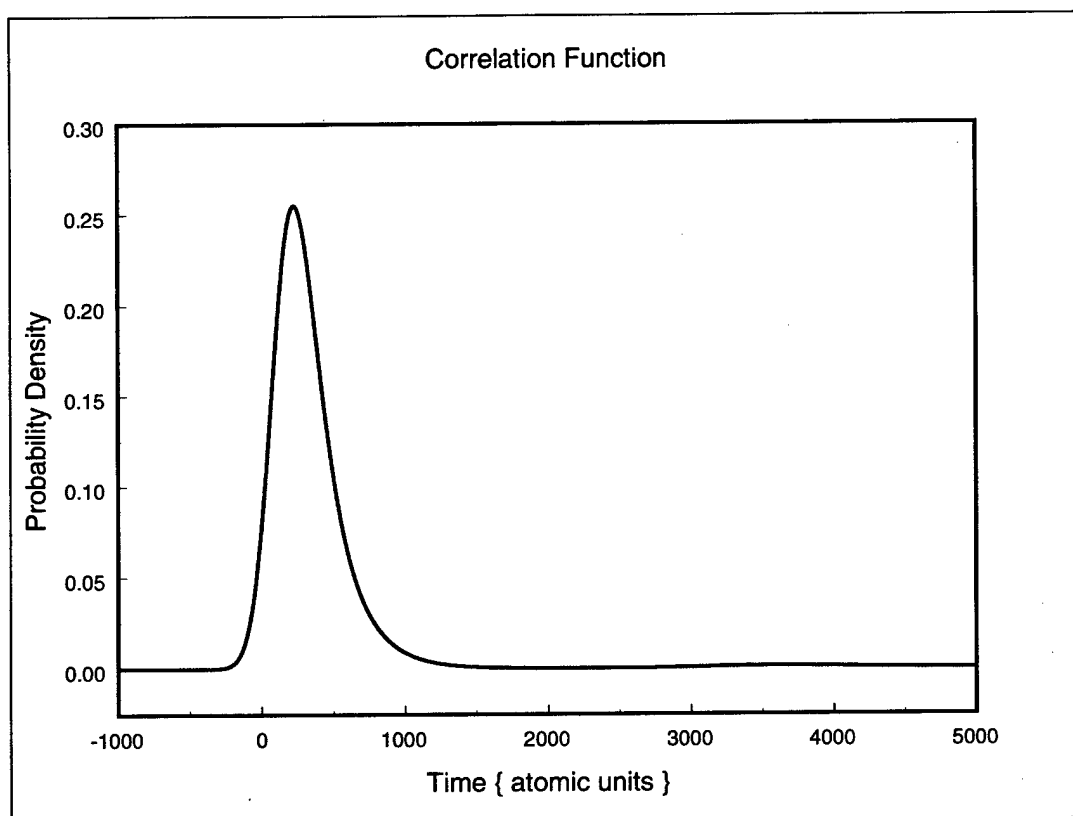
Figure 6.5 The absolute value squared of the correlation function, computed using equation (2.26).
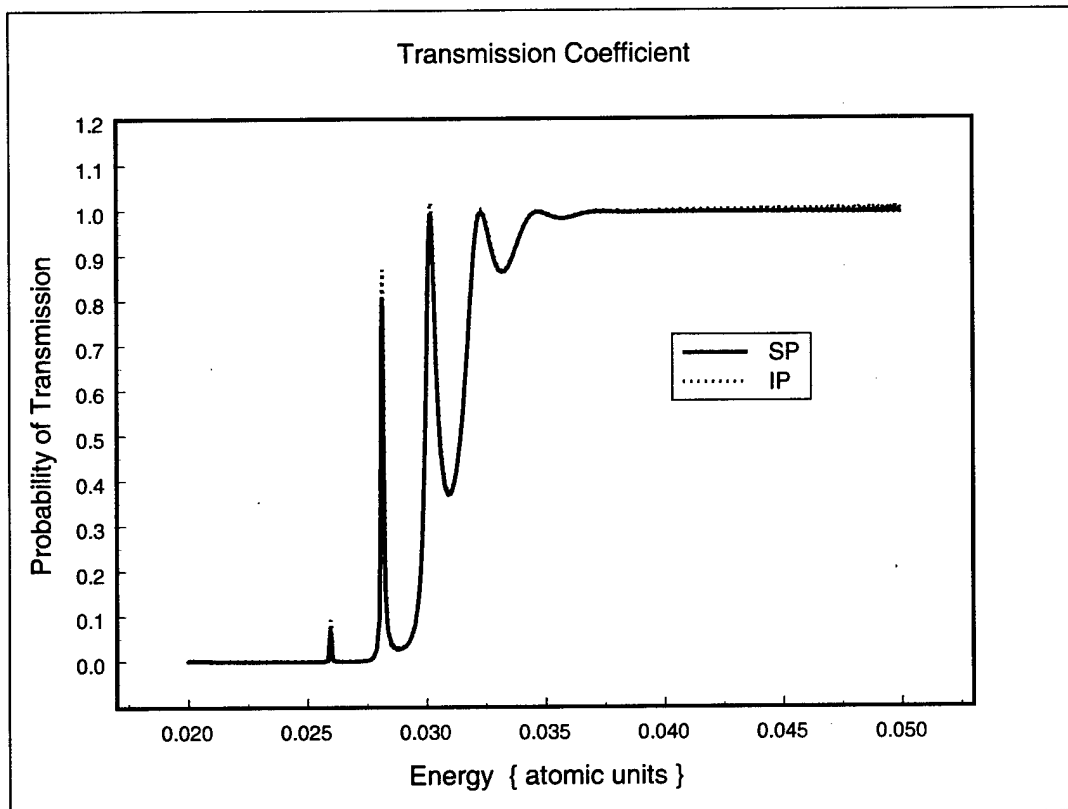
Figure 6.6   The transmission coefficient, computed from Møller states generated using the interaction picture (dotted line) and the Schrödinger picture (solid line). The interaction-picture S-matrix elements were computed on a grid half the size required for the Schrödinger-picture matrix elements.

Parameter	Potential 1	Potential 2	Potential 3	Potential 4
A	0.03	0.03	0.03	0.03
B	0.09	0.09	0.09	0.09
C	0.03	0.03	0.03	0.03
D	0.0	0.0	0.0	0.0
a	-4.0	-4.0	-4.0	-21.0
b	0.0	0.0	0.0	0.0
c	4.0	4.0	4.0	21.0
α	1.0	0.5	0.25	0.015625
β	1.0	0.5	0.25	0.015625
γ	1.0	0.5	0.25	0.015625

Table 6.4   The coefficients used in Equation 6.1 to create four potential functions with similar energy characteristics but differing slopes. All quantities use atomic units.

6.2 Effect of Potential Slope

The interaction picture is at a performance disadvantage relative to the Schrödinger picture regarding time-independent potentials. Since all spatially non-constant potentials yield time-dependent Hamiltonians in the interaction picture, the length of the calculation time step Δt is more constrained than it is for the corresponding time-independent Hamiltonian in the Schrödinger picture. In this section, the effect of varying the rapidity of change of the potential with the spatial coordinate is examined, using several symmetric potentials (Figure 6.7) fomulated according to equation (6.1), with the parameters given in Table 6.4. The measure of error chosen is the amplitude error of the wave function, given by equation 4.2. For a fixed time step, chosen to be $\Delta t = 1.0$ atomic units, three reactant Møller state calculations are performed on identical coordinate grids. The propagation techniques examined are a Lanczos method in the interaction picture using a first-order approximation of the Hamiltonian, a second-order Lanczos method in the interaction picture, and a split-operator method in the Schrödinger picture. The amplitude error of each is measured periodically relative to a Schrödinger-picture split-operator propagation using a time step $\Delta t' = 0.1$. Before comparison to the reference wavepacket, the interaction-picture wavepackets of course must be converted to the Schrödinger picture.

The calculation on the steepest potential (Potential 1) shows that for this potential, the chosen time step produces accurate Møller states from both the Schrödinger and
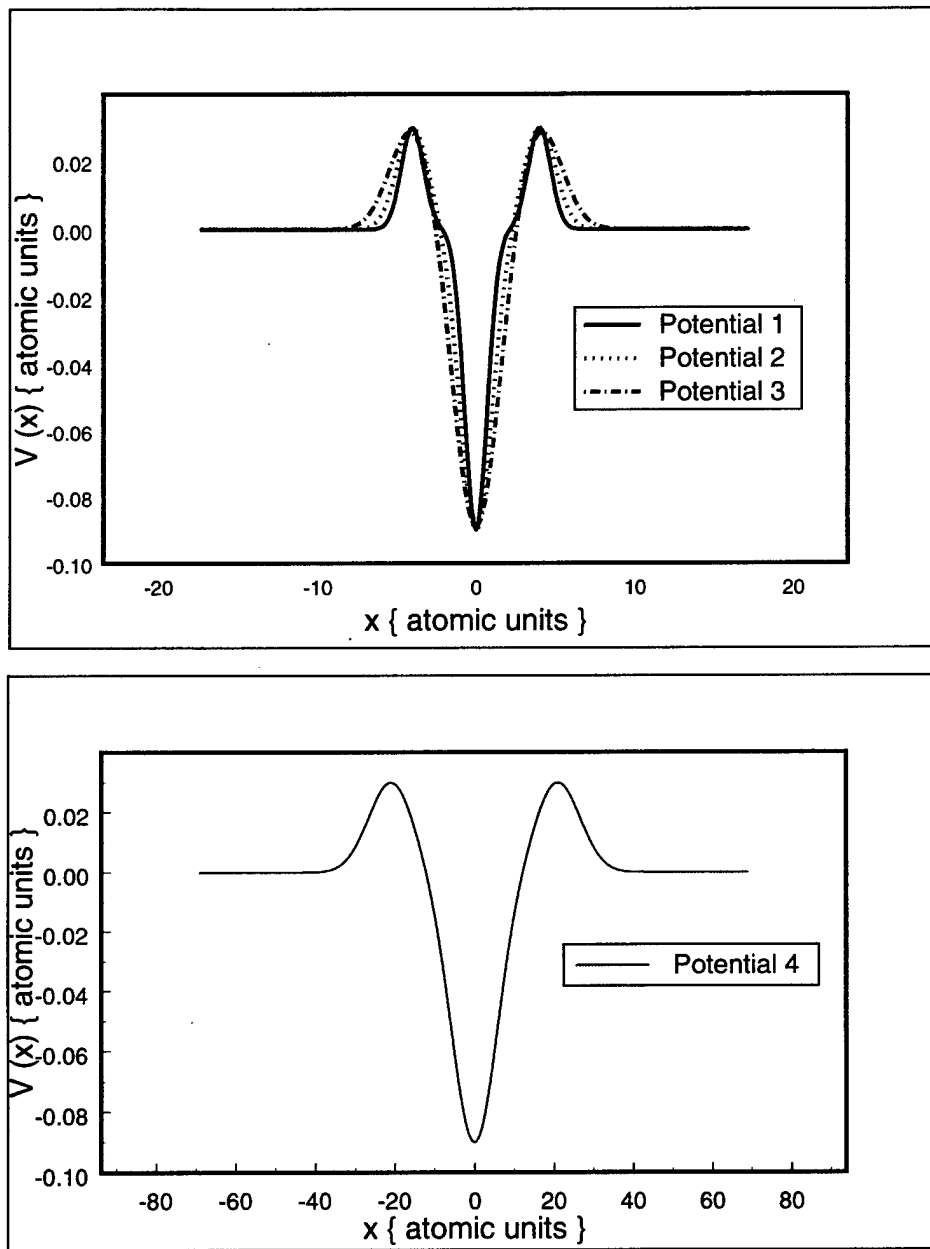
Figure 6.7   The four triple Gaussian potentials used to investigate the effect of varying
potential slope on the accuracy of propagation in the interaction picture.

Figure 6.8   The growth in amplitude error (equation (4.2)) during the computation of
the reactant Møller state for Potential 1. The solid line corresponds to a
scond-order nested interaction-picture Lanczos propagator, the alternating
dots and dashes to a first-order one. The dotted line shows the error in the
computation of the same Møller state using a split-operator propagator in
the Schrödinger picture. All propagations shown used a time step $\Delta t = 1.0$
atomic unit. The amplitude error for all three propagations is measured
against a split-operator propagation using $\Delta t' = 0.1$ atomic units.

the second-order interaction pictures, as shown in Figure 6.8. The first-order interaction-picture propagator diverges rapidly and fails to produce an acceptable Møller state. The second-order interaction-picture propagator diverges as the wavepacket encounters the potential, but maintains good correspondence to the reference calculation overall. The much more gradual divergence of the Schrödinger-picture method begins to accelerate late in the calculation, but still results in a Møller state that is markedly closer to the reference than the interaction-picture state is. This is reasonable to expect, since the reference state is computed by the identical method, the only difference being the length of the time step.

The somewhat reduced slope of Potential 2, with its slightly broader features, worked to the benefit of all three propagators, though not enough to get an accurate result from the first-order interaction-picture propagator. The divergence of both the second-order interaction-picture and the Schrödinger-picture propagators is less rapid, and occurs later, even though the interaction region of the potential is encountered earlier in the propagation. Figure 6.9 depicts the evolution of the Møller-state error for Potential 2.

Figure 6.10 shows the error associated with Møller-state propagation on Potential 3, which has still broader and more gradually sloped features than Potentials 1 and 2. The marginal improvement in the results from all three propagations seen between Potentials 1 and 2 is extended with Potential 3.

Potentials 1 through 3 are all very similar, and demonstrate the expected benefits of reduced potential slope to the interaction picture, while showing that the Schrödinger picture also enjoys improved accuracy. To achieve yet broader and more gradually sloped features with a triple Gaussian potential, while retaining the well and barrier energies, requires moving the locations of the outer Gaussians farther away from the central one. Potential 4 is the result of such an operation. The error of the Møller-state calculations on this potential, shown in Figure 6.11, is higher than might be expected from the trend seen with Potentials 1 through 3; however, the larger extent of this potential necessitated four times larger grids in both the interaction and Schrödinger pictures. The problem is therefore of somewhat greater computational difficulty.
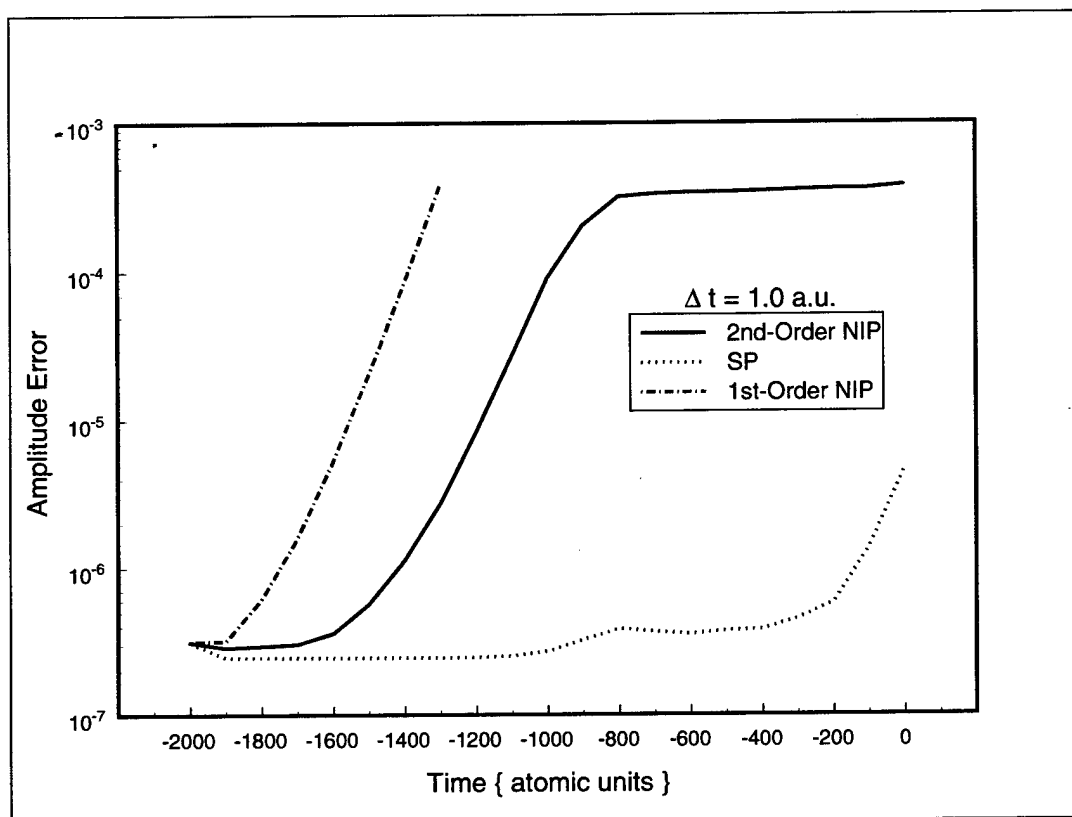
Figure 6.9   The growth in amplitude error (equation (4.2)) during the computation of
the reactant Møller state for Potential 2. The solid line corresponds to a
scond-order nested interaction-picture Lanczos propagator, the alternating
dots and dashes to a first-order one. The dotted line shows the error in the
computation of the same Møller state using a split-operator propagator in
the Schrödinger picture. All propagations shown used a time step $\Delta t = 1.0$
atomic unit. The amplitude error for all three propagations is measured
against a split-operator propagation using $\Delta t' = 0.1$ atomic units.

Figure 6.10   The growth in amplitude error (equation (4.2)) during the computation of the reactant Møller state for Potential 3. The solid line corresponds to a scond-order nested interaction-picture Lanczos propagator, the alternating dots and dashes to a first-order one. The dotted line shows the error in the computation of the same Møller state using a split-operator propagator in the Schrödinger picture. All propagations shown used a time step $\Delta t = 1.0$ atomic unit. The amplitude error for all three propagations is measured against a split-operator propagation using $\Delta t' = 0.1$ atomic units.
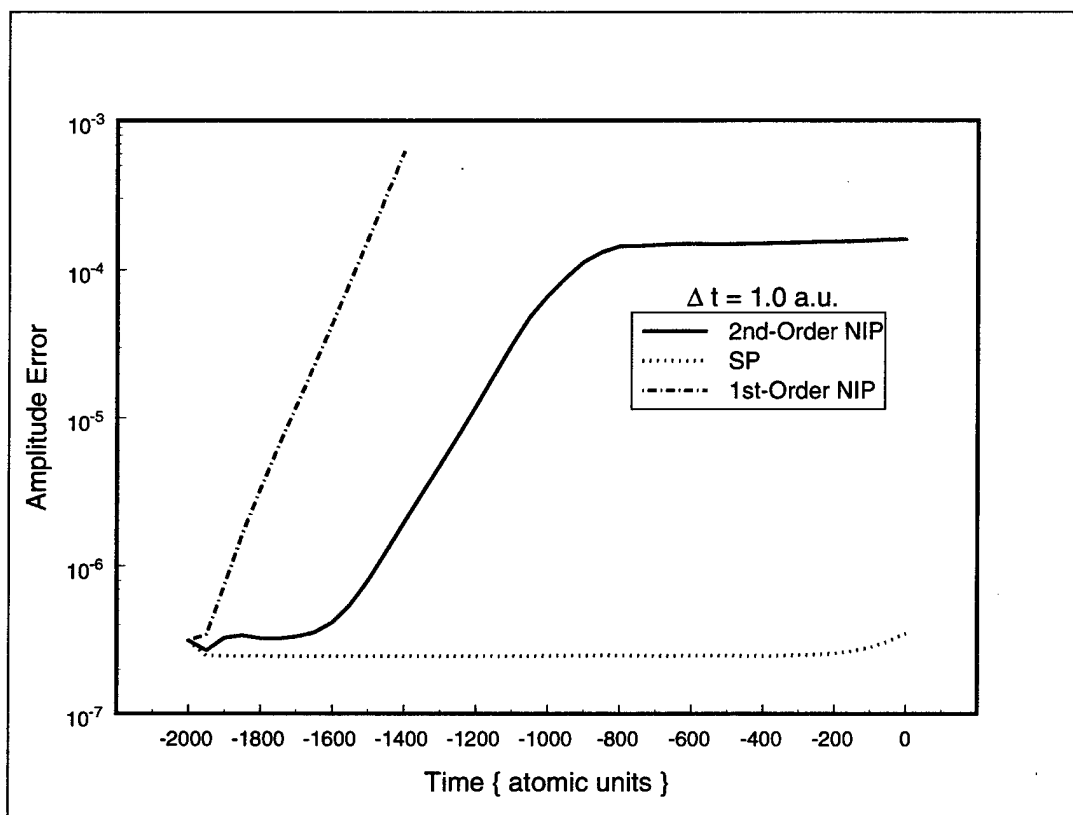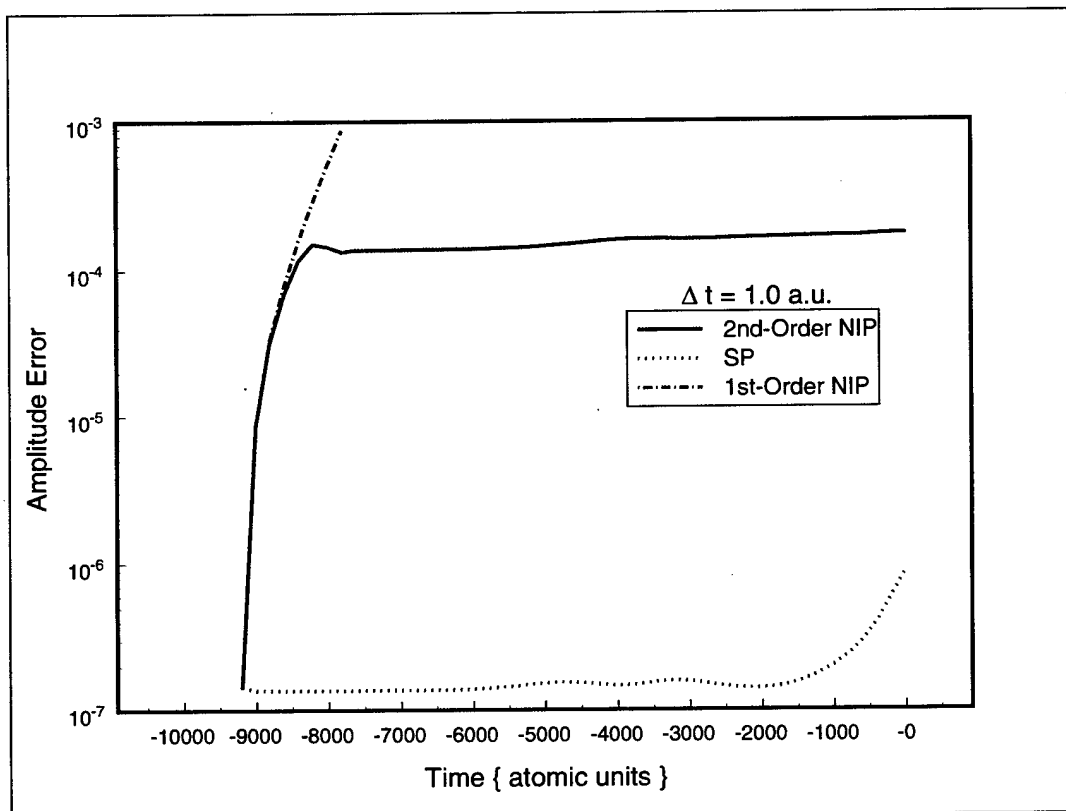
Figure 6.11   The growth in amplitude error (equation (4.2)) during the computation of
the reactant Møller state for Potential 4. The solid line corresponds to a
scond-order nested interaction-picture Lanczos propagator, the alternating
dots and dashes to a first-order one. The dotted line shows the error in the
computation of the same Møller state using a split-operator propagator in
the Schrödinger picture. All propagations shown used a time step $\Delta t = 1.0$
atomic unit. The amplitude error for all three propagations is measured
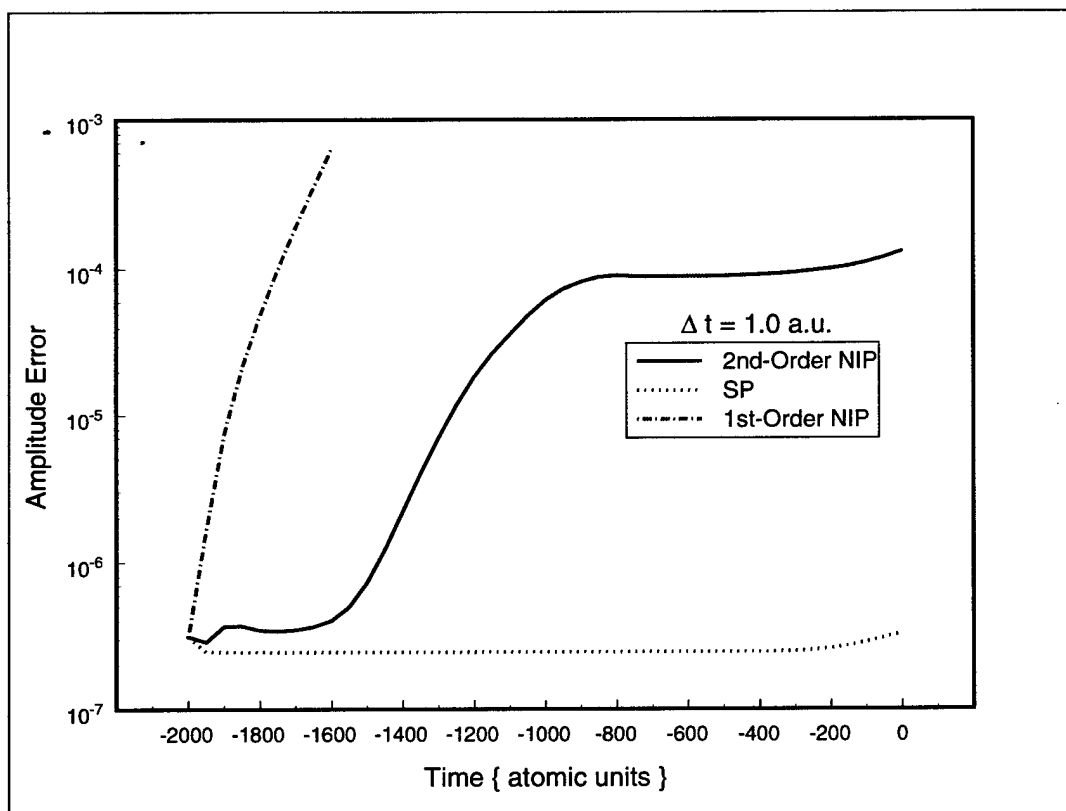against a split-operator propagation using $\Delta t' = 0.1$ atomic units.

Figure 6.12 places the error trajectories for the second-order interaction-picture propagator with all four potentials together. The general conclusion to be drawn is that error levels, while less for lower-sloped potentials on the same computational grid, are not significantly altered when the barrier and well energies remain the same.
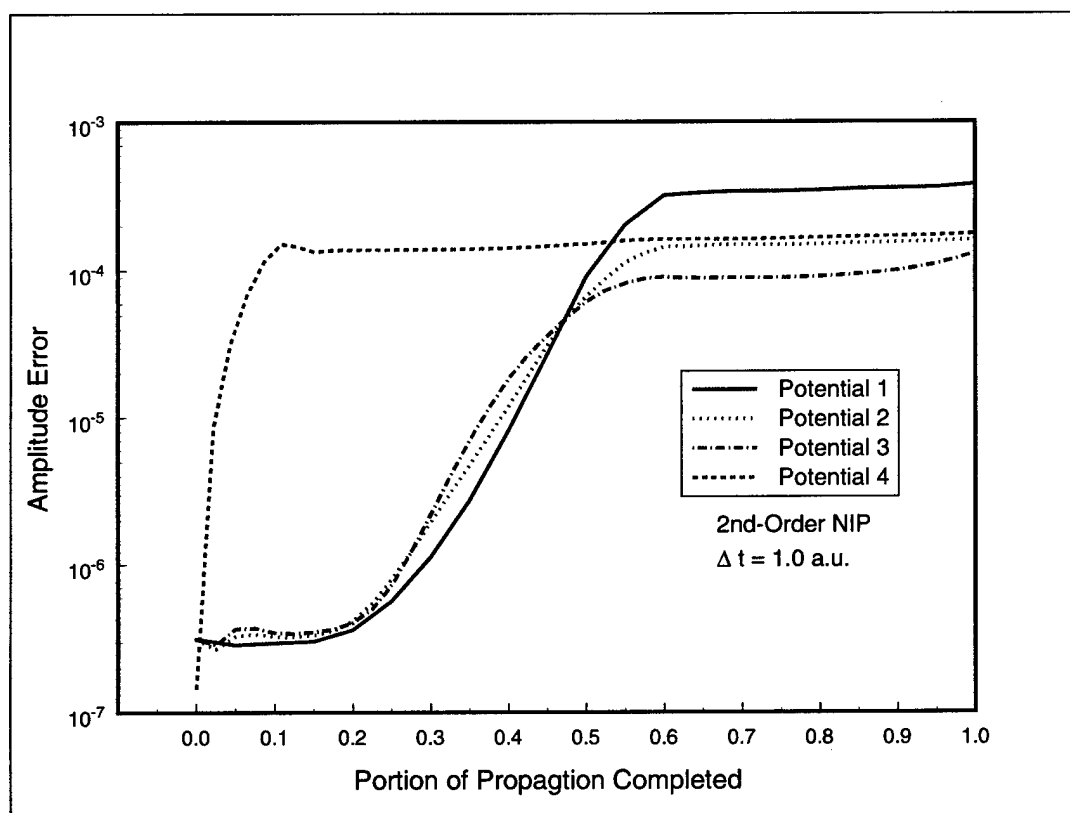
Figure 6.12   The amplitude error functions for the second-order interaction-picture propagator on the four symmetric triple Gaussian potentials, displayed together for comparison.

6.3   Effect of Wavepacket Compactness

Employment of the interaction picture in the calculation of Møller states can be relied upon to enable reduction of the computational coordinate grid by a factor of two, as demonstrated above. However, a factor of two is not enough to result in a reduction in the propagation time relative to the Schrödinger picture. This is because the (usually

shorter) time steps in the Lanczos method require at least as many FFTs as there are Krylov basis vectors, as compared to two FFTs per time step in the split-operator propagation scheme, which can be employed with the time-independent Hamiltonians common to the Schrödinger picture. The nested interaction picture requires an additional pair of FFTs per time step to compute the expectation values $\langle \mathbf{x} \rangle$ and $\langle \mathbf{p} \rangle$; and the second-order Lanczos algorithm adds an expensive matrix diagonalization as well in order to lengthen the allowable time step. This is a worthwhile investment, as shown in Section 6.2 where results of a first-order and a second-order propagator are compared.

The Schrödinger picture can require much larger grids than the interaction picture when the wavepackets remain compact throughout the propagation. A wavepacket whose momentum has a large absolute value requires a large value of k_{max}, with a concomitant small coordinate spacing Δx. This in turn necessitates a large number N of grid points to contain the trajectory of the coordinate representation, even though the wavepackets in both representations may be relatively compact. However, compact wavepackets my be propagated in the nested interaction picture using grids barely large enough to contain the wavepackets alone; the grids are adjusted continuously to follow their trajectories in both representations. This situation is illustrated with the barrier potential shown in Figure 6.13. Two collision scenarios are examined with this potential, both at a kinetic energy of 3.0 atomic units. One scenario involves a reactant state with low reduced mass and correspondingly low momentum; the other a reactant state with higher reduced mass and momentum.

6.3.1 Low-Momentum Collision. For this example, a reactant state with reduced mass $\mu = 18.36$ atomic units is chosen, with momentum atomic units and Gaussian width parameter $\sigma = 0.05$. The propagation begins in the asymptotic region at time $-\tau = -20$ atomic units, and proceeds in time steps $\Delta t = 0.01$ atomic units. Møller states are derived in both the interaction and Schrödinger pictures. The results of this scenario are summarized in Table 6.5. An eightfold reduction in the grid size required for the calculation was realized in the interaction picture as compared to the Schrödinger picture. This is sufficient for the interaction picture to be the faster of the two computational
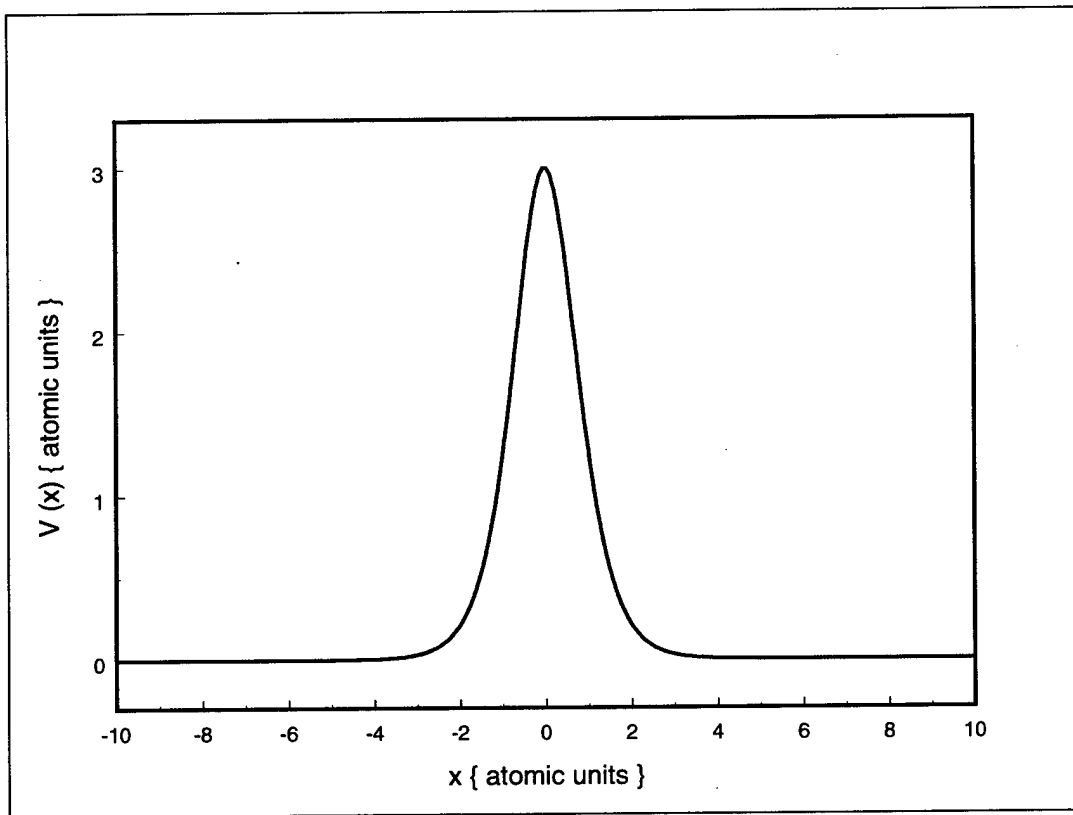
Figure 6.13   The barrier potential $V(x) = 3.0 \operatorname{sech}(x)$.

Propagation Method	Grid Size (N)	Grid Spacing (Δx)	CPU Time (sec)
SP/SPO	512	0.1	6.8
SP/SPO	256	0.1	3.2
IP/2SIL	32	0.2	2.9

Table 6.5　Møller-state propagations with a low-momentum reactant state on the barrier potential of Figure 6.13, using the split-operator (SPO) method in the Schrödinger picture (SP) and a second-order short iterative Lanczos (2SIL) method in the interaction picture (IP) .

Propagation Method	Grid Size (N)	Grid Spacing (Δx)	CPU Time (sec)
SP/SPO	1024	0.1	14.8
SP/SPO	512	0.1	6.8
IP/2SIL	32	0.2	2.9

Table 6.6　Møller-state propagations with a low-momentum reactant state on the barrier potential of Figure 6.13, using the split-operator (SPO) method in the Schrödinger picture (SP) and a second-order short iterative Lanczos (2SIL) method in the interaction picture (IP) .

techniques in this scenario. The CPU times reported in the table are from the Silicon Graphics IRIX "time" utility on MIPS 10000 processors.

6.3.2　High-Momentum Collision.　A higher-momentum wavepacket makes more clear a weakness of the Schrödinger picture when compared to the interaction picture. At the same kinetic energy as the previous case, if the reactant state has mass $\mu = 1836$ atomic units and momentum $k_0 = 104.2$, a starting time $-\tau = -100$ is required for the intermediate wavepacket to be clear of the interaction region at the beginning of the forward propagation. The greater time than the low-momentum case results from more rapid spreading of the wavepacket during its analytic propagation backward in time to create the intermediate state at $t = -\tau$. The end result is a need for more room in the coordinate representation to contain the extra spreading and translation of the wavepacket. In contrast, the interaction-picture propagation can be done on the same grid as the previous calculation. Table 6.6 summarizes the results of this group of propagations, which use a time step $\Delta t = 0.05$ atomic units on MIPS 10000 processors.

6.4 Summary

Propagation in the interaction picture is a reliable, accurate option for computing the Møller states needed for the channel-packet method of deriving selected S-matrix elements. The interaction picture can usually accomplish the calculation on a grid that is, at most, half the minimum size possible when propagating in the Schrödinger picture. However, because of the larger number of FFTs and matrix diagonalizations per time step, as well as the time dependence of its Hamiltonians, propagation in the interaction picture tends to require more time to reach an accurate evaluation of a Møller state than propagation in the Schrödinger picture. The interaction picture becomes most advantageous in grid savings and comparative computational time in high-momentum collisions.

VII. Conclusion

Through the use of the channel-packet method, the interaction picture can be used to compute reactive scattering matrix elements on reduced computational grids. Previous use of the interaction picture has been restricted to single scattering channels, limiting its application to non-reactive scattering problems. The channel-packet method opens the possibility of extending the efficacy of the interaction picture by allowing each Møller state to be computed in an interaction picture derived from its asymptotic Hamiltonian. A twofold reduction in required grid size is generally possible, and under the right conditions, larger grid reductions can be achieved.

7.1 Efficacy of the Interaction Picture in One Dimension

Three primary achievements have been demonstrated during this research project. First, a method has been found to apply the interaction picture to multichannel reactive scattering, retiring the commonplace that "there is no convenient generalization of the interaction picture" to such scenarios (1). Second, the nested interaction picture has been shown reliably to allow computation of Møller states on grids at least a factor of two smaller than the smallest possible grid required to derive the same states in the Schrödinger picture. Third, while accurate Møller states for most one-dimensional potentials can be computed more quickly in the Schrödinger picture, under conditions where a Møller state that remains compact in both its coordinate and its momentum representation allows much larger grid size reductions, the nested interaction picture has been shown to be the faster choice in one dimension. What happens to this situation in higher-order systems remains to be shown, but as suggested in Section 7.2, the advantages of the Schrödinger picture may erode as more degrees of freedom are added.

The interaction picture is now indisputably applicable to the calculation of reactive S-matrix elements, and has been shown to dovetail effectively with the channel-packet method and absorbing boundary conditions in reducing the memory required in the computation of Møller states. Because of the time-dependence of the interaction-picture Hamiltonian, however, the interaction picture requires shorter time steps in the interaction region of the

Method	Comment
Sequential	Reliable, accurate, slow, no grid reduction
Finite Basis	Unstable, unsuitable for long propagations
Sequential Nested	Reliable, accurate, slow, grid reduction at least twofold
"Heisenberg" Nested	Needs analytic expression for potiential; works only for certain potentials

Table 7.1   Summary of results of investigations of various interaction-picture techniques.

potential, so in one dimension, reductions in computational time relative to the Schrödinger picture are realized only under special circumstances, with the largest reductions in grid size. Of the numerous approaches to wavepacket propagation in the interaction picture investigated in this project, only the laborious sequential methods were reliably accurate when implemented and tested, and only the sequential nested interaction picture was able to deliver any reduction in grid size requirements. Table 7.1 summarizes the methods tested and the results in each case. All implementations used the iterated Lanczos algorithm to represent the time-evolution operator.

7.2   Extension of the Nested Interaction Picture to More Degrees of Freedom

If the interaction picture is ever to be useful in genuine molecular scattering calculations, it must be applied in three or more dimensions. The interaction picture offers a reduction in the memory requirements for such calculations by reducing the grid requirements along the translational coordinates of a multidimensional model. Computational time, a more desirable commodity to conserve than simply memory, is not necessarily reduced in one-dimensional calculations using the interaction picture because of the shorter time steps necessitated by the interaction picture's time-dependent Hamiltonians. However, with added dimensions, the nature of the underlying mathematics suggests that reductions in computational time could be realized in multidimensional calculations even if the one-dimensional interaction picture process requires more time than the Schrödinger picture on a larger grid. Assuming that the FFT dominates the computational effort required in the calculation of the Møller states, effort E_n scales with number n of degrees of

freedom as

$$E_n = (n-1)!P_n \log P_n, \tag{A.7}$$

where the argument P_n is the product of the grid sizes for all n degrees of freedom. The derivation of equation (A.7) appears in Appendix A.

Suppose the nested interaction picture in n dimensions allows one dimension's coordinate grid to be reduced from N_j to N_j/b. If the interaction-picture propagation requires a times longer than the Schrödinger picture in one dimension, then using equation (A.7),

$$
\begin{aligned}
a &= \left(\frac{T_I}{T_S}\right)_{n=1} = \frac{\beta \frac{N_j}{b} \log \frac{N_j}{b}}{\alpha N_j \log N_j} \\
&= \frac{\beta \log \frac{N_j}{b}}{\alpha b \log N_j} \\
&= \frac{\beta}{\alpha b} \left(1 - \frac{\log b}{\log N_j}\right),
\end{aligned}
\tag{7.1}
$$

for some pair of real constants α and β, which account for differences in the optimum time step and in the number of FFTs needed per time step between the two methods. The ratio of propagation times for $n > 1$ dimensions is

$$
\begin{aligned}
\left(\frac{T_I}{T_S}\right)_n &= \frac{\alpha \frac{P_n}{b} \log \frac{P_n}{b} + (\beta - \alpha)\frac{N_j}{b} \log \frac{N_j}{b}}{\alpha P_n \log P_n} \\
&= \frac{1}{b} - \frac{\log b}{b \log P_n} + \frac{(\beta - \alpha)\frac{N_j}{b} \log \frac{N_j}{b}}{\alpha P_n \log P_n}.
\end{aligned}
\tag{7.2}
$$

As the number of degrees of freedom n increases, the terms with $\log P_n$ in the denominator vanish, and the computational-effort ratio given by equation (7.2) approaches

$$\lim_{n \to \infty} \left(\frac{T_I}{T_S}\right)_n = \frac{1}{b}. \tag{7.3}$$

Hence, as degrees of freedom are added, the comparative computational effort of the interaction picture relative to the Schrödinger picture approaches the ratio of the required grid sizes in the single dimension that is different.

7.3 Topics for Further Study

The successes obtained within the confines of this investigation point the way to many related topics where the use of interaction picture continues to be an attractive potential tool for scattering calculations. The unsatisfactory performance of the finite-basis and "Heisenberg" approaches has not been conclusively explored. Either of these techniques would be a significant advance over what has thus far been demonstrated should the problems be overcome. The finite-basis approach may well be inherently unstable because it bases its Krylov vectors on a representation of the Hamiltonian in another Krylov subspace, instead of in either the coordinate or momentum representation. However, only a highly speculative reason has been put forward as to why the "Heisenberg" nested interaction picture fails for most potentials. Zhang's finite-difference approach is also an interesting option, requiring fewer FFTs than the Lanczos-based propagation schemes tested here(46,82). The question of how beneficially the techniques developed here in one dimension scale to the much larger dimensionalities of "real" molecular scattering problems also remains to be settled.

It is important to note that since the short iterative Lanczos propagation scheme is employed when using the nested interaction picture, a greater number of FFTs is required per time step when compared to the split-operator approach commonly used for time independent Hamiltonians in the Schrödinger picture. This results in a trade-off between the computational savings afforded by the grid reduction, and the requirement for a larger number of FFTs per time step. An alternative to the short iterative Lanczos propagator that avoids this trade-off is the second order finite difference propagation technique developed by Zhang(46,82). Using this approach, the number of FFTs per time step is reduced to the same number required by the split-operator method. This second order finite difference technique has been successfully applied to a two-dimensional model of CH_3I photodissociation(83), and to a three-dimensional model of vibrational predissociation of van der Waals molecules(84).

Related scattering calculations into which further investigations might be made using the interaction picture include time-dependent potential-energy surfaces, molecule-surface scattering, inclusion of electronic degrees of freedom (dropping the Born-Oppenheimer ap-

proximation), and adapting the models to parallel-architecture computers. Small, stochastic, time-dependent kicks to the potential may be used to model the behavior of the reaction in the presence of a solvent. The interaction picture is especially attractive for dealing with explicitly time-dependent Hamiltonians, since the Schrödinger-picture propagator then faces the same time-step issues that disadvantage the interaction picture when the potential is time-independent. The interaction of molecules with surfaces is of great interest because of the many practical applications of such reactions. Including electronic degrees of freedom would make the model more rigorously correct, at the cost of added complexity. However, the Born-Oppenheimer approximation is not valid for all molecular interactions(85). If the prediction of equation (7.3) holds—in itself a very important question to investigate—the interaction picture might be employed to reduce the added computational effort associated with the addition of degrees of freedom associated with atomic electrons. Parallelization is a natural improvement to consider because the FFT, which consumes much of the time needed by these computations, has been adapted with great success to parallel computers.

Appendix A. A General Scaling Rule for Computational Effort of Multidimensional FFTs

For a one-dimensional FFT, the execution time is governed by the total number of multiplications, which scales with the grid size N as

$$E_1 = N \log_\gamma N, \tag{A.1}$$

where γ is the order, usually 2, of the FFT's divide-and-conquer scheme(86). Since we are only interested in relative scaling using the same FFT base, the value of γ is unimportant and will be dropped from now on.

Two–dimensional FFTs on $N_1 \times N_2$ grids are calculated by performing one-dimensional FFTs on the N_1 rows of length N_2, followed by another N_2 on the columns of length N_1. Hence, the total effort scales with grid size as

$$
\begin{aligned}
E_2 &= N_1 N_2 \log N_2 + N_2 N_1 \log N_1 \\
&= N_1 N_2 \log N_1 N_2 \\
&= P_2 \log P_2,
\end{aligned}
\tag{A.2}
$$

where we define the n-dimensional grid product,

$$P_n = \prod_{i=1}^{n} N_i. \tag{A.3}$$

A three-dimensional FFT breaks down into N_1 two-dimensional FFTs on $N_2 \times N_3$ grids, plus N_2 on $N_1 \times N_3$ grids, and N_3 on $N_1 \times N_2$ grids. The scaling is therefore,

$$
\begin{aligned}
E_3 &= N_1 \left\{ N_2 N_3 \log N_2 N_3 \right\} + N_2 \left\{ N_1 N_3 \log N_1 N_3 \right\} + N_3 \left\{ N_1 N_2 \log N_1 N_2 \right\} \\
&= P_3 \log (P_3)^2 \\
&= 2 P_3 \log P_3.
\end{aligned}
\tag{A.4}
$$

Similarly, in four dimensions there are four sets of three-dimensional FFTs involved, and the scaling with grid size is,

$$
\begin{aligned}
E_4 &= N_1 \left\{ 2N_2N_3N_4 \log N_2N_3N_4 \right\} + N_2 \left\{ 2N_1N_3N_4 \log N_1N_3N_4 \right\} \\
&\quad + N_3 \left\{ 2N_1N_2N_4 \log N_1N_2N_4 \right\} + N_4 \left\{ 2N_1N_2N_3 \log N_1N_2N_3 \right\} \quad \text{(A.5)} \\
&= 2P_4 \log \left(P_4 \right)^3 \\
&= 3! P_4 \log P_4. \quad \text{(A.6)}
\end{aligned}
$$

The general formula for computational effort of an n-dimensional FFT,

$$
E_n = (n-1)! P_n \log P_n, \quad \text{(A.7)}
$$

is seen to hold for n between 1 and 4. If $n > 4$, assuming (A.7) to be true for $n-1$, the scaling rule is

$$
\begin{aligned}
E_n &= \sum_{i=1}^{n} (n-2)! P_n \log \frac{P_n}{N_i} \\
&= (n-2)! P_n \log \prod_{i=1}^{n} \frac{P_n}{N_i} \\
&= (n-2)! P_n \log \frac{\prod_{i=1}^{n} P_n}{\prod_{i=1}^{n} N_i} \\
&= (n-2)! P_n \log \frac{P_n^n}{P_n} \\
&= (n-2)! P_n \log P_n^{n-1} \\
&= (n-1)! P_n \log P_n. \quad \text{(A.8)}
\end{aligned}
$$

Equation (A.7) is therefore, by induction, the scaling rule for all natural numbers n of grid dimensions.

Bibliography

1. Taylor, J. R. *Scattering Theory: The Quantum Theory of Nonrelativistic Collisions;* Corrected Reprint ed.; Krieger: Malabar, FL, 1987.

2. Diestler, D. J. *J. Chem. Phys.* 1969, 50, 4746

3. Diestler, D. J. *J. Chem. Phys.* 1971, 54, 4547.

4. Manolopoulos, D. E. *J. Chem. Phys.* 1986, 85, 6425.

5. Alexander, M. H.; Manolopoulos, D. E. *J. Chem. Phys.* 1987, 86, 2044.

6. Secrest, D., in *Atom-Molecule Collision Theory: A Guide for the Experimentalist,* ed. R. B. Bernstein; Plenum: New York, 1979; p. 265.

7. Kosloff, R. *J. Phys. Chem.* 1988, 92, 2087.

8. Gerber, R. B.; Kosloff, R.; Berman, M. *Comput. Pys Rep.* 1986, 5, 59.

9. Kosloff, R.; Kosloff, D. *J. Chem. Phys.* 1983, 72, 1823.

10. Judson, R. S.; Kouri, D. J.; Neuhauser, D.; Baer, M. *Phys. Rev. A* 1990, 42, 351.

11. Sharafeddin, O.A.; Zhang, J.Z.H. *Chem. Phys. Lett,,* 1993, 204, 190.

12. Dai, J.; Zhang, J. Z. H. *J. Phys. Chem.* 1996, 100, 6898.

13. Schatz, G. C. *J. Phys. Chem.* 1996, 100, 12839.

14. Zhu, W.; Zhao, X.; Tang, Y.. *J. Chem. Phys.* 96, 106, 2271.

15. Mead, C. A. In *Mathematical Frontiers in Computational Chemical Physics*; Truhlar, D. G., Ed.; Springer-Verlag: New York, 1988.

16. Zhang, Dong H.; Zhang, John Z. H. *J. Chem. Phys.* 1994, 101, 1146.

17. Wu, Qian; Zhang, Dong H.; Zhang, John Z. H. *J. Chem. Phys.* 1995, 103, 2548.

18. Zhang, Dong H.; Light, John C. *J. Chem. Phys.* 1996, 104, 4530.

19. Dai, Jiqong; Zhu, Wei; Zhang, John Z. H. *J. Phys. Chem.* 1996, 100, 13901.

20. Wilson, E. B., Jr.; Decius, J. C.; Cross, P. C. *Molecular Vibrations*; Dover: New York, 1980.

21. Baer, M. In *Advances in Chemical Physics;* I. Prigogine and S. A. Rice, Ed.; Wiley: New York, 1982.

22. Weeks, D. E.; Tannor, D. J. *Chem. Phys. Lett.* 1994, 224, 451.

23. Calfas, R.; Weeks, D E. *Chem. Phys. Lett.* 1996, 263, 292.

24. Weeks, D. E.; Calfas, R. S. *Proceedings of the High Energy Density Matter Contractors' Conference;* 20 May 1998, Monterey, in California, in press.

25. Garashchuk, S.; Tannor, D.J. *Chem. Phys. Lett,* 1996, 262, 477.

26. Jäckle, A.; Meyer, H.D. J. Chem. Phys. 1995, 102, 5650.

27. Merzbacher, E. *Quantum Mechanics;* Wiley: New York, 1970.

28. Newton, R. G. *Scattering Theory of Waves and Particles*; 2nd ed.; Springer-Verlag: New York, 1982.

29. Weeks, D. E.; Tannor, D. *J. Chem. Phys. Lett.* 1993, 207, 301.

30. Tannor, D. J.; Weeks, D. E. *J. Chem. Phys.* 1993, 98, 3884.

31. Levine, R. D. *Quantum Mechanics of Molecular Rate Processes;* Oxford University Press: Oxford, UK, 1969.

32. Isele, A.; Meier, C.; Engel, V.; Fahrer, N.; Schlier, C. *J. Chem. Phys.* 1994, 101, 5919.

33. Gazdy, B.; Bowman, J. M. In *Advances in Molecular Vibrations and Collision Dynamics;* J. M. Bowman and M. A. Ratner, Eds.; JAI Press: Greenwich, 1991; Vol. 1B; p. 105.

34. Leforestier, C.; Bisseling, R. H.; Cerjan, C.; Feit, M. D.; Friesner, R.; Guldberg, A.; Hammerich, A.; Jolicard, G.; Karrlein, W.; Meyer, H.-D.; Lipkin, N.; Roncero, O.; Kosloff, R. *J. Comput. Phys.* 1991, 94, 59.

35. Feit, M. D.; Fleck, J. A., Jr.; Steiger, A. *J. Comput. Phys.* 1982, 47, 412.

36. Fleck, J. A., Jr.; Morris, J. R.; Feit, M. D. *Appl. Phys.* 1976, 10, 129.

37. Magnus, W.; Karrass, A.; Solitar, D. *Combinatorial Group Theory: Presentations of Groups in Terms of Generators and Relations;* Wiley: New York, 1966.

38. Kosloff, R.; Cerjan, D. *J. Chem. Phys.* 1984, 81, 3722.

39. Neuhauser, D.; Baer, M. *J. Chem. Phys.* 1989, 90, 4351.

40. Neuhauser, D.; Baer, M. *J. Chem. Phys.* 1989, 91, 4651.

41. Neuhauser, D.; Baer, M.; Judson, R. S.; Kouri, D. J. *Comput. Phys. Commun.* 1991, 63, 460.

42. Balint-Kurti, G. G.; Vibok, A. in *Numerical Grid Methods and Their Application to Schrödinger's Equation,* C. Cerjan, ed.; Kluwer Academic: Dordrecht, 1993, 175.

43. Riss, U. V.; Meyer, H.-D. *J. Chem. Phys.* 1996, 105, 1409.

44. Lanczos, C., *J. Res. Natn. Bur. Stand.* 1950, 45, 255.

45. Cullum, J. K.; Willoughby, R. A. *Lanczos Algorithms for Large Symmetric Eigenvalue Computations;* Birkhäuser: Boston, 1985; Vol. 1.

46. Zhang, J. Z. H. *Chem. Phys. Lett.* 1989, 160, 417.

47. Zhang, J. Z. H. *J. Chem. Phys.* 1990, 92, 324.

48. MacLachlan, M. J.; Weeks, D. E. *J. Phys. Chem. A* 1998, 102, 9489.

49. Tannor, D. J.; Besprozvannaya, A.; Williams, C. J. *J. Chem. Phys.* 1992, 96, 2998.

50. Das, S.; Tannor, D. J. *J. Chem. Phys.* 1990, 92, 3403.

51. Williams, C. J.; Qian, J.; Tannor, D. J. *J. Chem. Phys.* 1991, 95, 1721.

52. Qian, Jiwen. *Wavepacket Approach to Triatomic Photodissociation and Molecule-Surface Reactive Scattering*, PhD Thesis, Dept. of Chemistry and Biochemistry, Notre Dame, Indiana, 1995.

53. Dirac, P. A. M. *The Principles of Quantum Mechanics*; 4th ed.; Clarendon: Oxford, 1958.

54. Shankar, R. *Principles of Quantum Mechanics;* Plenum: New York, 1980, p. 612.

55. Pechukas, P.; Light, J. C. *J. Chem. Phys.* 1966, 44, 3897.

56. Magnus, W. *Commun. Pure & Appl. Math.* 1954, 7, 649.

57. Salzman, W. R. *J. Chem. Phys.* 1985, 82, 822.

58. Sharafeddin, O. A. *J. Chem. Phys.* 1995, 103, 642.

59. Howard, R. E.; McLean, A. D.; Lester, W. A., Jr. *J. Chem. Phys.* 1979, 71, 2412.

60. Garrett, B. C.; Truhlar, D. G. *J. Chem. Phys.* 1980, 72, 3460.

61. Liu, B. *J. Chem. Phys.* 1973, 58, 1925.

62. Siegbahn, P.; Liu, B. *J. Chem. Phys.* 1978, 68, 2457.

63. Truhlar, D. G.; Horowitz, C. J. *J. Chem. Phys.* 1978, 68, 2468.

64. Truhlar, D. G.; Horowitz, C. J. *J. Chem. Phys.* 1979, 71, 1514.

65. Parker, G. A.; Langanà , A.; Crocchianti, S.; Pack, R. T. *J. Chem. Phys.* 1995, 102, 1238.

66. Baer, M.; Last, I.; Loesch, H.-J. *J. Chem. Phys.* 1994, 101, 9648.

67. Miller, D. L.; Wyatt, R. E. *J. Chem. Phys.* 1987, 86, 5557.

68. Brown, F. B.; Steckler, R.; Schwenke, D. W.; Truhlar, D. G.; Garrett, B. C. *J. Chem. Phys.* 1985, 82, 188.

69. Truhlar, D. G.; Garrett, B. C.; Blais, N. C. *J. Chem. Phys.* 1984, 80, 232.

70. Lynch, G. C.; Halvick, P.; Zhao, M.; Truhlar, D. G.; Yu, C.-H.; Kouri, D. J.; Schwenke, D. W. *J. Chem. Phys.* 1991, 94, 7150.

71. Schatz, G. C.; Dyck, J. *Chem. Phys. Lett.* 1992, 188, 11.

72. Paige, C. C., Ph.D. Thesis, University of London, 1971.

73. Paige, C. C., *J. Inst. Maths. Applics.* 1976, 18, 341.

74. Parlett, B. N., *The Symmetric Eigenvalue Problem.* Englewood Cliffs, NJ: Prentice-Hall, 1980, pp. 270-283 .

75. Parlett, B. N. and D. S. Scott, *Math. Comp.* 1979, 33, 217.

76. Jack Dongarra, Jeremy Du Croz, Iain Duff, and Sven Hammarling, *A Set of Level 3 Basic Linear Algebra Subprograms*; http://www.netlib.org/blas/blas3-paper.ps (1989).

77. E. Anderson, Z. Bai, C. Bischof, J. Demmel, J. Dongarra, J. Du Croz, A Greenbaum, S. Hammarling, A. McKenney, S. Ostrouchov, and D. Sorenson, LAPACK User's Guide; http://www.netlib.org/lapack/lug/lapack_lug.html (1995).

78. Netlib, "README File for CLAPACK";. http://www.netlib.org/clapack/readme

79. William H. Press, Saul A. Teukolsky, William T Vettering, and Brian P. Flannery, *Numerical Recipes in C: The Art of Scientific Computing.* Cambridge University Press: Cambridge, 2nd ed., 1992.

80. Calfas, Roy S., *Reactive Quantum Scattering in Two Dimensions,* Ph.D. Thesis AFIT/DSP/ENP/97-0, Air Force Institute of Technology, Wright-Patterson AFB, OH, 1996.

81. Bohm, David, *Quantum Theory.* New York: Dover, 1951, pp. 242-244.

82. J.Z.H. Zhang, *Comput. Phys. Commun.* 1991, 63, 28.

83. D.H. Zhang, O.A. Sharafeddin, and J.Z.H. Zhang, *Chemical Physics,* 1992, 167, 137.

84. D.H. Zhang and J.Z.H. Zhang, *J. Phys. Chem.* 1992, 96, 1575.

85. Yarkony, D. R.; *J. Phys. Chem.* 1996, 100, 18612.

86. E. Oran Brigham, *The Fast Fourier Transform and Its Applications*; Prentice-Hall: Englewood Cliffs,1988.

REPORT DOCUMENTATION PAGE		Form Approved OMB No. 0704-0188

1. REPORT DATE (DD-MM-YYYY) 09-09-1999	2. REPORT TYPE Doctoral Dissertation	3. DATES COVERED (From - To) Sep 94 - Sep 99

4. TITLE AND SUBTITLE
Application of the Interaction Picture to Reactive Scattering in One Dimension

5a. CONTRACT NUMBER

5b. GRANT NUMBER

5c. PROGRAM ELEMENT NUMBER

6. AUTHOR(S)
Michael J. MacLachlan, Major, USAF

5d. PROJECT NUMBER

5e. TASK NUMBER

5f. WORK UNIT NUMBER

7. PERFORMING ORGANIZATION NAME(S) AND ADDRESS(ES)
Air Force Institute of Technology
Department of Engineering Physics
2750 P Street
Wright-Patterson AFB, OH 45433-6583

8. PERFORMING ORGANIZATION REPORT NUMBER
AFIT/DS/ENP/99-02

9. SPONSORING/MONITORING AGENCY NAME(S) AND ADDRESS(ES)
Dr. Michael R. Berman
Air Force Office of Scientific Research
AFOSR/NL
801 North Randolph Street
Room 732
Arlington, VA 22203-1977

10. SPONSOR/MONITOR'S ACRONYM(S)

11. SPONSOR/MONITOR'S REPORT NUMBER(S)

12. DISTRIBUTION/AVAILABILITY STATEMENT
APPROVED FOR PUBLIC RELEASE; DISTRIBUTION UNLIMITED

13. SUPPLEMENTARY NOTES

14. ABSTRACT
The interaction picture is used together with the channel-packet method in a new time-dependent approach to compute reactive scattering matrix elements for simple one-dimensional systems representing typical molecular collisions. The channel-packet method enables the use of the interaction picture for computing reactive S-matrix elements by splitting the computation into two parts. First, asymptotic reactant and product wavepackets are individually propagated into the interaction region of the potential to form Moller states. The interaction picture reduces wavepacket spreading, decreasing the size of the region of space that must be modeled when computing the Moller states. By using two different interaction pictures--one for the reactant arrangement channel and one for the product arrangement channel--it is possible to realize savings in the required grid size. During the second part of the channel-packet computation, the reactant and product wavepackets obtained from the first part of the calculation are further propagated using the Schr"dinger picture. The time-dependent correlation between the evolving wavepackets is calculated as they split into energetically accessible arrangement channels and are absorbed using absorbing boundary conditions. The Fourier transform of the correlation function then gives the S matrix.

15. SUBJECT TERMS
QUANTUM CHEMISTRY, POTENTIAL SCATTERING, S MATRIX, QUANTUM THEORY, SCHRODINGER EQUATION

16. SECURITY CLASSIFICATION OF:			17. LIMITATION OF ABSTRACT	18. NUMBER OF PAGES	19a. NAME OF RESPONSIBLE PERSON Dr. David E. Weeks
a. REPORT U	b. ABSTRACT U	c. THIS PAGE U	UL	143	19b. TELEPHONE NUMBER (Include area code) (937) 255-3636, ext. 4561

Standard Form 298 (Rev. 8/98)
Prescribed by ANSI Std. Z39.18